HAL
open science

3D modelling of twisted multi-filamentary superconductors

Ludovic Didier Makong Helle Nkatack Makong Hell Nkatack

To cite this version:

Ludovic Didier Makong Helle Nkatack Makong Hell Nkatack. 3D modelling of twisted multi-filamentary superconductors. Electromagnetism. Université Paris Saclay (COmUE), 2017. English. NNT : 2017SACLS428 . tel-01679685

HAL Id: tel-01679685

https://theses.hal.science/tel-01679685v1

Submitted on 10 Jan 2018

HAL is a multi-disciplinary open access archive for the deposit and dissemination of scientific research documents, whether they are published or not. The documents may come from teaching and research institutions in France or abroad, or from public or private research centers.

L'archive ouverte pluridisciplinaire **HAL**, est destinée au dépôt et à la diffusion de documents scientifiques de niveau recherche, publiés ou non, émanant des établissements d'enseignement et de recherche français ou étrangers, des laboratoires publics ou privés.

NNT : 2017SACLS428

Thèse de doctorat de l'Université Paris-Saclay préparée à L'Université Paris-Sud

Ecole doctorale n°575
Electrical, Optical, Bio: PHYSICS AND ENGINEERING
Spécialité de doctorat: Génie électrique

par

M. Ludovic Didier MAKONG HELL

3D modelling of twisted multi-filamentary superconductors

Thèse présentée et soutenue à Gif-sur-Yvette, le 28 Novembre 2017.

Composition du Jury :

M.	Jean LÉVÊQUE	Professeur Université de Lorraine	(Président du jury)
M.	Gérard MEUNIER	Directeur de recherche CNRS	(Rapporteur)
M.	Benoît VANDERHEYDEN	Professeur Université de Liège	(Rapporteur)
M.	Christian Eric BRUZEK	Chargé de Recherche NEXANS	(Examinateur)
M.	Pierre VÉDRINE	Ingénieur de Recherche CEA	(Examinateur)
M.	Philippe MASSON	Professeur associé Université de Houston	(Co-encadrant)
M.	Abelin KAMENI	Maître de conférence Université Paris-Sud	(Co-encadrant)
M.	Frédéric BOUILLAULT	Professeur Université Paris-Sud	(Directeur de thèse)

Résumé

Introduction

L'intérêt croissant des applications liées à la supraconductivité à haute température nécessite des outils numériques permettant de modéliser rapidement et efficacement en 3D le comportement de tels matériaux. Malgré de nombreux travaux sur le sujet, présentés dans le chapitre 1, les méthodes developpées restent limitées par la complexité et le grand nombre de degrés de libertés des problèmes 3D modélisant les câbles multifilamentaires torsadés.

Par consequent, on se focalisera principalement dans ce travail de thèse sur le développement et la validation d'approches numériques permettant de simplifier considérablement la modélisation tridimensionnelle, appliquée à la formulation en champ magnétique $\mathbf{H}$, de câbles supraconducteurs multi-filamentaires torsadés. L'idée étant d'estimer rapidement et efficacement les pertes AC générées par de tels câbles.

Modélisation 3D de supraconducteurs à hautes températures

Au vu des limites présentes dans les approches numériques précédemment developpées pour la modélisation des supraconducteurs, le chapitre 2 explore et décrit deux approches numériques permettant de modéliser précisément en 3D le comportement thermo-électromagnétique non-linéaire des supraconducteurs à hautes températures. Les approches numériques décrites sont de types élements finis et Galerkin discontinue avec un accent sur le développement de cette dernière.

Ces approches discrétisent les équations non-linéaires, dont les inconnues sont le champ magnétique et la température. Ces équations résultent du couplage des lois de comportement électromagnétique caractérisant les supraconduteurs (loi électrique en puissance et comportement magnétique linéaire), des équations de Maxwell simplifiées en basses fréquences et enfin des équations thermiques :

$$\begin{aligned} \mathbf{H} \ &: \ \mu_0 \frac{\partial \mathbf{H}}{\partial t} + \nabla \times (\rho(J,T) \cdot \nabla \times \mathbf{H}) = \mathbf{0} \\ T \ &: \ \rho_T c_p(T) \frac{\partial T}{\partial t} - \nabla \cdot (\lambda(T) \nabla T) = \rho(J,T) \mathbf{J}^2 \end{aligned} \tag{1}$$

où

$$\rho(J,T) = \frac{E_c}{J_c(T)} \left\| \frac{\mathbf{J}}{J_c(T)} \right\|^{n(T)-1} \tag{2}$$

Dans l'approche type éléments finis, l'accent est mis sur le traitement des non-linéarités issues du comportement électrique des supraconducteurs via une linéarisation de la loi puissance.

$$\mathbf{E}(\mathbf{J}_k) = \mathbf{E}(\mathbf{J}_{k-1}) + \overline{\overline{\mathbf{A}}} \cdot (\mathbf{J}_k - \mathbf{J}_{k-1}) \tag{3}$$

avec

$$\overline{\overline{\mathbf{A}}} = \begin{cases} \mathbb{J}, \text{ in } \Omega_s \\ \rho_r \cdot \mathbb{I}, \text{ in } \Omega_r \end{cases} = \begin{cases} \dfrac{(n-1)E_c}{J_c^n} J_i^2 \left\|\mathbf{J}\right\|^{n-3} + \dfrac{E_c}{J_c^n} \left\|\mathbf{J}\right\|^{n-1}, & i = j \text{ in } \Omega_s \\ \dfrac{(n-1)E_c}{J_c^n} J_i J_j \left\|\mathbf{J}\right\|^{n-3} & , i \neq j \text{ in } \Omega_s \\ \rho_r & , i = j \text{ in } \Omega_r \\ 0 & , i \neq j \text{ in } \Omega_r \end{cases} \tag{4}$$

L' approche type Galerkin discontinue, de part sa méthodologie couple les méthodes des éléments finis et des volumes finis . Son principal avantage est qu'elle est adaptée au calcul parallèle car les matrices issues de la discrétisation sont diagonales par blocs. Le maillage du domaine étudié est ainsi distribué sur tous les noyaux d'une architecture hardware. Une telle caractéristique évite des problèmes de limitations de mémoire généralement rencontrés lorsque de larges problèmes sont résolus grâce aux éléments finis.

A la différence de l'usage des élements d'arêtes pour l'application des méthodes éléments finis sur des formulations en champs magnétique **H**, l'approche Galerkin discontinue utilisera une approximation nodale. Une pénalisation bien définie des termes d'interfaces est indispensable afin d'assurer la continuité de la composante tangentielle du champ magnétique.

Afin de valider ces approches numériques, un cube supraconducteur soumis à un champ magnétique sinusoïdal transverse fut modélisé en 3D pour des cas avec et sans couplage thermique. Les pertes AC générées furent évaluées et comparées pour ces deux approches avec des résultats obtenus sous le logiciel éléments finis Comsol. On observe bien une équivalence des pertes AC calculées mais une différence non-négligeable en terme de mémoire allouée aux calculs pour les différentes approches.

Un cas de modélisation 3D du comportement électromagnétique sans couplage thermique d'un câble supraconducteur mono-filamentaire droit transportant du courant fut aussi implémenté. La comparaison des pertes AC calculées montre aussi une équivalence de l'approche type Galerkin discontinue et celle de type éléments finis implémentée sous GetDP. La différence en terme de taille de mémoire allouée est toujours présente.

Ces cas de simulations montrent la validité des deux approches numériques développées.

L'approche type Galerkin discontinue permet, grâce au calcul parallèle, d'éviter toutes limitations de mémoire. Cette caractéristique rend cette approche potentiel-

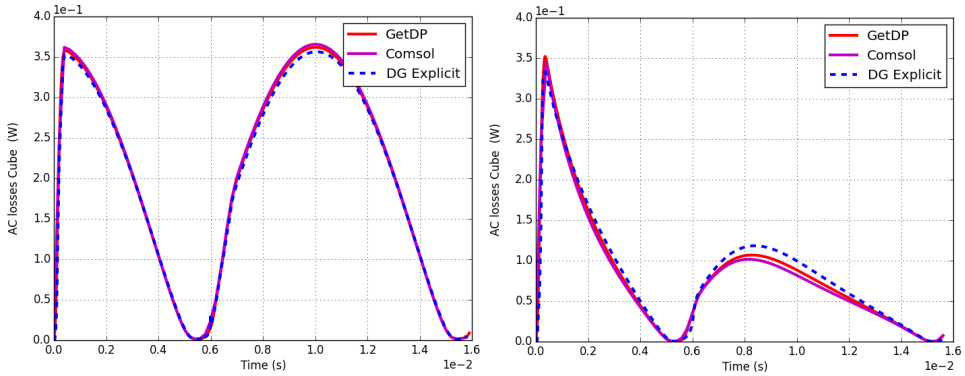

(a) Aucun couplage thermique (b) Couplage thermique

FIGURE 1 – Pertes AC générées par un cube supraconducteur soumis à un champ magnétique sinusoïdal transverse.

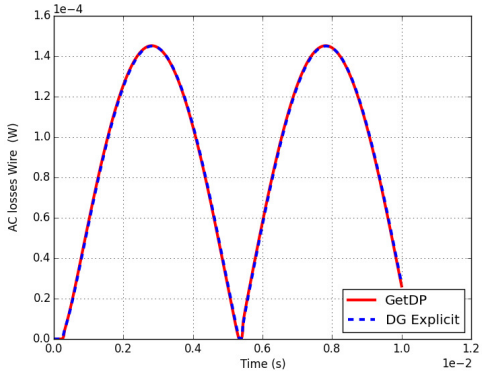

FIGURE 2 – Pertes AC générées par un câble supraconducteur mono-filamentaire droit transportant du courant.

lement appropriée pour la modélisation tridimensionnelle de larges systèmes supraconducteurs tel que des supraconducteurs multifilamentaires torsadés. De plus, de nombreuses perspectives de recherche afin d'optimiser cette approche, telles que du calcul sur GPU par exemple, sont envisageables.

Cependant, la modélisation tridimensionnelle, via les éléments finis, de câbles supraconducteurs multifilamentaires torsadés nécessite des méthodes permettant de simplifier considérablement le problème. Ces dernières permettraient de pallier les potentiels problèmes de limitations de mémoire dues aux larges géométries complexes de ces types de câbles.

Modélisation 3D de supraconducteurs multifilamentaires torsadés

Une évaluation précise des pertes AC générées par des câbles supraconducteurs multifilamentaires torsadés nécessite en plus d'outils numériques robustes de modélisation 3D, d'approches numériques permettant de simplifier considérablement ce type problème.

Ces dites méthodes sont développées et décrites dans le chapitre 3. Au regard

des tailles raisonnables des géométries étudiées dans la suite, l'outil de modélisation 3D utilisé pour ces travaux est GetDP.

Dans un premier temps, une étude de modélisation est réalisée sur un câble supraconducteur mono-filamentaire torsadé sujet à un champ magnétique sinusoïdal transverse. De cette étude, l'on note l'apparition de plusieurs boucles de courant électrique dans le câble. Ainsi, le champ magnétique vu par le filament supraconducteur torsadé du câble ne semblait pas être unidirectionnel mais ce dernier parcourt plutôt la trajectoire hélicoidale décrite par le filament.

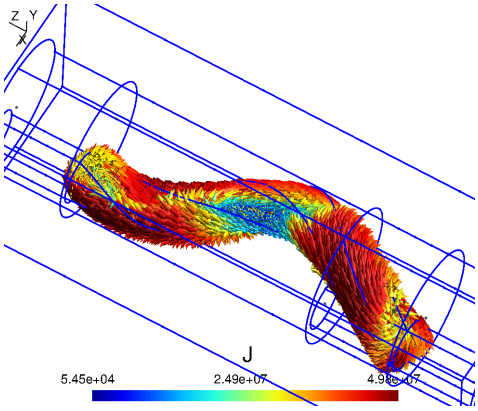

FIGURE 3 – Distribution 3D du courant dans le câble supraconducteur mono-filamentaire torsadé à $t = T/4s$ et dans le repère $(\mathbf{x}, \mathbf{y}, \mathbf{z})$.

Ces observations furent validées par l'application d'une transformation géométrique uniquement sur le champ magnétique transverse initialement imposé sur le filament torsadé. La dite transformation exprime le passage du repère $(\mathbf{x}, \mathbf{y}, \mathbf{z})$ au repère de Frenet $(\mathbf{T}, \mathbf{N}, \mathbf{K})$ associé à la trajectoire hélicoidale décrite par le filament torsadé :

$$\mathbf{H}_{[\mathbf{T},\mathbf{N},\mathbf{K}]} = \begin{bmatrix} -a \cdot sin(\theta) & a \cdot cos(\theta) & b \\ cos(\theta) & sin(\theta) & 0 \\ -b \cdot sin(\theta) & b \cdot cos(\theta) & -a \end{bmatrix} \cdot \mathbf{H}_{[\mathbf{x},\mathbf{y},\mathbf{z}]} \tag{5}$$

avec $a = r/L$, $b = c/L$, $c = p/2\pi$, $L^2 = r^2 + c^2$, et $\theta = z/c$ où p est le pas de torsadage et r le rayon de l'hélice. Le rayon r depend de la taille des surfaces de base du domaine de l'air entourant le câble sur le modèle. En effet pour une boîte d'air ce rayon r sera la moitié de la longueur de la diagonale tandis que pour un cylindre comme domaine d'air, le rayon r sera celui des surfaces de base.

De cette transformation du champ magnétique imposé sur ce câble mono-filamentaire torsadé, on retrouve une unique boucle de courant dans le filament. Ce résultat est équivalent au cas d'un filament droit soumis à un champ transverse dans le repère $(\mathbf{x}, \mathbf{y}, \mathbf{z})$. Il confirme ainsi notre hypothèse de départ sur la direction du champ.

Afin de complètement valider cette transformation, une étude paramétrique avec comme variables le nombre total de filaments, le pas de torsadage, l'amplitude et la direction du champ magnétique imposé est réalisée. Cette étude regroupe de nombreux cas de simulations ayant pour but de comparer les pertes AC générées par le câble dans le repère $(\mathbf{x}, \mathbf{y}, \mathbf{z})$ où ses filaments sont torsadés avec celles dans

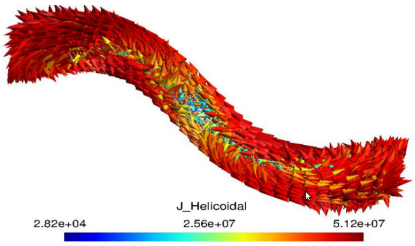

FIGURE 4 – Distribution 3D du courant dans le câble supraconducteur monofilamentaire torsadé à $t = T/4s$ et dans le repère de Frenet $(\mathbf{T}, \mathbf{N}, \mathbf{K})$.

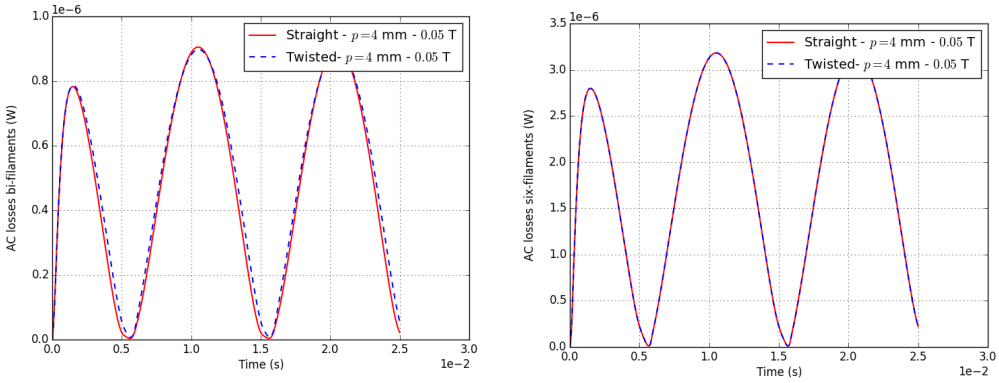

(a) 2 filaments (b) 6 filaments

FIGURE 5 – Pertes AC générées, dans les repères $(\mathbf{x}, \mathbf{y}, \mathbf{z})$ et $(\mathbf{T}, \mathbf{N}, \mathbf{K})$, par des câbles multifilamentaires supraconducteurs de longueur $p = 4$mm soumis à un champ magnétique sinusoïdal transverse .

le repère de Frenet $(\mathbf{T}, \mathbf{N}, \mathbf{K})$ où ses filaments sont droits. On observe bien une équivalence des deux configurations quel que soit les paramètres définis.

Malgré une telle équivalence, la modélisation tridimensionnelle de câbles supraconducteurs multifilamentaires torsadés comporte toujours un large nombre de degrés de liberté. Celà résulte du grand nombre de torsades que comporte généralement de tels câbles. Afin de rémédier à ce problème, on a pu observer, avec de nombreuses simulations utilisant la transformation dans le repère de Frenet, qu'un câble avec un nombre minimal de torsades pouvait être représenté, en termes de pertes AC par unité de longueur, de façon équivalente par un modèle réduit d'une de ses torsades située en son centre. Ce modèle réduit comportera des conditions de périodicité à ses extrémités.

L'idée d'une telle approche réside dans l'approximation de la quantité de courant moyen traversant la torsade situé au centre du câble si les effets magnétiques des extrémités du câble en son centre deviennent négligeables. La modélisation approximative du centre du câble donne ainsi une idée de ce courant moyen ainsi que des pertes AC par unité de longueur associées.

En considérant le modèle réduit à la torsade centrale au câble, on s'est interessé à ce qui se passe en son milieu. On a alors étudié des fractions de cette torsade dans le but de réduire le modèle.

Cette diminution de longueur du modèle réduit permet de considérablement diminuer le nombre de degrés de liberté du problème.

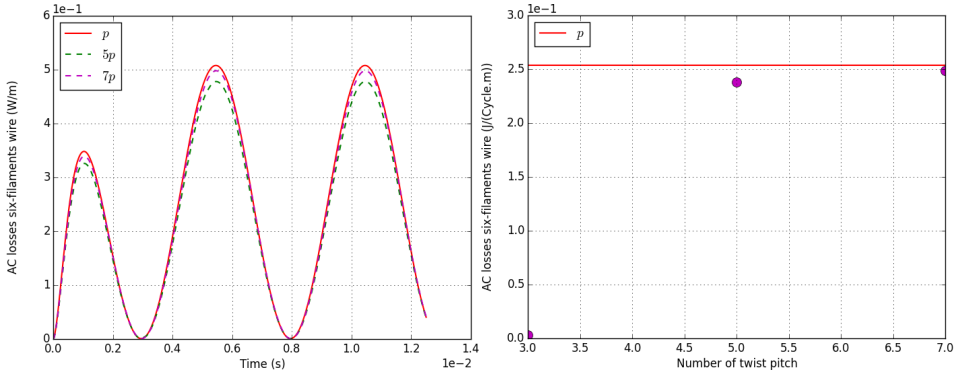

(a) Pertes AC instantanées (b) Pertes AC moyenne

FIGURE 6 – Comparaison et évolution des pertes AC d'un câble supraconducteur sujet à un champ sinusoïdal transverse en fonction du nombre de torsades par rapport aux pertes AC d'une torsade comme modèle réduit.

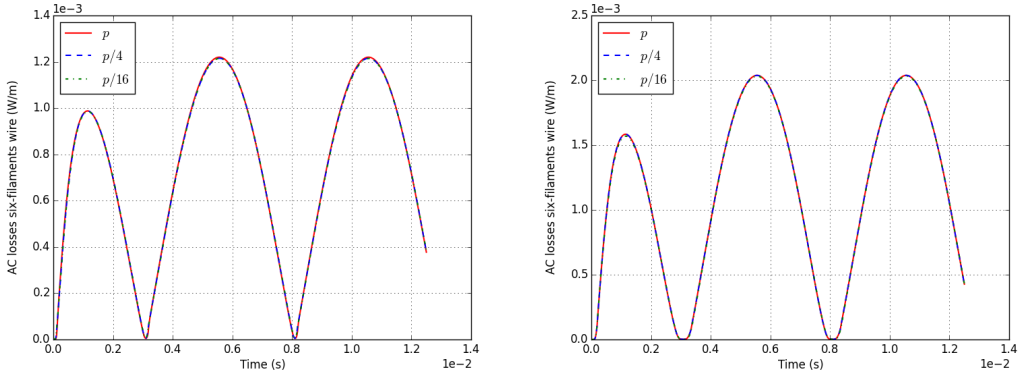

(a) Champ transverse (b) Champ axial

FIGURE 7 – Comparaison des pertes AC d'un câble supraconducteur pour différents modèles réduits.

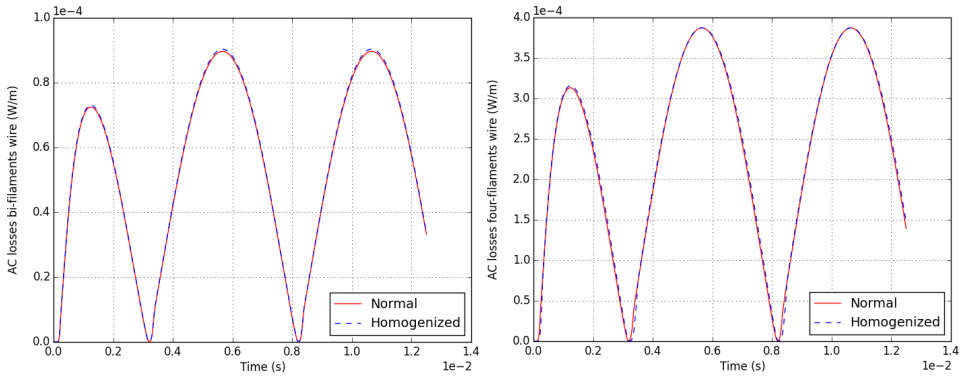

(a) 2 filaments (b) 4 filaments

FIGURE 8 – Pertes par aimantation de câbles supraconducteurs, évaluée dans le repère de Frenet, avec 2 et 4 filaments torsadés et leur version homogénéisée soumis à un champ magnétique transverse - $B_{max} = 50$ mT, $f = 100$ Hz et $p = 4$ mm

Ces approches couplant la transformation dans le repère de Frenet et les modèles réduits de câbles supraconducteurs multifilamentaires torsadés permettent de simplifier la modélisation 3D et d'accélérer la conception optimisée de ces types de câbles.

Ils ont ainsi permis de modéliser en 3D l'influence du champ elliptique sur les pertes par aimantation d'un échantillon de 100 câbles de MgB_2 multifilamentaires torsadés.

A partir de l'étude de câbles comportant une seule couche de filaments, on montre la possibilité d'homogénéiser ces câbles afin d'évaluer de façon équivalente les pertes AC par unité de longueur.

Dans ce contexte, les volumes des différents sous-domaines sont conservés ainsi que chacune de leur géometrie excepté celle du sous-domaine supraconducteur. Ce dernier est représenté par un unique filament centrée de longueur équivalente à celle du câble. De nouveaux paramètres de la loi puissance doivent être définis comme étant fonctions de différents paramètres tel que :

$$J_{ch} = G(J_c, n_f, \alpha_v, \beta_{r_f}, \beta r_L) \tag{6}$$

and

$$n_h = g(n, n_f, \alpha_v, \beta_{r_f}, \beta r_L) \tag{7}$$

Ces fonctions dépendent du nombre de filaments n_f appartenant à une couche, du ratio volumique α_v des filaments supraconducteurs par rapport à la matrice résistive, de la distribution radiale β_{r_f} des filaments sur les couches et la distribution radiale βr_L des couches des filaments. Pour notre étude, ces fonctions furent évaluées empiriquement afin de servir de base pour de futures recherches visant à les définir explicitement.

Conclusion

Les approches éléments finis et Galerkin discontinue ont été mise en place pour déterminer les champs induits dans des supraconducteurs et notamment évaluer

les pertes dans les câbles multifilamentaires.

Dans un premier temps, il s'agit de résoudre les problèmes liés à la modélisation tridimensionnelle des supraconducteurs. Pour celà, l'approche type éléments finis prenant en compte la linárisation de la loi puissance ainsi que l'approche de type Galerkin discontinue, adaptée au calcul parallèle, furent mise en place pour la résolution de problèmes en champ magnetique $\mathbf{H}$. Elles furent validées sur des cas simples avec des résultats réferences issus d'une approche type élements finis implémentée sur Comsol.

Puis, la réduction et simplification des larges problèmes associés à la modélisation tridimensionnelle de câbles supraconducteurs multifilamentaires est indispensable car l'étude des configurations réelles de câbles nécessiterait des maillages à des millions d'inconnues. De ce fait, une transformation géométrique fut proposée et validée afin de résoudre un problème 3D équivalent dans le repère de Frenet. Dans ce repère les filaments torsadés deviennent droits et le champ appliqué devient hélicoïdal.

A partir de ce problème 3D équivalent, des modèles réduits de ces câbles permettant l'évaluation rapide et simplifiée des pertes AC par unité de longueur furent proposées et validées. Ils ont permis de modéliser en 3D l'influence du champ elliptique sur les pertes par aimantation d'un échantillon de 100 câbles de MgB_2 avec 54 filaments torsadés.

Enfin, l'homogénéisation de ces types de câbles représente une perspective de recherche. Les résultats présentés montrent la faisabilité et les potentialités d'une telle approche pour la conception optimisée de ces câbles.

Contents

General Introduction **1**

1 Superconductivity and numerical modelling **5**

1.1 Introduction . . . 5
1.2 Superconductors : types I and II . . . 7
1.2.1 Type-I superconductors . . . 7
1.2.2 Type-II superconductors . . . 8
1.3 HTS: macroscopic models . . . 10
1.3.1 Critical state model : Bean model . . . 11
1.3.2 E-J power law . . . 11
1.3.3 Kim model . . . 12
1.3.4 AC losses . . . 12
1.4 HTS applications . . . 14
1.5 Mathematical models . . . 16
1.5.1 $\mathbf{H}$ formulation . . . 18
1.5.2 $\mathbf{E}$ formulation . . . 18
1.5.3 $\mathbf{A} - V$ formulation . . . 18
1.5.4 $\mathbf{T} - \phi$ formulation . . . 19
1.6 Numerical methods . . . 20
1.6.1 Minimization of an energy functional . . . 20
1.6.2 Integral methods . . . 21
1.6.3 Finite element method . . . 22
1.6.4 Finite volume method . . . 23
1.6.5 Finite element - Finite volume hybrid method . . . 24
1.6.6 Discontinuous Galerkin method . . . 25
1.7 Conclusion . . . 26

2 3D modelling of high-temperature superconductors **29**

2.1 Introduction . . . 29
2.2 Problem formulation . . . 30
2.2.1 Constitutive laws . . . 30
2.2.2 Differential formulation . . . 31
2.2.3 Variational formulation . . . 32
2.3 Finite element method . . . 33
2.3.1 Mesh definition . . . 34
2.3.2 Discrete variational formulation . . . 34
2.3.3 Numerical treatment of the non-linearities arising from $\mathbf{E} = \rho(\mathbf{J})\mathbf{J}$ . . . 36

2.4 Discontinuous Galerkin method 39
2.4.1 Mesh definition 39
2.4.2 Discrete Variational formulation 40
2.4.3 Spatial approximation 43
2.4.4 Numerical fluxes terms on the faces of the mesh $\mathcal{T}_h$ 45
2.4.5 Boundary conditions 50
2.4.6 Numerical treatment of the non-linearities arising from $\mathbf{E} = \rho(\mathbf{J})\mathbf{J}$ 51
2.5 Comparisons and validations 52
2.5.1 Straight superconducting filament embedded in a Niobium matrix carrying a sinusoidal transport current 52
2.5.2 Superconducting cube subjected to an alternating transverse magnetic field 52
2.6 Conclusion 56

3 3D modelling of twisted multi-filamentary superconducting wires 57
3.1 Introduction 57
3.2 Influence of a transverse magnetic field on a twisted mono-filament wire 58
3.3 Mapping from a twisted mono-filament wire to a straight mono-filament wire 60
3.4 Mapping validation on a twisted bi-filaments wire 63
3.4.1 Twisted bi-filaments superconducting wire subjected to a transverse magnetic field along the y-axis 65
3.4.2 Twisted bi-filaments superconducting wire subjected to an axial magnetic field along the z-axis 69
3.5 Mapping validation on a twisted six-filaments wire 73
3.5.1 Twisted six-filaments superconducting wire subjected to a transverse magnetic field along the y-axis 77
3.5.2 Twisted six-filaments superconducting wire subjected to an axial magnetic field along the z-axis 80
3.6 Study of multi-filamentary wires with multiple twist pitch 83
3.6.1 Influence of the number of twist pitch 84
3.6.2 Model-order reduction of a twisted multi-filamentary wire with multiple twist pitch 87
3.6.3 Analysis of the impact of elliptical fields on magnetization losses 89
3.7 Perspective : homogenization of multi-filamentary superconducting wire 93
3.8 Conclusion 96

General conclusion 99

Bibliography 101

List of Figures

1 Pertes AC générées par un cube supraconducteur soumis à un champ magnétique sinusoïdal transverse. v

2 Pertes AC générées par un câble supraconducteur mono-filamentaire droit transportant du courant. v

3 Distribution 3D du courant dans le câble supraconducteur mono-filamentaire torsadé à $t = T/4s$ et dans le repère $(\mathbf{x}, \mathbf{y}, \mathbf{z})$. vi

4 Distribution 3D du courant dans le câble supraconducteur mono-filamentaire torsadé à $t = T/4s$ et dans le repère de Frenet $(\mathbf{T}, \mathbf{N}, \mathbf{K})$. vii

5 Pertes AC générées, dans les repères $(\mathbf{x}, \mathbf{y}, \mathbf{z})$ et $(\mathbf{T}, \mathbf{N}, \mathbf{K})$, par des câbles multifilamentaires supraconducteurs de longueur $p = 4$mm soumis à un champ magnétique sinusoïdal transverse vii

6 Comparaison et évolution des pertes AC d'un câble supraconducteur sujet à un champ sinusoïdal transverse en fonction du nombre de torsades par rapport aux pertes AC d'une torsade comme modèle réduit. viii

7 Comparaison des pertes AC d'un câble supraconducteur pour différents modèles réduits. viii

8 Pertes par aimantation de câbles supraconducteurs, évaluée dans le repère de Frenet, avec 2 et 4 filaments torsadés et leur version homogénéisée soumis à un champ magnétique transverse - $B_{max} = 50$ mT, $f = 100$ Hz et $p = 4$ mm ix

1.1 Critical temperatures and year of discovery for different superconductors [3]. 6

1.2 Characteristics of superconductors 7

1.3 Phase diagram of type-I superconductors 8

1.4 Phase diagram of type-II superconductors 9

1.5 Magnetic behaviour characteristics of both type-I and type-II superconductors 9

1.6 The mixed state with fluxon lattices and encircling supercurrent [9] 10

1.7 HTS rotating machine [38]. 15

2.1 Mapping from D to I 43

2.2 AC losses in the non-thermal case of a superconducting wire carrying a transport current computed with GetDP and the discontinuous galerkin method (DG) with the non-linear resistivity evaluated explicitly. 53

2.3 AC losses in the non-thermal case of a superconducting cube subjected to an external magnetic field computed with GetDP, Comsol and the discontinuous galerkin method (DG) with the non-linear resistivity evaluated explicitly. 54
2.4 Temperature distribution at $t = 20$ ms in the superconducting cube. 55
2.5 AC losses in the thermal case of a superconducting cube subjected to an external magnetic field computed with GetDP, Comsol and the discontinuous galerkin method (DG) with the non-linear resistivity evaluated explicitly. 55

3.1 3D current density distribution inside the filament at $t = T/4s$ . . . 59
3.2 3D filament subjected to a transverse magnetic field in the Frenet frame 62
3.3 3D current density distribution inside the filament in the Frenet frame at $t = T/4s$ 63
3.4 Filaments of both twisted and equivalent straight bi-filaments superconducting wire of length $p = 4$ mm 65
3.5 AC losses comparison of a bi-filaments superconducting wire of different twist pitch lengths subjected to a transverse magnetic field with $B_{max} = 50$ mT in both the initial and Frenet frames. 66
3.6 Current density vector distribution at $t = 1.5$ ms inside the superconducting domain of a bi-filaments superconducting wire of length $p = 4$ mm subjected to a transverse magnetic field with $B_{max} = 50$ mT in both the initial and Frenet frames. 67
3.7 Magnetization losses and computed average magnetization along the y-axis comparison of a bi-filaments superconducting wire of twist pitch length subjected to a transverse magnetic field with $B_{max} = 50$ mT in both the initial and Frenet frames. 68
3.8 AC losses comparison of a bi-filaments superconducting wire of of different twist pitch lengths subjected to a transverse magnetic field with $B_{max} = 100$ mT in both the initial and Frenet frames. 69
3.9 AC losses comparison of a bi-filaments superconducting wire of of different twist pitch lengths subjected to a transverse magnetic field with $B_{max} = 200$ mT in both the initial and Frenet frames. 70
3.10 AC losses comparison of a bi-filaments superconducting wire of of different twist pitch lengths subjected to an axial magnetic field with $B_{max} = 50$ mT in both the initial and Frenet frames. 71
3.11 Current density vector distribution at $t = 1.5$ ms inside the superconducting domain of a bi-filaments superconducting wire of length $p = 4$ mm subjected to an axial magnetic field with $B_{max} = 50$ mT in both the initial and Frenet frames. 72
3.12 Magnetization losses and computed average magnetization along the y-axis comparison of a bi-filaments superconducting wire of twist pitch length subjected to an axial magnetic field with $B_{max} = 50$ mT in both the initial and Frenet frames. 73
3.13 AC losses comparison of a bi-filaments superconducting wire of of different twist pitch lengths subjected to an axial magnetic field with $B_{max} = 100$ mT in both the initial and Frenet frames. 74

3.14 AC losses comparison of a bi-filaments superconducting wire of of different twist pitch lengths subjected to an axial magnetic field with $B_{max} = 200$ mT in both the initial and Frenet frames. 75
3.15 Filaments of both twisted and equivalent straight six-filaments superconducting wire of length $p = 4$ mm 76
3.16 AC losses comparison of a six-filaments superconducting wire of different twist pitch lengths subjected to a transverse magnetic field with $B_{max} = 50$ mT in both the initial and Frenet frames. 77
3.17 Magnetization losses and computed average magnetization along the y-axis comparison of a six-filaments superconducting wire of twist pitch length subjected to a transverse magnetic field with $B_{max} = 50$ mT in both the initial and Frenet frames. 78
3.18 AC losses comparison of a six-filaments superconducting wire of different twist pitch lengths subjected to a transverse magnetic field with $B_{max} = 100$ mT in both the initial and Frenet frames. 79
3.19 AC losses comparison of a six-filaments superconducting wire of different twist pitch lengths subjected to a transverse magnetic field with $B_{max} = 200$ mT in both the initial and Frenet frames. 80
3.20 AC losses comparison of a six-filaments superconducting wire of different twist pitch lengths subjected to an axial magnetic field with $B_{max} = 50$ mT in both the initial and Frenet frames. 81
3.21 Magnetization losses and computed average magnetization along the y-axis comparison of a six-filaments superconducting wire of twist pitch length subjected to an axial magnetic field with $B_{max} = 50$ mT in both the initial and Frenet frames. 82
3.22 AC losses comparison of a six-filaments superconducting wire of different twist pitch lengths subjected to an axial magnetic field with $B_{max} = 100$ mT in both the initial and Frenet frames. 83
3.23 AC losses comparison of a six-filaments superconducting wire of different twist pitch lengths subjected to an axial magnetic field with $B_{max} = 200$ mT in both the initial and Frenet frames. 84
3.24 Total ac losses comparison in the Frenet frame of a twisted six-filaments superconducting wire subjected and its truncated version to a transverse magnetic field 86
3.25 Evolution of the AC losses per unit length with respect to the number of twist pitch of the wire 86
3.26 Magnetization losses comparison of truncated twisted six-filaments superconducting wires subjected to a transverse magnetic field along the y-axis 87
3.27 Magnetization losses comparison of truncated six-filaments superconducting wire subjected to an axial magnetic field along the z-axis 88
3.28 Magnetization losses per unit length of a pseudo-2D representation in the Frenet frame of a truncated six-filaments superconducting wire subjected to a transverse magnetic field along the y-axis . . . 89
3.29 Magnetization losses experimental vs numerical comparison of a twisted 54-filaments MgB_2 wire subjected to an elliptic field at 50 Hz 91
3.30 Magnetization losses experimental vs numerical comparison of a twisted 54-filaments MgB_2 wire subjected to an elliptic field at 110 Hz 91

3.31 Computed instanteneous magnetization losses of reduced models of the twisted 54-filaments MgB_2 wire subjected to an elliptic field at 50 Hz 92
3.32 Computed instanteneous magnetization losses of reduced models of the twisted 54-filaments MgB_2 wire subjected to an elliptic field at 110 Hz 92
3.33 Pseudo-2D representation in the Frenet frame of twisted multifilamentary superconducting wire subjected to a transverse magnetic field in the Frenet frame. 94
3.34 Pseudo-2D representation in the Frenet frame of the homogenized twisted multifilamentary superconducting wire subjected to a transverse magnetic field in the Frenet frame. 94
3.35 Magnetization losses per unit length of a pseudo-2D representation in the Frenet frame of the pseudo-2D representation of twisted superconducting wires in the Frenet frame. 96

List of Tables

1.1 HTS Synchronous motors developed 16

3.1 Bi-filaments superconducting wire parameters 64
3.2 Six-filaments superconducting wire parameters 76
3.3 Parameters of a six-filaments superconducting wire with multiple twist pitch 85
3.4 Parameters of twisted multi-filamentary wire with multiple twist pitch for homogenization 95

General Introduction

The rising global energy consumption coupled with the finite supply of fossil energy ushered a new wave of research initiatives geared to develop more efficient and robust renewable energy alternatives. These initiatives are aimed at developing technologies which use abundant energy with respect to the environment. Such technologies involve for instance electrical machines which are ubiquitous in numerous industries. Those devices are generally characterized by non-negligible dissipated energy, from electric cables carrying current, as heat losses.

In the case of electrical machines, electric cables carrying high currents, more than the usual conventional materials such as copper, with minimal losses can be a perfect alternative. Fortunately, high temperature superconducting materials provide interesting properties for such application. In fact, high temperature superconductors can carry high direct currents (DC) with minimal to zero losses when used in an environment with cryogenic temperatures. In such state, the resistivity of the superconductors remain close to zero if the temperature, the magnetic field density and the current intensity are respectively below the critical temperature T_c, the critical magnetic field density B_c and the critical current density I_c.

However, high alternating currents (AC) carried by those materials can lead them to dissipate heat because of the magnetic induction. The energy dissipated is commonly called AC losses. Its precise evaluation is therefore critical in order to design efficient cables for electrical machines. Moreover, the design of the associated cryogenic system, whose function is to maintain, from a thermal standpoint, the cable in a superconducting state, require an accurate value of those losses.

The need of accuracy in evaluating AC losses requires strong mathematical tools. Despite the existence of analytical tools, superconducting machines commonly using multiple superconductors in tape/wire form wound into coils and interacting together in a complex magnetic environment make them insufficient. Thus, robust and efficient numerical tools must be investigated and developed in order to accurately model superconductors. Several developments have been made

in that direction with considerable amount of work geared towards 2D modelling. The aspect regarding 3D modelling have known some interesting developments except in the case of large scale systems such as multi-filamentary superconducting wires.

In this dissertation, several numerical approaches geared toward an accurate 3D modelling of whole twisted multi-filamentary superconducting wires will be developed. The main focus is to simplify and reduce the associated 3D problem of such wires for fast and efficient AC losses computations. In fact, a typical 3D problem for modelling those wires requires a large number of degrees of freedom coupled with complexities arising from the twisted multi-filamentary wire geometry. Thus, reduced model of truncated version of those wires will help us derive the complete electro-magnetic behaviour of the whole wires through fast and efficient computations.

The chapter 1 set the overall picture of the research work involved. An introduction to the superconductivity followed by an understanding of loss mechanisms are mentioned. Moreover, applications, mostly involving large systems, are described in order to show the current and future developments involving superconductivity. Then, the modelling aspect is introduced with the different mathematical models and numerical methods investigated by the applied superconductivity community. With some detailed descriptions of those numerical approaches, their limitations in regards with 3D modelling of large and complex superconducting systems are stated.

Given those limitations, two numerical approaches applied on the magnetic field $\mathbf{H}$ based formulation are presented in the chapter 2. The first one is the finite element method with a focus on the treatment of non-linearities arising from the electrical behaviour of high-temperature superconductors. Then, the discontinuous galerkin method will be introduced in order to make use of its numerous capabilities such as distributed computing for electromagnetism 3D modelling. With a thermo-electromagnetic consideration, several simple cases, subjected to different magnetic field configurations, are validated with simulations using finite element method implemented in GetDP and Comsol Multiphysics.

Finally, an extensive study on the 3D modelling of twisted multi-filamentary superconducting wires have been done in the chapter 3. Given the geometric complexities present in the wire, the purpose was to develop numerical approaches which simplify the 3D modelling of such wires based on the finite element method. A mathematical framework is thus proposed to solve an equivalent straight wire mod-

elling problem with a significant reduced number of unknowns. Thus, capabilities of this framework led to develop a model-order reduction which model accurately and quickly in 3D the electro-magnetic behaviour of twisted multi-filamentary superconducting wires. With the use of GetDP, numerous simulations on smaller versions of these wires were done in order to validate the proposed framework. Then this new model was applied on a study of the influence of elliptical magnetic fields on the magnetization losses of a twisted MgB_2 twisted wire with 54 filaments. As research perspectives, homogenization approaches are investigated briefly in order to show the optimization wire design potentialities.

Chapter 1

Superconductivity and numerical modelling

1.1 Introduction

Superconductivity was first discovered in 1911 by Kamerlingh Onnes. In his experiments with liquid helium, Onnes observed that the electrical resistance of metals such as mercury, lead and tin sharply disappeared below a low critical temperature, T_c, characteristic of each material (4.15 Kelvins (K) for the mercury, 7.19 K for the lead and 3.72 K for the tin)[1]. The metals, characterized by a perfect conduction, were observed in a superconductor state. Perfect diamagnetism of superconductors was discovered later in 1933 in superconductors by Meissner and Ochsenfeld. In such case, the applied magnetic field was expelled by superconductors, at temperatures below T_c, except for a distance of λ known as the penetration depth [2]. This became known as the Meissner effect.

Above their critical temperature T_c, superconductors are in normal state which is common to the electrical behaviour of resistive materials.

Years later, different superconductors have been discovered with an increasing critical temperature.

Metallic elements and alloys, whose superconducting state is observed below 30 K have been named low temperature superconductors (LTS). Some oxide compounds named high-temperature superconductors (HTS) were discovered with a superconducting state observed above $30K$. With the growing interest and research in superconductivity, the critical temperature has been increasing and now may exceed 130 K for certain oxide superconductors, see fig. 1.1. The higher the critical temperature T_c, the easier is the design and maintenance of cryogenic systems

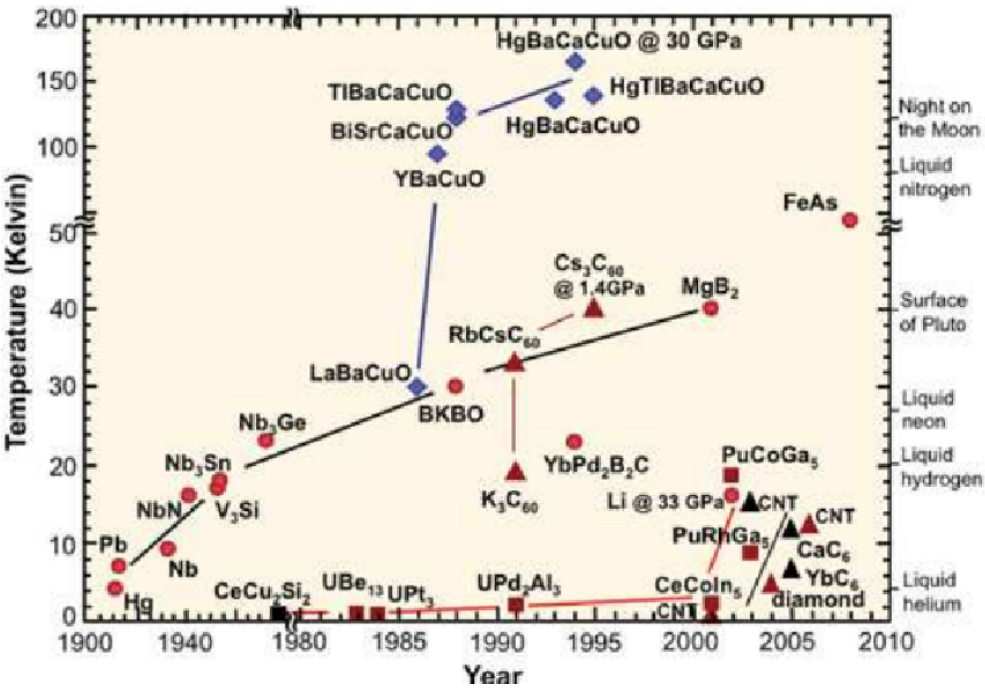

Figure 1.1 – Critical temperatures and year of discovery for different superconductors [3].

needed to cool down the superconductors in their applications.

A superconductor is thus characterised by its critical temperature, T_c, its critical magnetic field, H_c, and its critical current density, J_c, as shown in figure 1.2. These parameters define the upper limits for the superconductivity in a material and can be used to define a superconducting or normal state for a given set of conditions [4]. The shaded volume in this figure corresponds to the material being in its superconducting state.

In the last few years, the development of high-temperature superconducting devices increased. Several prototypes and some commercial devices have been built. However, many of those devices costs remain high and potential solutions to reduce it are being proposed and explored. Moreover, other important practical aspects such as cooling systems must be taken in consideration for real applications.

The complexities associated with the devices geometries and overall highly non-linear behaviour in real applications led to the development of efficient numerical modelling tools. Those tools will help deepen the understanding of the behaviour of HTS devices. They will also allow the optimization of those devices performances while helping reduce their associated costs.

Beyond the behaviour and the optimization of those devices, numerical modelling tools can also be used to predict how a device will perform in its environment

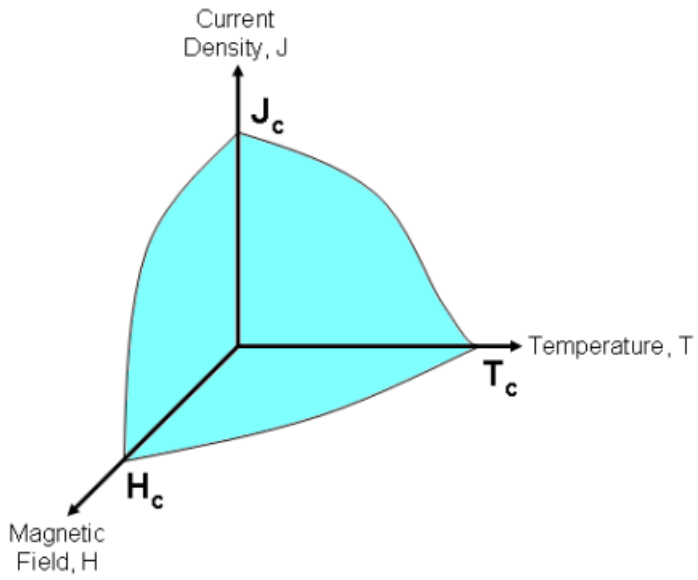

Figure 1.2 – Characteristics of superconductors

once in operation. In other words, a device rarely operates alone, but acts on its neighbourhood as one element of a system. A good example of this is a superconducting power device installed in a power system. Since the final performance of a device is conditioned by the system in which it is installed, it is of the highest importance to develop device models that are compatible with system simulators. These device models, most often expressed in terms of electric circuits, are in general simpler than those used for device optimization, for instance finite element models, but they are nonetheless essential for comparing the performance of competing technologies in a given system.

In this chapter, characteristics and constitutive laws of superconductors will be explored. Moreoever, models and numerical methods, applied on modelling high temperature superconductors and found in the literature, will be presented with mentions of their advantages and limitations. A focus on their limitations will help derive the need of a robust and scalable approach to model superconducting devices in three-dimensions.

1.2 Superconductors : types I and II

1.2.1 Type-I superconductors

They consist of pure metals with a critical temperature below 10 K. The Meissner effect or perfect diamagnetism characterizes the behaviour of type-I superconduc-

tors below the critical magnetic field H_c. Above H_c the type-I superconductor becomes normal and the magnetic field fully penetrates the material (see Fig. 1.3).

During the Meissner effect, a current flow combined with a self-induced magnetic field are created and confined in the outer layer of the superconductor. Thus, the current-capacity of type-I superconductors becomes limited.

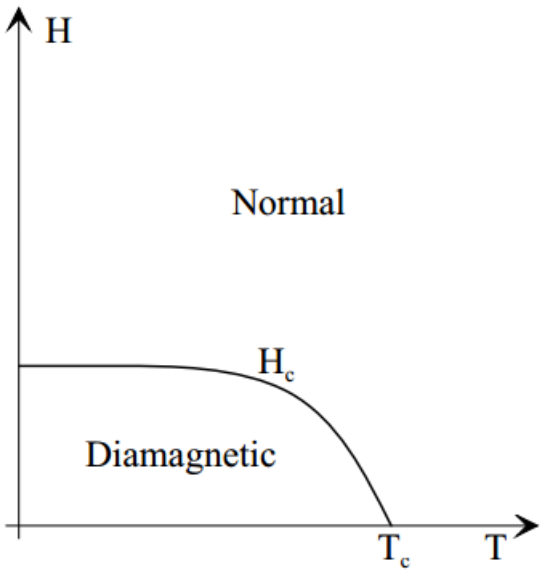

Figure 1.3 – Phase diagram of type-I superconductors

According to Silsbee's criterion, only valid for type-I, a superconductor loses its zero resistance when at any point on the surface the total magnetic field strength (due to the transport current and applied magnetic field) exceeds H_c[5]. The maximum current that can be carried by a type-I superconductor is called critical current intensity I_c. For currents above I_c, the self-induced magnetic field will be large enough to bring on transition to a normal state[6].

1.2.2 Type-II superconductors

The discovery and development of superconducting metal alloys led to the existence of another superconductors class known as type-II superconductors. In 1957, Abrikosov contributed to the behaviour study of this class. According to his research, they exhibited a continuous increase in flux penetration starting at a first critical field till reaching $B = \mu_0 H$ at a second critical field H_{c2}, instead of showing a discontinuous disappearance of superconductivity at the critical magnetic field H_c (see Fig.1.5)[7]. It is now known that the behaviour of this new class was not simply due to impurities in their chemical composition but were intrinsic properties[8].

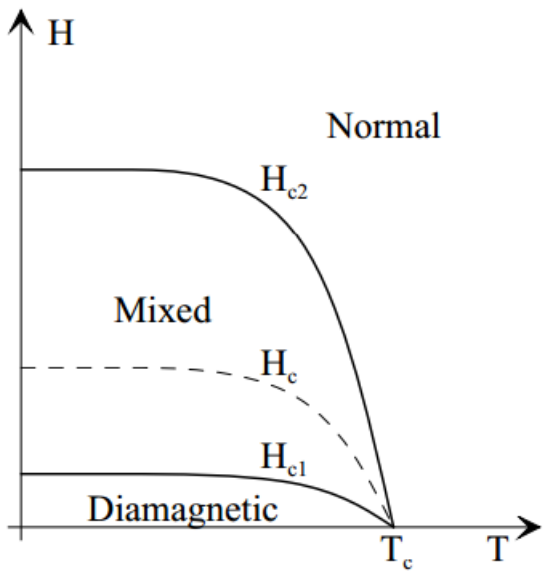

Figure 1.4 – Phase diagram of type-II superconductors

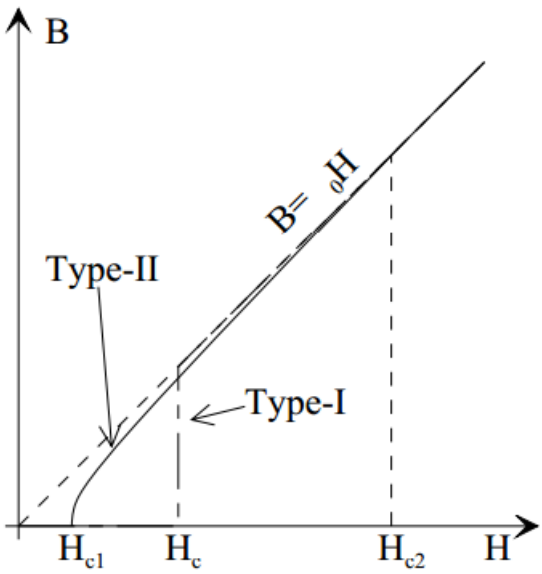

Figure 1.5 – Magnetic behaviour characteristics of both type-I and type-II superconductors

Moreover, they are also characterized by a new phase called mixed state between the critical magnetic field H_{c1} and H_{c2} (see Fig.1.4). In such state, both the Meissner state and the superconducting state are present. The negative surface energy between normal regions and superconducting regions led to the appearance of cylindrical normal regions in order to attain the lowest total free energy state possible [9]. Those cylindrical normal regions, called vortices or fluxons, are distributed in a regular pattern called fluxon lattices (see Fig. 1.6). Each vortice let

the applied magnetic field pass through and is shielded from the neighbouring superconducting regions by a vortex of induced currents called super-currents. The perfect diamagnetism is maintained by the surface currents on edges of both the material and its vortices.

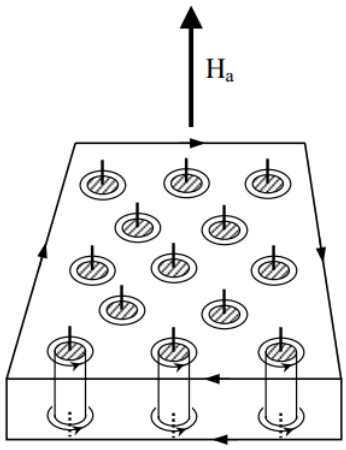

Figure 1.6 – The mixed state with fluxon lattices and encircling supercurrent [9]

Because of microstructural defects and impurities (lattice defects, grain boundaries, dislocations), the vortices movement will be stopped. This energy barrier created lead to the flux pinning. The Lorentz force F_l created on each vortex is smaller than the pinning force F_p.

However, the Lorentz force can become greater than the pinning force at a certain critical value J_c leading to the vortices movement called flux flow.

In the case of thermally-actived vortices motion called flux creep, the movement of vortices is slower and more sporadic. The superconducting state of the material has not disappeared.

Metal alloys and some pure metals, Niobium for instance, are type-II superconductors. Different oxide compounds are also included. All pure metals and metal alloys have their T_c below 30 K and are referred to as low temperature superconductors (LTS), while the oxide superconductors have their T_c above 30 K and are referred to as high-temperature superconductors (HTS).

1.3 HTS: macroscopic models

HTS materials are type-II in nature, and the magnetic flux entering a type-II superconductor does so in the form of vortices. Super-currents flow around vortices to shield them from the superconducting matrix. These vortices always appeared in

the sample initially from the edges of the material. Their motion inward is impeded by pinning sites due to irregularities in the material microstructure, such as lattice defects, grain boundaries, and dislocations [10].

Because of these pinning sites, type-II superconductor are characterized by an irreversible magnetization and a trapped magnetic field.

1.3.1 Critical state model : Bean model

A critical state model (CSM) is often used to represent the dynamics and different operation modes of vortices.

Critical state models are based on the macroscopic behaviour of superconducting materials, derived from experimental observations of the relationship between current density and magnetic field. The critical state occurs when an applied field exceeds a type-II superconductor's lower critical magnetic field H_{c1}. Magnetic flux vortices with circulating shielding currents penetrate the material to shield the interior of the material from the applied current/field.

Where there is a current flowing in the superconductor, the magnetic field experiences a Lorentz force $\mathbf{F_l} = \mathbf{J} \times \mathbf{B}$. For a large Lorentz force, the vortices become de-pinned and move in the direction of the force with a velocity $\mathbf{v}_v$. this vortex movement will induce an electric field $\mathbf{E} = \mathbf{B} \times \mathbf{v}_v$. Thus,

$$\mathbf{E} = \rho(\|\mathbf{J}\|)\mathbf{J} \tag{1.1}$$

In order to maintain a superconduting state, all CSMs state that the current density should not exceed the critical current density J_c.

The Bean model is the simplest of all CSMs. It states that the magnitude of the superconductor's current density takes values of either 0 where the perfect diamagnetism property holds or $\pm J_c$ in the mixed state. When the superconductor is entirely penetrated with $\pm J_c$, the superconductor is characterized by a critical state.

1.3.2 E-J power law

Some HTS materials are characterized by an ill-defined critical current density. Anderson[33] proposed a flux creep theory where the relationship between the electric field and the current density is not discontinuous. In this theory, vortices move

slowly, due to thermal activation, at current lower than the critical current, then an electric field appears and losses occur. Rhyner [11] proposed the following $E-J$ power law :

$$E = E_c \left\| \frac{\mathbf{J}}{J_c} \right\|^n \tag{1.2}$$

with $J_c = J_c(B,T)$, $n = n(B,T)$ and the critical electric field $E_c = 10^{-4}$ V/m. The power law index n is dependent on the HTS properties and microstructure.

The extreme case of $n = 1$ and $n = \infty$ correspond to the linear Ohm law and the Bean's model.

1.3.3 Kim model

It is the commonly used model characterizing the magnetic field dependence of the critical current density. Kim and Anderson [12] showed that the critical current density in a type-II superconductor exhibit a strong dependence on temperature, as well as magnetic field. It was also recognized by Bean [14]. The model developed states that the critical current density decreases with the local magnetic field according to :

$$J_c(B,T) = J_{c0}(T) \left(1 + \frac{\|B\|}{B_0}\right)^{-1} \tag{1.3}$$

with B_0 a constant and J_{c0} is the critical current density at zero field, which is a temperature-dependent constant of the material.

1.3.4 AC losses

HTS materials appear to be much more interesting for technological development since they can carry large currents. However, losses are generated due to the vortices dynamic (flux flow or flux creep) resulting from the varying current or magnetic field applied. It is therefore important to accurately calculate and measure AC losses in order to minimize them, since they are dissipated as heat, for an efficient design of both superconducting and cryogenic systems [15].

Depending of the energy source, AC losses are usually classified as magnetization losses or transport current losses [16]. Both categories can be present in superconducting applications.

AC losses types

They are losses generated by the HTS materials subjected to an external alternating magnetic field.

- Hysteresis losses

  They are the result of the magnetization irreversibility caused by the pinning of vortices. The flux that first entered the superconductor does not leave in the same manner. It is because of vortice pinned by irregularities in the HTS material that such irreversibility and hysteresis losses occur. The hysteresis loop is shown on the average magnetic field density **B**-magnetic field **H** characteristic. The dissipated energy per cycle is proportional to the loop surface if no transport current are flowing [16]. The larger the critical current density is, the larger the hysteresis losses will be [10].

- Coupling losses

  Coupling losses are present in multi-filamentary conductors which consists of multiple superconducting filaments (round filaments or tapes) within a resistive matrix [16], [17]. The induced current generated by the alternating magnetic field can flow through the superconductor and the resistive matrix between the filaments. Filaments are said to couple together once the current flow from one filament to another. In this configuration, all the filaments form one magnetic body with a resistance encountered in the resistive matrix. Thus, losses generated in the resistive matrix are called the coupling loss [16].

- Eddy current losses

  When an external time-varying magnetic field penetrates into a normal conductor, it induces a changing electric field, which in turn causes currents to flow [18]. These are known as eddy currents. They are generated by the resistive matrix which protects the superconducting filaments.

AC losses calculation

AC losses will be calculated using an electric method. An electric field is induced by an applied time-varying magnetic field. A screening current begins to flow and there is a local non-zero product of voltage and current. The product $\mathbf{E} \cdot \mathbf{J}$ is integrated spatially over the conductor cross-section area S and with respect to time over

the magnetic field cycle yields to give the loss (per unit volume per field cycle in J/cycle/m^3).

$$\mathbf{Q} = \frac{1}{S}\int_0^{1/f}\int_S \mathbf{E}\cdot\mathbf{J}dSdt \tag{1.4}$$

1.4 HTS applications

HTS applications encompasses domains where high current density or high magnetic fields are important. It includes for example transformers, fault current limiter, superconducting magnetic storage, magnetic resonance imaging, power cables and motors or generators.

Transformers

HTS allow transformers to operate continuously in overload conditions without any lifetime loss because of the ultra-cold operating range of 20 to 77 K and the low total losses due to their zero resistance. They are also smaller and lighter in comparaison to conventional transformers [19].

Fault current limiter

The negligible impedance of HTS in their superconducting state allows them to operate in ideal conditions whenever fault currents are not generated. Moreover, the current is limited, whenever there is a fault event, because the transition from the superconducting state to the normal state is too fast [20].

Superconducting magnetic storage

Those devices are used to prevent voltage sags and outage on the energy distribution network. They are generally small, store and release quickly huge amount of energy. They are either flywheel-based or magnetic field-based [21].

Magnetic resonance imaging

HTS will render small the huge magnet used in the magnetic resonance imaging (MRI). Their accessibility to higher temperatures and their low manufacturing and maintenance will make them more accessible for such market [22].

Power cables

HTS allow power cables to carry huge amount of current while the total generated losses are extremely lower in comparison with normal conductors present in cables. Their lightness gives more design flexibility to apply on these cables [23]-[24].

HTS rotating machines : motors or generators

However, this dissertation work will be focused on HTS rotating machines such as motor or generator. HTS coil windings of those machines will be modeled precisely in order to optimize both their design and the machines design.

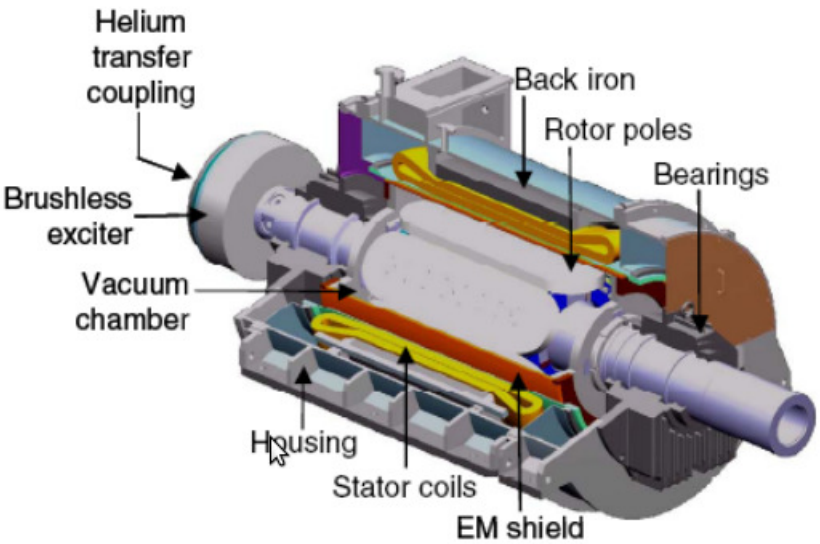

Figure 1.7 – HTS rotating machine [38].

A look at HTS synchronous motor shows that HTS rotating machines include both stator and rotor assembly. Each assembly have HTS coil windings containing multiple polesets, each fabricated using HTS wire or tape designed to withstand the powerful magnetic and mechanical forces experienced in the rotor.

Those HTS wires or tapes design consider the minimization of the resulting AC losses during the machine operation. They mainly include fine filaments twisted or straight embedded together inside a resistive matrix (mostly metallic) as a mechanical support.

Table 1.1 – HTS Synchronous motors developed

Contribution	Rated power	Time	Basic parameters	HTS material
America	1.5 kW [25]	1993	2-pole, 3600 rpm	Multifilamentary BSCCO coil
	3.7 kW [25]	1993	4-pole, 1800 rpm	Multifilamentary BSCCO coil
	92 kW [26]	1995	4-pole, 1800 rpm	Multifilamentary Bi-2223/Ag coil
	735 kW [27]	2000	4-pole, 1800 rpm	Multifilamentary BSCCO tape
	3.7 MW [28]	2001	4-pole, 1800 rpm	Multifilamentary BSCCO wire
	5 MW [29]	2003	6-pole, 230 rpm	Multifilamentary BSCCO tape
	36.5 MW [38]	2006	120 rpm	Multifilamentary BSCCO tape
Siemens	400 kW [31]	2001	4-pole, 1800 rpm	Mg-reinforced Bi-2223/Ag tape
	4 MW [32]	2005	2-pole, 3600 rpm	Bi-2223 tape
Korea	73.5 kW [33]	2002	4-pole, 1800 rpm	Stainless steel-reinforced Bi-2223 tape
	3 kW [34]	2001	4-pole, 1800 rpm	Bi-2223/Ag tape
Japan	3.1 kW [35]	2005	8-pole, 720 rpm	Gd-Ba-Cu-O bulk magnet
Finland	1.5 kW [40]	1997	4-pole, 1500 rpm	Bi-2223/Ag coil

1.5 Mathematical models

The goal here is to derive mathematical representations of the overall physical behaviour of the studied system based on relevant hypothesis and simplifying assumptions. In the case of superconducting devices, the electromagnetic behaviour is simultaneously characterized by Maxwell equations (eqs.1.5-1.8), the linear magnetic constitutive law (eq. 1.10) and the electric power law (eq. 1.12).

All electromagnetic phenomena are described mathematically by Maxwell equations. They are first-order vectorial partial differential equations which relates various physical quantities characterizing the electric or magnetic behaviour of a continuum domain. Those quantities, both time and space dependent, are the following :

- the magnetic field $\mathbf{H}$ measured in Ampere per meter (A/m)
- the magnetic field density $\mathbf{B}$ measured in Tesla (T)
- the electric field $\mathbf{E}$ in Volts per meter (V/m)
- the electric field density $\mathbf{D}$ in Coulomb per meter square (C/m^2)
- the electric current density $\mathbf{J}$ in Amperes per meter square (A/m^2)
- the electric charge density ρ in Coulomb per meter cube (C/m^3)

$$\nabla \times \mathbf{E} = -\frac{\partial \mathbf{B}}{\partial t} \tag{1.5}$$

$$\frac{\partial \mathbf{D}}{\partial t} + \mathbf{J} = \nabla \times \mathbf{H} \tag{1.6}$$

$$\nabla \cdot \mathbf{D} = \rho \tag{1.7}$$

$$\nabla \cdot \mathbf{B} = 0 \tag{1.8}$$

Superconducting machines will not generally operate in high frequencies, therefore the electric field density $\mathbf{D}$ can be neglected. Thus, equations 1.6 will become :

$$\mathbf{J} = \nabla \times \mathbf{H} \tag{1.9}$$

We therefore have equations 1.5, 1.7, 1.8 and 1.9 to use for our study. However, they are not enough to find a solution since there is more unknowns (18) than equations (8).

Additional equations must be added to 1.5, 1.7, 1.8 and 1.9 in order to find a solution. They are known as constitutive laws and are expressed as :

$$\mathbf{B} = \mu_0 \mathbf{H} \tag{1.10}$$

$$\mathbf{D} = \epsilon_0 \mathbf{E} \tag{1.11}$$

$$\mathbf{E} = \rho(\mathbf{J})\mathbf{J} \tag{1.12}$$

with the non-linear resistivity ρ characterized by the power law 1.2 in the superconducting domain. The quantity μ_0, whose value is about $4\pi.10^{-7}$ H/m (Henry per meter), is known as the magnetic permeability. The quantity ϵ_0 is known as the vacuum permittivity.

All those mathematical relations are embedded in one single sytem of equations generally called formulation. The formulations [41] - [42] used to model superconducting devices are listed below.

1.5.1 H formulation

The magnetic field $\mathbf{H}$ is the only unknown of this formulation. The elementary equations deriving from both Maxwell equations and the constitutive laws are :

$$\mathbf{J} = \nabla \times \mathbf{H} \tag{1.13}$$

$$\mathbf{E} = \rho(\mathbf{J})\mathbf{J} = \rho\mathbf{J} \tag{1.14}$$

The combination of all those elementary equations with the Faraday law in equation 1.5 will give us the $\mathbf{H}$ formulation :

$$\nabla \times (\rho\nabla \times \mathbf{H}) = -\mu\frac{\partial \mathbf{H}}{\partial t} \tag{1.15}$$

1.5.2 E formulation

The electric field $\mathbf{E}$ is the only unknown of this formulation. The elementary equations deriving from both Maxwell equations and the constitutive laws are :

$$\frac{\partial \mathbf{B}}{\partial t} = -\nabla \times \mathbf{E} \tag{1.16}$$

$$\mathbf{J} = \rho(\mathbf{J})^{-1}\mathbf{E} = \rho^{-1}\mathbf{E} \tag{1.17}$$

The combination of all those elementary equations with both the Ampere law in equation 1.9 and the linear magnetic constitutive law in equation 1.10 will give us the $\mathbf{E}$ formulation :

$$\nabla \times \nabla \times \mathbf{E} = -\frac{\partial(\mu\rho^{-1}\mathbf{E})}{\partial t} \tag{1.18}$$

1.5.3 $\mathbf{A} - V$ formulation

In this case, the system of equations have the magnetic vector potential $\mathbf{A}$ and the electric scalar potential V as unknowns. Based on Maxwell equations and constitutive laws characterizing the behaviour of superconducting devices, we have the following elementary equations :

$$\mathbf{B} = \nabla \times \mathbf{A} \tag{1.19}$$

$$\mathbf{E} = -\frac{\partial \mathbf{A}}{\partial t} - \nabla V \tag{1.20}$$

$$\sigma = \sigma(\mathbf{E}) \tag{1.21}$$

where $\mathbf{B}$, $\mathbf{E}$, σ are the magnetic field density vector, the electric field vector and the electric conductivity.

The combination of all those elementary equations with the Ampere law in equation 1.9 and the linear magnetic constitutive law in equation 1.10 will give us the system of equations known as the $\mathbf{A} - V$ formulation :

$$\begin{cases} \nabla \times \frac{1}{\mu} \nabla \times \mathbf{A} = -\sigma(\frac{\partial \mathbf{A}}{\partial t} + \nabla V) \\ \nabla \cdot (\sigma(\frac{\partial \mathbf{A}}{\partial t} + \nabla V)) = 0 \end{cases} \tag{1.22}$$

with μ the magnetic permeability.

1.5.4 $\mathbf{T} - \phi$ formulation

The unknowns of such formulation are the electric vector potential $\mathbf{T}$ and the magnetic scalar potential ϕ. The elementary equations deriving from both Maxwell equations and the constitutive laws are :

$$\mathbf{J} = \nabla \times \mathbf{T} \tag{1.23}$$

$$\mathbf{H} = \mathbf{T} - \nabla \phi \tag{1.24}$$

$$\rho = \rho(\mathbf{J}) \tag{1.25}$$

where $\mathbf{J}$, $\mathbf{H}$, ρ are the current density vector, the magnetic field vector and the electric resistivity.

The combination of all those elementary equations with the Faraday law in equation 1.5 will give us the $\mathbf{T} - \phi$ formulation :

$$\begin{cases} \nabla \times \rho \nabla \times \mathbf{T} = -\mu \frac{\partial (\mathbf{T} - \nabla \phi)}{\partial t} \\ \nabla \cdot (\mathbf{T} - \nabla \phi) = 0 \end{cases} \tag{1.26}$$

1.6 Numerical methods

Every formulations described above can be solved using different numerical methods. Several numerical methods used to model superconducting devices have been found in the literature. Through some discretization, they approximate the exact solution of the model described by whichever formulation listed. The discretization involves the geometry of the problem, either as a grid or as a mesh, depending on the method. The dimension of this grid/mesh, specifically the number of nodes or edges in it, is directly related to the number of degrees of freedoms (or unknowns) of the problem. The number of degrees of freedoms has a critical impact on the computation time and memory requirements.

1.6.1 Minimization of an energy functional

One can define a third family of numerical method based on the minimization of an energy functional. This approach is very intuitive, since it consists in defining a functional that relates the total energy of a system (or a variation of energy with respect to some initial conditions) with the variables that define the state of this system, e.g. potentials, field variables, source terms, etc.

It allows more freedom in the way one chooses the shape functions used to approximate the solution. It also allows solving classes of problems that would be difficult to solve otherwise, namely the critical state problem, which is singular in its pure form, and therefore can only be approximated to some extent when using a classical electromagnetic formulation. Although at first sight this approach requires less mathematical formalism than strictly applying the finite element method, the process of minimizing a functional in order to obtain a well-posed discrete equation system requires good skills in functional analysis and optimization algorithms. Also, since it is generally based on integral equations, its use in 3D is likely to be limited to relatively small problems.

In the HTS community, the use of this method was first introduced by Bossavit [55] and applied by Maslouh [44]. It was also formalized later by Prigozhin [43] as a systematic approach to solve the J distribution in HTS domains based on the critical state model. A variant of the method was later introduced by Sanchez and Navau [45] and improved and generalized by Pardo *et al* [46] to include, among other things, current constraints.

▷ **Limitations**

A similar problem of matrices size is encountered with methods using the minimization of the energy functional. Despite their flexible mathematics formalism, these optimization problems cannot be easily extended to complex 3D geometries because of the resulting algebraic system sizes.

1.6.2 Integral methods

These methods require the use of Green's functions defined everywhere in the studied domain. They were mainly developed for 2D modelling purposes. The Green's functions will be solved exactly on each point of the grid or mesh. All the local solutions will be interpolated over the grid or mesh in order to get the global solution over the studied domain. These methods are smoother by nature but we can have Green's functions with singularities leading to large errors if not treated properly. The pointwise discretization of the problem leads to a global matricial system with full matrices over the studied domain. Thus, the larger the studied domain is, the bigger the full matrices will be and the more difficult it will be to solve the resulting matricial system. Moreover, these methods do not give control on the error approximation over the studied domain. It will therefore be difficult to refine the global solution depending on the approximated error of the problem over the studied domain.

In the applied superconductivity modelling, the Brandt method remain the commonly used integral method for 2D problems [48]. It solves the Laplace equation resulting from the $\mathbf{A} - V$ formulation. As mentioned above, a general solution of the magnetic vector potential $\mathbf{A}$ is derived, based on Green's functions, in order to discretize, over each grid's point, the resulting integral formulation of the problem. From there, the matricial system must be inverted and solved iteratively. Boundary conditions are not needed. The numerical algorithm has been implemented and used by several groups to model efficiently different superconducting systems. However, its extension on 3D problems is not simple. Green's functions in 3D are not easily defined and the resulting matricial system will be large, because of the high number of degrees of freedom characterizing 3D problems, in addition to be full.

▷ **Limitations**

Despite the smoothness of the 2D solution and its simple implementation, integral methods such as the Brandt method cannot easily be extended to 3D problems. In fact, Green's functions evaluation is not simple even for simple geometries in 3D. Even if the Green's functions are well-defined, the large size and complexity of the geometry will likely lead to compute an inversion of full large matrix. Such an operation is extremely costly in terms of computations. It is thus not suitable to compute with those methods the electro-magnetic behaviour of twisted multi-filamentary superconducting tapes or wires for instance.

1.6.3 Finite element method

This method consists in solving, through a discretization over a meshed domain, the weighted residual of the formulation describing the problem. The weighted residual is the integration over the meshed domain of the formulation multiplied by weighting or test functions. The weight functions are used to approximate in a piecewise manner the continuous solution of a studied problem over discrete mesh.

The modified governing equations are said to be written in weak form. Through this approach, it is possible to weight the numerical error of the problem over the whole domain. Thus, obtained numerical solutions can minimize the error on the whole domain depending on the chosen weight functions.

The local solution on each element of the meshed domain is determined by the values set at the element boundary. Information is thus propagated from element to element through their common boundaries leading to the boundary conditions imposed at the periphery of the studied model which will then determine the global solution. Therefore, the connectivity between the degrees of freedom is only function of the nodes (in case of nodal base functions) or edges (in case of vector base functions) shared by neighbouring elements, leading to sparse matrix patterns, and a more or less linear relationship between the number of degrees of freedom and the memory requirements.

Finite element method is the most popular numerical method used in engineering to model systems. Through commercial or open-source software packages, it provides a stable and simple to use framework to model in 1D, 2D and 3D geometries of complex shapes [51]-[55].

In applied superconductivity, finite element method have been investigated for 2D and 3D models. It has been implemented mostly on the $\mathbf{A} - V$, $\mathbf{T} - \phi$, and

H formulations. For numerical stability purposes, a residual resistivity is always added on the non-linear resistivity $\rho(\mathbf{J})$. This added term might be viewed as a thermally activated resistance at the initial temperature.

In 3D, the resulting matricial system, though sparse, becomes large due to the high number of degrees of freedom. Large enough memory is therefore required in 3D cases.

▷ **Limitations**

Finite element methods are geared to model in any dimension complex geometries of superconducting systems. However, the resulting sparse matrix size will scale with the size of the geometry because of the degrees of freedom growing number. The large matrix size will require large memories and it can limit computations of problems involving large scale systems. In addition to the non-linearities present in the problem, difficulties to invert and solve such matrix will occur. The treatment of non-linearities present in the power law will become problematic for high value of the index n and high-order approximations.

Thus, a linearization of the power law will be investigated in this thesis work because it will provide more stability.

1.6.4 Finite volume method

This method is using aspects of both the finite difference method and finite element method, especially on partial differential equations that arise from physical conservation laws.

It can be applied to both structured and unstructured meshed domains of complex geometries. Based on well-defined control volumes deriving from the meshed domain, a volume integral conservation law of the problem is discretized. These control volumes are either vertex-centered or cell-centered with mesh nodes as vertices and mesh elements as cell. In order to obtain a linear system, integral on each control volume are expressed in terms of mean values.

A numerical integration procedure, with a specified polynomial approximation, is thus applied in a point-wise manner over the volume integral formulation on each control volume. Equations also involve integrals of fluxes, approximated in a linear form as numerical fluxes, crossing the boundary of control volumes defined

on the mesh. Furthermore, boundary conditions can be applied non-invasively since values of the conserved variables are located within the control volumes and not at vertices or surfaces.

Finite volume method requires few degrees of freedom to compute a solution closed to the exact one. The resulting matrix is banded, thus sparse, when structured meshes apply while it has no line structure in the case of unstructured meshes.

The major advantage of this method is that it implicitly makes the flux variable divergence-free by equating the flux integrals on every common edge (in 2D) or face (in 3D) of mesh elements.

Alloui *et al* [56]-[58] investigated this numerical approach for the modeling of high-temperature superconductors in 3D. The $\mathbf{A}-V$ formulation coupled with the heat equation was used. Different numerical schemes and iterative solvers were also used in order to deal with the resulting matricial system associated to the discretized problem. They successfully obtained expected results for numerous cases basedon the finite volume element.

▷ **Limitations**

Although the smoothness and the regularity of the solutions is not a concern, finite volume method present the same limitations as the finite element method in terms of large matrix for 3D problem. Solving these kind of matrices is costly.

1.6.5 Finite element - Finite volume hybrid method

It is usually implemented to solve convection-diffusion partial differential equations where the diffusion equations are discretized using the finite element method and the convection equations are discretized using the finite volume method. Moreover, equivalence of the computed projection of the finite element method solution on the finite volume method mesh and vice versa allows mathematically a successful numerical implementation of this hybrid approach.

Specific operators must be implemented in order to successfully compute the equivalent projection of the solution. These operators ensure the coupling between the finite element discrete form and the finite volume discrete form.

It can be applied to both structured and unstructured meshed domains of complex geometries. Based on nodes and elements, as control volumes, of the meshed

domain, a volume integral formulation of the problem is discretized. According to this approach, the global solution is assumed to be piecewise constant.

Kameni *et al* [59]-[60] implemented this approach for the specific case of modeling, based on the **E**-formulation, high-temperature superconductors in 2D. In the partial differential equations associated to the **E**-formulation, the nodal finite element method appears to be not suitable for the treatment of non-linear terms while the finite volume method does not approximate well the diffusion terms because of the gradient operator. Thus, the finite volume method will be implemented in the discrete form based on the nodal finite element method to deal efficiently with the non-linear terms. The nodal finite element method will be used for the discrete form of the finite volume method in order to approximate effectively the diffusion terms. For the coupling of both methods in order to solve the **E**-formulation, well-defined operators will be derived in order to successfully compute the equivalent projected solution in either finite element or finite volume meshed domain.

The developed method is robust and efficient. Unlike the finite element method, it allows the modeling of superconductors with an n-value as high as 200.

▷ **Limitations**

The mixed approach combining both finite element method and finite volume method, to solve non-linear equations system describing superconductors, is tedious to extend in 3D. Despite its robustness and efficiency, specific operators must be well-defined for 3D geometries of any complexity.

1.6.6 Discontinuous Galerkin method

This method [61] is using aspects of both the Finite volume method and Finite elements method. On each element of the studied mesh, a finite element approach is implemented to discretize the problem. Moreover, interface terms, defined on each element face, are replaced by equivalent integrals of well-defined numerical fluxes. Numerical fluxes are evaluated, using the symmetry interior penalty method, in order to ensure the convergence of the problem.

The discrete system consists of block diagonal matrices with each blocks made of volume terms and interface terms.

Because of the structure of its matricial system, this method allows naturally a scalability in both memory and computations through parallel processing. Moreover, the discontinuous character of the local approximated problem allows a flex-

ible treatment of the non-linearities.

▷ **Limitations**

The discontinuous galerkin method investigated by Kameni *et al* [62]-[64] for the E-formulation provides numerically the adequate framework to deal with the commonly encountered large matrice size mentioned in all the numerical approaches above. Its framework is naturally prone to parallel computations which neglect the limited memory problem occurring with the finite element method. Despite its robustness and efficiency, solving the **E**-formulation is not appropriate for complex geometries in 3D. It requires the analytical evaluation of demagnetization coefficients of the studied domain in order to compute the electro-magnetic behaviour without a surrounding air domain. Such an evaluation is too complicated for geometries which includes twisted multi-filamentary superconductors for instance.

In the following thesis work, this approach implementation to solve the **H**-formulation will be investigated.

1.7 Conclusion

Through a thorough literature investigation, we found extensive works done on the modelling of high-temperature superconductors. Several differential formulations of the problem have been explored and solved with numerous numerical approaches for 2D and/or 3D modelling.

The numerical approaches encompass strong form and weak form approaches. The former includes integral methods such as the Brandt method and the latter consists of variational based method .

They are commonly limited by the resulting large matrices needed to be inverted and computed. These operations are extremely costly in computations time and memory. Moreover, the treatments of the non-linearities might also be problematic causing difficulties to get the problem convergence.

In regards of those observations, the work of this thesis will consist in adding more numerical features to the commonly used finite element method applied on the **H**-formulation in order to make the 3D modelling of twisted multi-filamentary superconducting wires possible. While some of those features, described in chapter 2, are related for convergence purposes to the treatment of the non-linearities arising

from the electrical behaviour of superconductors, most of them, described in chapter 3, will be geared towards more simplifications of the associated 3D problem of those wires.

Also, in chapter 2 we will be improving upon the discontinuous galerkin method framework, applied on the **E**-formulation, in order to efficiently model in 3D, based on the **H**-formulation, high-temperature superconductors of any geometric complexities. This numerical approach has been chosen because of its potential for electromagnetism 3D modelling. It also provides natural implementation of parallel computations, which might reduce the memory usage and potentially allows computations over large scale systems. Thus, it has the potential to provide scalability in terms of memory and computations. Computations speed can also be improved upon implementing GPU-accelerated computations.

Chapter 2

3D modelling of high-temperature superconductors

2.1 Introduction

High temperature superconductors (HTS) are used as windings in several alternating applications, such as motors design for aircraft propulsion [30] and magnets design for medical imaging [65]. They must carry high currents efficiently. High and complex magnetic fields will thus be generated based on the superconducting windings geometry used in the studied systems.

AC losses, generated by superconducting windings as heat loads, must be evaluated accurately and reduced in order to design an efficient superconducting machine. Such an evaluation must take in account the highly non-linear electrical behaviour characterizing high temperature superconductors, thermal conditions, complexities arising from both the winding geometry and the external magnetic field configurations.

Robust, efficient and fast numerical approaches must be developed to model accurately in 3D the thermo-electromagnetic behaviour of high-temperature superconducting windings. They are represented by the global domain Ω. It will generally include two non-overlapping sub-domains Ω_s and Ω_r which are respectively superconducting and a non-superconducting sub-domain. For instance, superconducting windings made of multi-filamentary superconducting wire will have all its filaments as the sub-domain Ω_s while the sub-domain Ω_r will represent the resistive matrix embedding the filaments.

In this chapter, the studied problem we must solve will be formulated based on the magnetic field $\mathbf{H}$ and the temperature T, using the heat equation, Maxwell

equations and the necessary constitutive laws, in section 2.2. Its approximations using the classical finite element method and the nodal discontinuous galerkin method will be investigated in sections 2.3 and 2.4 respectively. The latter numerical approach provides numerous potential advantages such as a scalability over numerous processors through parallel computing. Finally, section 2.5 will focus on comparisons and validations of both numerical approaches applied to simulation cases of superconducting systems in both the non-thermal coupling and thermal coupling cases.

2.2 Problem formulation

2.2.1 Constitutive laws

Magnetic and electric constitutive laws will characterize the studied domain Ω.

The electric behaviour of Ω is assumed linear and isotropic in the sub-domain Ω_r while highly non-linear and isotropic in the sub-domain Ω_s. The linear and isotropic electric constitutive law, known as Ohm law, is expressed as follows:

$$\mathbf{E} = \rho \mathbf{J} \tag{2.1}$$

with ρ the constant resistivity of the non-superconducting sub-domain Ω_r.

The highly non-linear and isotropic electric constitutive law, known as power law, describing the superconducting sub-domain Ω_s. Instead of the expressions shown in equations 1.2 and 1.12, we will have a temperature dependence as follows :

$$\mathbf{E} = \rho(J, T)\mathbf{J} \tag{2.2}$$

with

$$\rho(J, T) = \frac{E_c}{J_c(T)} \left\| \frac{\mathbf{J}}{J_c(T)} \right\|^{n(T)-1} \tag{2.3}$$

In the power law expressed above, the quantity ρ is the electrical resistivity of the sub-domain Ω_s. The quantities E_c, J_c and n are the critical electric field, the critical current density and the power law index of the superconducting domain Ω_s respectively. Both the critical current density and the power law index are

dependent on the temperature T.

2.2.2 Differential formulation

The coupling of the resulting Maxwell equations 1.5, 1.7, 1.8, 1.9 with the heat equations and constitutive equations 1.10, 3.14, 2.2, 2.3 presented above will give the following non-linear vectorial equation based on both the magnetic field $\mathbf{H}$ and the temperature T:

$$\begin{aligned} \mathbf{H} \ &: \ \mu_0 \frac{\partial \mathbf{H}}{\partial t} + \nabla \times (\rho(J,T) \nabla \times \mathbf{H}) = \mathbf{0}, \quad \text{in } \Omega \times [0,t] \\ T \ &: \ \rho_T c_p(T) \frac{\partial T}{\partial t} - \nabla \cdot (\lambda(T) \nabla T) = \rho(J,T) \mathbf{J}^2, \quad \text{in } \Omega \times [0,t] \end{aligned} \tag{2.4}$$

$$\begin{aligned} \mathbf{H} \ &: \ \mathbf{H} \times \mathbf{n} = \mathbf{H_a} \times \mathbf{n}, \quad \text{in } \partial\Omega \\ T \ &: \ \nabla T \cdot \mathbf{n} = \mathbf{0} \quad \text{in } \partial\Omega \end{aligned} \tag{2.5}$$

$$\begin{aligned} \mathbf{H} \ &: \ \mathbf{H}(x,0) = \mathbf{H_0}, \quad \forall x \in \Omega \\ T \ &: \ T(x,0) = T_0, \quad \forall x \in \Omega \end{aligned} \tag{2.6}$$

with the initial temperature T_0 and the initial magnetic field $\mathbf{H_0}$. The boundary $\partial\Omega$ of the studied domain are assumed belonging to an air domain surrounding the entire superconducting windings. Both an external alternating magnetic field $\mathbf{H_a}$ and a thermal insulation condition imposed on the boundaries $\partial\Omega$ are also assumed.

In the heat equation, ρ_T, $c_p(T)$, $\lambda(T)$ are the mass density, the specific heat and the thermal conductivity of the studied domain respectively. AC losses generated by the studied system are considered as a heat source quantity. In fact, the continuity of the tangential components of the magnetic field $\mathbf{H}$ and the conservation of the current density $\mathbf{J} = \nabla \times \mathbf{H}$ must be insured.

In this formulation, the boundary condition of the magnetic part, expressed by equation 2.5 on $\partial\Omega = \Gamma^{D,M}$, are of Dirichlet type for the magnetic part and Neumann for the thermal part. However, some problems might require both Dirichlet and Neumann boundary conditions for each part.

In the magnetic part, Neumann boundary conditions might be imposed on $\Omega^{N,M}$

with $\partial\Omega = \Gamma^{D,M} \cup \Omega^{N,M}$.

For the thermal part of the problem, boundary conditions might be Neumann-like insulation, convection and radiation conditions and Dirichlet too. Assuming $\partial\Omega = \Gamma^{D,T} \cup \Omega^{N,T}$, they can be imposed on $\Omega^{N,T} = \Omega_i^{N,T} \cup \Omega_c^{N,T} \cup \Omega_r^{N,T}$ with $\Omega_i^{N,T} \cap \Omega_c^{N,T} \cap \Omega_r^{N,T} = \emptyset$ for the Neumann boundaries and $\Omega^{D,T}$ for the Dirichlet ones. Depending on the problem, boundaries $\Omega_i^{N,T}$, $\Omega_c^{N,T}$ and $\Omega_r^{N,T}$ are respectively subjected to insulation, convection and radiation conditions.

2.2.3 Variational formulation

The discretization of equation (2.4) requires to derive a variational formulation. The unknown magnetic field $\mathbf{H}$ and the unknown temperature T are supposed to belong to $(\mathbf{L}^2(\Omega))^3$ and $\mathbf{L}^2(\Omega)$ respectively such that :

$$\mathbf{L}^2(\Omega) = \left\{ f : \Omega \subset \mathbb{R}^3 \mapsto \mathbb{R} : \int_\Omega f^2(\mathbf{x}) d\Omega < \infty \right\} \tag{2.7}$$

with a scalar product and a norm expressed as :

$$(f, g)_{\mathbf{L}^2(\Omega)} = \int_\Omega f(\mathbf{x}).g(\mathbf{x}) d\Omega, \ \ \|f\|_{\mathbf{L}^2(\Omega)} = \sqrt{(f, g)_{\mathbf{L}^2(\Omega)}} \tag{2.8}$$

After multiplying equations (2.4) by the basis vector function $\boldsymbol{\varphi}$ and the basis function Φ, we must find the unknown variables couple $(\mathbf{H}, T) \in (\mathbf{L}^2(\Omega))^3 \times \mathbf{L}^2(\Omega)$ such that:

$$\begin{aligned} \mathbf{H} \ : \ & \int_\Omega (\mu_0 \frac{\partial \mathbf{H}}{\partial t} + \nabla \times (\rho(J,T) \nabla \times \mathbf{H})) \cdot \boldsymbol{\varphi} d\Omega = \mathbf{0} \ , \ \ \forall \boldsymbol{\varphi} \in (\mathbf{L}^2(\Omega))^3 \\ T \ : \ & \int_\Omega (\rho_T c_p(T) \frac{\partial T}{\partial t} - \nabla \cdot (\lambda(T) \nabla T) - \rho(J,T) \mathbf{J}^2) \Phi d\Omega = 0 \ , \ \ \forall \Phi \in \mathbf{L}^2(\Omega) \end{aligned} \tag{2.9}$$

However, the Green's theorem applied on the magnetic problem's volumic term and the thermal problem's volumic term with respectively the Curl − Curl operator

and Div − Grad operator will give us

$$\begin{aligned}
\mathbf{H} \ : \quad & \int_\Omega \nabla \times (\rho \nabla \times \mathbf{H}) \cdot \boldsymbol{\varphi} d\Omega = \int_\Omega \rho (\nabla \times \mathbf{H}) \cdot (\nabla \times \boldsymbol{\varphi}) d\Omega - \int_\Gamma ((\rho \nabla \times \mathbf{H}) \times \mathbf{n}) \cdot \boldsymbol{\varphi} dA \\
T \ : \quad & \int_\Omega \nabla \cdot (\lambda(T) \nabla T) \Phi d\Omega = - \int_\Omega \lambda(T) \nabla T \cdot \nabla \Phi d\Omega + \int_\Gamma \lambda(T) (\nabla T \cdot \mathbf{n}) \Phi dA
\end{aligned} \tag{2.10}$$

According to equations 2.9 and 2.10, the final expressions of the variational formulation are :

$$\begin{aligned}
\mathbf{H} \ : \quad & \int_\Omega \mu_0 \frac{\partial \mathbf{H}}{\partial t} \cdot \boldsymbol{\varphi} d\Omega + \int_\Omega \rho (\nabla \times \mathbf{H}) \cdot (\nabla \times \boldsymbol{\varphi}) d\Omega \\
& - \int_\Gamma ((\rho \nabla \times \mathbf{H}) \times \mathbf{n}) \cdot \boldsymbol{\varphi} dA = \mathbf{0} \\
& , \ \forall \boldsymbol{\varphi} \in (\mathbf{L}^2(\Omega))^3 \\
T \ : \quad & \int_\Omega \rho_T c_p(T) \frac{\partial T}{\partial t} \cdot \Phi d\Omega + \int_\Omega \lambda(T) \nabla T \cdot \nabla \Phi d\Omega \\
& - \int_\Omega \rho(J, T) \mathbf{J}^2 \Phi d\Omega \\
& + \int_\Gamma \lambda(T) (\nabla T \cdot \mathbf{n}) \Phi dA = 0 \\
& , \ \forall \Phi \in \mathbf{L}^2(\Omega)
\end{aligned} \tag{2.11}$$

The general solution space of the unknown magnetic field $\mathbf{H}$, defined above, will be restricted based on both the chosen numerical approach and the physics.

Two numerical approaches respectively based on the finite element method and the Discontinuous Galerkin Method will be investigated. Their implementation will be discussed in addition with the treatment of the non-linearities arising from the superconductor electric behaviour.

2.3 Finite element method

A numerical approach based on the classical finite element method has been developed to solve the **H**-formulation. It was implemented in the open source finite element software GetDP [67]-[68]. The treatment of non-linearities, arising from the power law describing the electrical behaviour of superconductors, will also be

investigated.

We will first discuss the spatial discretization of Ω and the associated functional element spaces in order to derive the discrete variational formulation resulting from the **H**-formulation.

2.3.1 Mesh definition

Let us consider a three-dimensional conforming mesh $\mathcal{T}_h$ which is a partition of the domain Ω in tetrahedral or hexahedral elements K such that $\Omega = \bigcup_{K\in\mathcal{T}_h} K$. The size of each element is denoted by h_K. We assume that the mesh is aligned with the discontinuities of the material properties, such as the resistivity ρ, present in the domain. Therefore, $\mathcal{T}_h = \mathcal{T}_{h,s} \cup \mathcal{T}_{h,r}$ with $\mathcal{T}_{h,s}$ and $\mathcal{T}_{h,r}$ respectively representing the meshes of the sub-domains Ω_s and Ω_r.

All the faces of the mesh $\mathcal{T}_h$ belong to the set $\Gamma_h = \Gamma_h^{\mathcal{I}} \cup \Gamma_h^{\mathcal{B}}$ where $\Gamma_h^{\mathcal{I}}$ is the set of all the interior faces and $\Gamma_h^{\mathcal{B}}$ the set of the boundary faces.

Among the boundary faces, there will be faces with either Dirichlet or Neumann boundary conditions such that $\Gamma_h^{\mathcal{B}} = \Gamma_{h,M}^{\mathcal{B},\mathcal{D}} \cup \Gamma_{h,M}^{\mathcal{B},\mathcal{N}}$ and $\Gamma_h^{\mathcal{B}} = \Gamma_{h,T}^{\mathcal{B},\mathcal{D}} \cup \Gamma_{h,T}^{\mathcal{B},\mathcal{N}}$ for both the magnetic and thermal problems respectively . $\Gamma_{h,T}^{\mathcal{B},\mathcal{D}}$ or $\Gamma_{h,M}^{\mathcal{B},\mathcal{D}}$ is the set of boundary faces with Dirichlet conditions and $\Gamma_h^{\mathcal{B},\mathcal{N}}$ is the one with Neumann conditions for either the thermal and the magnetic problems.

2.3.2 Discrete variational formulation

The finite element discretization of the equation (2.4) will need an approximation of the unknown magnetic field **H** based on Nedelec elements. The approximated quantities u^h and $\mathbf{v}^h$ of the temperature T and the magnetic field **H** will be defined over the mesh $\mathcal{T}_h$. They will belong respectively to the following finite element spaces :

$$U^h = \left\{ u \in \mathbf{L}^2(\Omega) : u|_K \in \mathbb{P}^1(K), K \in \mathcal{T}_h \right\} \tag{2.12}$$

and

$$\mathbf{V}^h = \left\{ \mathbf{v} \in H(\mathrm{curl};\Omega) : \mathbf{v}|_K \in (\mathbb{P}^1(K))^3, K \in \mathcal{T}_h \right\} \tag{2.13}$$

with

$$H(\mathrm{curl};\Omega) = \left\{\mathbf{v} \in (\mathbf{L}^2(\Omega))^3 : \mathrm{curl}\mathbf{v} \in (\mathbf{L}^2(\Omega))^3\right\} \tag{2.14}$$

The norm associated with $\mathbf{V}^h$ is on the mesh $\mathcal{T}_h$ evaluated as :

$$\|\mathbf{v}\|_{\mathbf{V}^h} = \|\mathbf{v}\|^2_{H(\mathrm{curl};\Omega)} \tag{2.15}$$

Thus, the discrete weak formulation of equation (2.4) will consist in finding $(\mathbf{v}^h, u^h) \in (\mathbf{V}^h \times U^h)$ such that:

$$\begin{aligned}
\mathbf{H} \ : \ & \int_{\mathcal{T}_h} \mathbf{v}_t^h \cdot \boldsymbol{\varphi} d\mathcal{T}_h + \int_{\mathcal{T}_h} \kappa(\nabla \times \mathbf{v}^h) \cdot (\nabla \times \boldsymbol{\varphi}) d\mathcal{T}_h - \\
& \int_{\Gamma_{h,M}^{\mathcal{B},\mathcal{N}}} ((\kappa \nabla \times \mathbf{v}^h) \times \mathbf{n}) \cdot \boldsymbol{\varphi} dA + I_{h,M}^{\mathcal{B},\mathcal{D}} = \mathbf{0} \ , \quad \forall \boldsymbol{\varphi} \in \mathbf{V}^h \\
T \ : \ & \int_{\mathcal{T}_h} \rho_T c_p u_t^h \cdot \Phi d\mathcal{T}_h - \int_{\mathcal{T}_h} \lambda \nabla T \cdot \nabla \Phi d\mathcal{T}_h - \int_{\mathcal{T}_h} (\rho \mathbf{J}^2) \Phi d\Omega \\
& + \int_{\Gamma_{h,T}^{\mathcal{B},\mathcal{N}}} \lambda (\nabla T \cdot \mathbf{n}) \Phi dA = 0 \ , \quad \forall \Phi \in U^h
\end{aligned} \tag{2.16}$$

with $\mathbf{v}_t^h = \partial \mathbf{v}^h / \partial t$, $u_t^h = \partial u^h / \partial t$, $\kappa = \rho / \mu_0$ and :

$$I_{h,M}^{\mathcal{B},\mathcal{D}} = \int_{\Gamma_{h,M}^{\mathcal{B},\mathcal{D}}} \boldsymbol{\gamma} \cdot \boldsymbol{\varphi} dA + \int_{\Gamma_{h,M}^{\mathcal{B},\mathcal{D}}} (\mathbf{v}^h - \mathbf{H_a}) \cdot \boldsymbol{\gamma}' dA. \tag{2.17}$$

The Lagrange coefficients $\boldsymbol{\gamma}$ and $\boldsymbol{\gamma}'$ help impose the Dirichlet boundary conditions in a weak way. They must belong to the finite element space $\mathbf{V}^h$.

2.3.3 Numerical treatment of the non-linearities arising from $\mathbf{E} = \rho(\mathbf{J})\mathbf{J}$

The electrical behaviour of the superconducting domain Ω_s is defined by a non-linear power law as shown in (2.2) and (2.3).Therefore, the discrete variational formulation, expressed in (3.14), must take in account those non-linearities.

First, a linearization of the vectorial power law is necessary in order to avoid using a residual resistivity and to ensure the convergence of the problem. Therefore, we have the following indicial notation of the combination of (3.14) and (2.3) in the superconducting domain Ω_s :

$$E_i = \frac{E_c}{J_c^{\,n}} \left(J_m J_m\right)^{(n-1)/2} J_i \quad , i, m = 1, 2, 3 \tag{2.18}$$

$\mathbf{E} = E_i$ is differentiable function with respect to the vector field $\mathbf{J} = J_i$. Thus, the first-order Taylor expansion of the vector field E_i around $\mathbf{J_0} = (J_{1,0}, J_{2,0}, J_{3,0})$ can be derived as follows :

$$\mathbf{E}(\mathbf{J}) = \mathbf{E}(\mathbf{J_0}) + \mathbb{J} \cdot (\mathbf{J} - \mathbf{J_0}) \tag{2.19}$$

with $\mathbb{J}$ the Jacobian of the function $\mathbf{E} : \mathbb{R}^3 \mapsto \mathbb{R}^3$ expressed as :

$$\mathbb{J} = \left(\frac{\partial E_i}{\partial J_j}\right)\bigg|_{\Omega_s} = \begin{bmatrix} \partial E_1/\partial J_1 & \partial E_1/\partial J_2 & \partial E_1/\partial J_3 \\ \partial E_2/\partial J_1 & \partial E_2/\partial J_2 & \partial E_2/\partial J_3 \\ \partial E_2/\partial J_1 & \partial E_2/\partial J_2 & \partial E_2/\partial J_3 \end{bmatrix} , \; i, j = 1, 2, 3 \tag{2.20}$$

In order to find the expanded expression of the jacobian $\mathbb{J}$, the partial derivation of E_i with respect to J_j will give the following :

$$\left(\frac{\partial E_i}{\partial J_j}\right)\bigg|_{\Omega_s} = \frac{E_c}{J_c^{\,n}} \left[\frac{\partial J_i}{\partial J_j}(J_m J_m)^{(n-1)/2} + \frac{\partial[(J_m J_m)^{(n-1)/2}]}{\partial J_j} J_i\right] \quad , i, j, m = 1, 2, 3 \tag{2.21}$$

with

$$\frac{\partial J_i}{\partial J_j} = \delta_{ij} \quad , i, j = 1, 2, 3 \tag{2.22}$$

and

$$\begin{aligned} \frac{\partial[(J_m J_m)^{(n-1)/2}]}{\partial J_j} &= (n-1)\left[\frac{\partial J_m}{\partial J_j} J_m\right](J_m J_m)^{(n-3)/2} \\ &= (n-1)\delta_{mj} J_m (J_m J_m)^{(n-3)/2} \\ &\qquad , i, j, m = 1, 2, 3 \end{aligned} \tag{2.23}$$

The use of equations 2.22 and 2.23 in 2.21 will give the following :

$$\begin{aligned} \left(\frac{\partial E_i}{\partial J_j}\right)\bigg|_{\Omega_s} &= \frac{E_c}{{J_c}^n}\left[\delta_{ij}(J_m J_m)^{(n-1)/2} + (n-1)\delta_{mj} J_m (J_m J_m)^{(n-3)/2} J_i\right] \\ &= \frac{E_c}{{J_c}^n}\left[\delta_{ij}(J_m J_m)^{(n-1)/2} + (n-1) J_i J_j (J_m J_m)^{(n-3)/2}\right] \\ &\qquad , i, j, m = 1, 2, 3 \end{aligned} \tag{2.24}$$

Thus

$$\begin{aligned} \left(\frac{\partial E_i}{\partial J_j}\right)\bigg|_{\Omega_s} &= \frac{E_c}{{J_c}^n}\left[\delta_{ij}\|\mathbf{J}\|^{(n-1)} + (n-1) J_i J_j \|\mathbf{J}\|^{(n-3)/2}\right] \\ &\qquad , i, j = 1, 2, 3 \end{aligned} \tag{2.25}$$

In the non-superconducting sub-domain Ω_r, the quantity $\partial E_i/\partial J_j|_{\Omega_r} = \delta_{ij}$. In both sub-domains Ω_s and Ω_r, we will have two real constant numbers ν and M such that :

$$|\mathbb{J}| \leq \nu \leq M \quad , i, j = 1, 2, 3 \tag{2.26}$$

We can conclude from both 2.26 and 2.19 that the vector function $\mathbf{E}(\mathbf{J})$ know as a power law is Lipschitz continuous. The use of the Newton-Raphson algorithm

on the power law linearization will lead to a convergence.

At each time step t_p^l of the problem resolution, the power law will be approximated by a first order Taylor expansion. The linearised power law at the iteration k of the Newton Raphson algorithm is the following:

$$\mathbf{E}(\mathbf{J}_k) = \mathbf{E}(\mathbf{J}_{k-1}) + \overline{\overline{\mathbf{A}}} \cdot (\mathbf{J}_k - \mathbf{J}_{k-1}) \tag{2.27}$$

with

$$\overline{\overline{\mathbf{A}}} = \begin{cases} \mathbb{J}, \text{ in } \Omega_s \\ \rho_r \mathbb{I}, \text{ in } \Omega_r \end{cases} = \begin{cases} \dfrac{(n-1)E_c}{J_c^n} J_i^2 \left\|\mathbf{J}\right\|^{n-3} + \dfrac{E_c}{J_c^n} \left\|\mathbf{J}\right\|^{n-1}, & i = j \text{ in } \Omega_s \\ \dfrac{(n-1)E_c}{J_c^n} J_i J_j \left\|\mathbf{J}\right\|^{n-3} & , i \neq j \text{ in } \Omega_s \\ \rho_r & , i = j \text{ in } \Omega_r \\ 0 & , i \neq j \text{ in } \Omega_r \end{cases} \tag{2.28}$$

where $\mathbb{I}$ the identity matrix, $i, j = 1, 2$ and 3. Moroever, the current density $\mathbf{J}_{k-1}$ and the corresponding electric field, evaluated at the iteration k-1 of the Newton-Raphson algorithm, are known. The power law linearisation will be formulated directly in the discrete variational formulation as an approximation of the following volumic term of the superconducting domain :

$$\int_{\mathcal{T}_{h,s}} \kappa \mathrm{curl} \mathbf{v}_k^h \cdot \mathrm{curl} \boldsymbol{\varphi} d\mathcal{T}_{h,s} \tag{2.29}$$

The approximated expression of (2.29), based on the power law linearisation, will give :

$$\int_{\mathcal{T}_{h,s}} \kappa_{k-1} \mathrm{curl} \mathbf{v}_{k-1}^h \cdot \mathrm{curl} \boldsymbol{\varphi} d\mathcal{T}_{h,s} + \mu_0^{-1} \int_{\mathcal{T}_{h,s}} \overline{\overline{\mathbf{A}}} \cdot (\mathrm{curl} \mathbf{v}_k^h - \mathrm{curl} \mathbf{v}_{k-1}^h) \cdot \mathrm{curl} \boldsymbol{\varphi} d\mathcal{T}_{h,s} \tag{2.30}$$

In the numerical implementation, we noticed that the tensor $\overline{\overline{\mathbf{A}}}$ ensures a stable convergence of the problem.

2.4 Discontinuous Galerkin method

This method consists in solving the studied problem on each element K_i of the mesh $\mathcal{T}_h$. The variational formulation expressed in equation 2.11 will be used on each element K_i instead of the global domain Ω. Moreover, interfaces terms expressed on ∂K_i instead of Γ will be replaced in an equivalent way by numerical fluxes term based defined in a finite volume method-like way. Those interfaces terms will help connect all the elements K_i of the mesh under the same problem [71]-[72].

2.4.1 Mesh definition

A three-dimensional conforming mesh $\mathcal{T}_h$ is a partition of the domain Ω in tetrahedral or hexahedral elements K_i of size h_{K_i} such that :

$$\Omega = \bigcup_{i=1}^{N_e} K_i \tag{2.31}$$

$$\overset{o}{K}_l \cap \overset{o}{K}_m = \emptyset, \quad \forall l, m \text{ with } 1 < l \neq m < N_e \tag{2.32}$$

with $\overset{o}{K}_l$ representing the interior domain or the largest open set of the element K_l.

The set $\mathcal{F}_h$ of all faces of the mesh $\mathcal{T}_h$ consists of a subset of interior faces $\mathcal{F}_h^i$ and a subset $\mathcal{F}_h^b$ of boundary faces such that :

$$\mathcal{F}_h^i \cap \mathcal{F}_h^b = \emptyset \tag{2.33}$$

While the boundary faces of $\mathcal{F}_h^b$ will help impose boundary conditions, the interior faces of $\mathcal{F}_h^i$ will help connect all the elements K_i through numerical fluxes. Both subsets are defined as :

$$\forall f \in \mathcal{F}_h^i, \quad \exists l, m \text{ such that } 1 < l \neq m < N_e, \quad f = K_l \cap K_m \tag{2.34}$$

and

$$\forall f \in \mathcal{F}_h^b, \quad \exists l \text{ such that } 1 < l < N_e, \quad f = K_l \cap \partial\Omega \tag{2.35}$$

We assume that the mesh is aligned with the discontinuities of the material properties, such as the resistivity ρ, present in the domain. Therefore, $\mathcal{T}_h = \mathcal{T}_{h,s} \cup \mathcal{T}_{h,r}$ with $\mathcal{T}_{h,s}$ and $\mathcal{T}_{h,r}$ respectively representing the meshes of the sub-domains Ω_s and Ω_r.

Among the boundary faces, there will be ones with either Dirichlet or Neunmann boundary conditions depending on the problem types:

$$\mathcal{F}_h^b = \mathcal{F}_{h,T}^{b,D} \cup \mathcal{F}_{h,T}^{b,N} \tag{2.36}$$

and

$$\mathcal{F}_h^b = \mathcal{F}_{h,M}^{b,D} \cup \mathcal{F}_{h,M}^{b,N} \tag{2.37}$$

with $\mathcal{F}_{h,T}^{b,D}$ or $\mathcal{F}_{h,M}^{b,D}$ and $\mathcal{F}_h^{b,N}$ or $\mathcal{F}_{h,T}^{b,N}$ are subsets of boundary faces with Dirichlet conditions and Neumann conditions respectively for either the thermal or magnetic parts of the problem.

2.4.2 Discrete Variational formulation

The discontinuous galerkin discretization of the equation (2.4) will need nodal approximation v^h and $\mathbf{w}^h$ of the unknown temperature T and magnetic field $\mathbf{H}$. These approximated quantities are defined over each finite element K_i of the mesh $\mathcal{T}_h$. They will respectively belong to the following finite element space :

$$U^h = \left\{ u \in \mathbf{L}^2(\Omega) : u|_K \in \mathbb{P}^m(K), K \in \mathcal{T}_h \right\} \tag{2.38}$$

and

$$\mathbf{W}^h = \left\{ \mathbf{v} \in (\mathbf{L}^2(\Omega))^3 : \mathbf{v}|_K \in (\mathbb{P}^m(K))^3, K \in \mathcal{T}_h \right\} \tag{2.39}$$

with $\mathbb{P}^m(K)$ the space of polynomials of degree at most m on an element K.The solution space $\mathbf{W}^h$ is a subset of square-integrable vector function space $(\mathbf{L}^2(\Omega))^3$. Its associated norm with is the sum of $(\mathbf{L}^2(K_i))^3$ norm evaluated on each element

K_i such that :

$$\|\mathbf{v}\|_{\mathbf{W}^h} = \left(\sum_{i=1}^{N_e} \|\mathbf{v}|_{K_i}\|^2_{\mathbf{W}^h} \right)^{\frac{1}{2}} \tag{2.40}$$

The discrete weak formulation of equation (2.4) associated with the discontinuous Galerkin method, defined on each element K, consists in finding $(\mathbf{w}^h, u^h) \in \mathbf{W}^h \times U^h$ such that:

$$\begin{aligned}
\mathbf{H} \ : \ & \int_{K_i} \frac{\partial \mathbf{w}^h}{\partial t} \cdot \boldsymbol{\varphi} dK_i + \int_{K_i} \kappa(\nabla \times \mathbf{w}^h) \cdot (\nabla \times \boldsymbol{\varphi}) dK_i \\
& - \int_{\partial K_i} ((\kappa \nabla \times \mathbf{w}^h) \times \mathbf{n}) \cdot \boldsymbol{\varphi} dA = \mathbf{0} \ , \quad \forall \boldsymbol{\varphi} \in \mathbf{W}^h \\
T \ : \ & \int_{K_i} \rho_T c_p \frac{\partial u^h}{\partial t} \cdot \Phi dK_i - \int_{K_i} \lambda \nabla u^h \cdot \nabla \Phi dK_i \\
& - \int_{K_i} (\rho \mathbf{J}^2) \Phi dK_i \\
& + \int_{\partial K_i} \lambda (\nabla T \cdot \mathbf{n}) \Phi dA = 0 \ , \quad \forall \Phi \in U^h
\end{aligned} \tag{2.41}$$

However, the equation based on the magnetic field $\mathbf{H}$ as an unknown in 2.41 must be expressed in a conservative form for the numerical implementation. Therefore, the $\mathbf{curl} - \mathbf{curl}$ operator is changed by a div operator such that :

$$\kappa \mathrm{curl} \mathbf{w}^h = (F^h_x, F^h_y, F^h_z)^T \tag{2.42}$$

and

$$\mathbf{F}_1 = (0, F^h_z, -F^h_y)^T, \mathbf{F}_2 = (-F^h_z, 0, F^h_x)^T, \mathbf{F}_3 = (F^h_y, -F^h_x, 0)^T \tag{2.43}$$

will give the following derivations

$$\begin{cases} \text{curl}(\kappa \text{curl}\mathbf{w}^h) = (\text{div}\mathbf{F}_1, \text{div}\mathbf{F}_2, \text{div}\mathbf{F}_3)^T \\ \\ (\kappa \text{curl}\mathbf{w}^h) \times \mathbf{n} = (\mathbf{F}_1 \cdot \mathbf{n}, \mathbf{F}_2 \cdot \mathbf{n}, \mathbf{F}_3 \cdot \mathbf{n})^T \end{cases} \tag{2.44}$$

With $\mathbf{w}^h = (w_1, w_2, w_3)^T$, $\boldsymbol{\varphi} = (\varphi_1, \varphi_2, \varphi_3)^T$ and $\mathbb{F} = (\mathbf{F}_1, \mathbf{F}_2, \mathbf{F}_3)^T$, the final expression of the set of equations in 2.41 in the conservative form (with $j = 1, 2$ and 3) is :

$$\begin{aligned} \mathbf{H} \ : \ & \int_{K_i} \frac{\partial w_j}{\partial t} \cdot \varphi_j dK_i + \int_{K_i} \mathbf{F}_j \cdot \nabla \boldsymbol{\varphi} dK_i \\ & - \int_{\partial K_i} (\mathbf{F}_j \cdot \mathbf{n}) \varphi_j dA = \mathbf{0} \ , \quad \forall \boldsymbol{\varphi} \in \mathbf{W}^h \\ T \ : \ & \int_{K_i} \rho_T c_p \frac{\partial u^h}{\partial t} \cdot \Phi dK_i - \int_{K_i} \lambda \nabla u^h \cdot \nabla \Phi dK_i \\ & - \int_{K_i} (\rho \mathbf{J}^2) \Phi dK_i \\ & + \int_{\partial K_i} \lambda (\nabla u^h \cdot \mathbf{n}) \Phi dA = 0 \ , \quad \forall \Phi \in U^h \end{aligned} \tag{2.45}$$

with $\kappa = \rho/\mu_0$ and $\mathbf{n}$ the interface normal vector present in interface terms :

$$I_{h,M} = - \int_{\partial K_i} \big((\kappa \nabla \times \mathbf{w}^h) \times \mathbf{n} \big) \cdot \boldsymbol{\varphi} dA = \int_{\partial K_i} (\mathbf{F}_j \cdot \mathbf{n}) \varphi_j dA \tag{2.46}$$

$$I_{h,T} = \int_{\partial K_i} \lambda (\nabla T \cdot \mathbf{n}) \Phi dA \tag{2.47}$$

They are expressed respectively in the magnetic and thermal part of the problem equations 2.41 and 2.45 above.

However, the continuity of the tangential components of the approximated magnetic field $\mathbf{w}^h$, as expressed by the constraint equation 1.8, must be ensured. Thus, an equivalent and penalized interface term $\tilde{I}_{h,M}$ must replace the actual interface term $I_{h,M}$ in order to both ensure the constraint equation 1.8 and the convergence. A similar approach will help us derive for the thermal part of the problem a penal-

ized interface term $\tilde{I}_{h,T}$ in place of the interface term $I_{h,T}$ to ensure the continuity of the temperature.

2.4.3 Spatial approximation

Each element K_i of the mesh $\mathcal{T}_h$ is characterized by vertices a_k with $k \in 1, .., N$. Moreover, Lagrange polynomials $L_k \in \mathbb{P}^m(K)$ will be set on each K_i such that:

$$L_k(a_l) = \delta_{kl} \tag{2.48}$$

with δ_{kl} the Kroneker delta function. Because of the discontinuous characteristic of the method, those functions are assumed to be zero outside their defined domain K_i. They are also constructed as basis functions on reference elements resulting from a mapping Ψ based on the meshed elements K_i.

The mapping Ψ is a diffeomorphism that transform a physical element D into a topological elements I as shown in the figure 2.1 below.

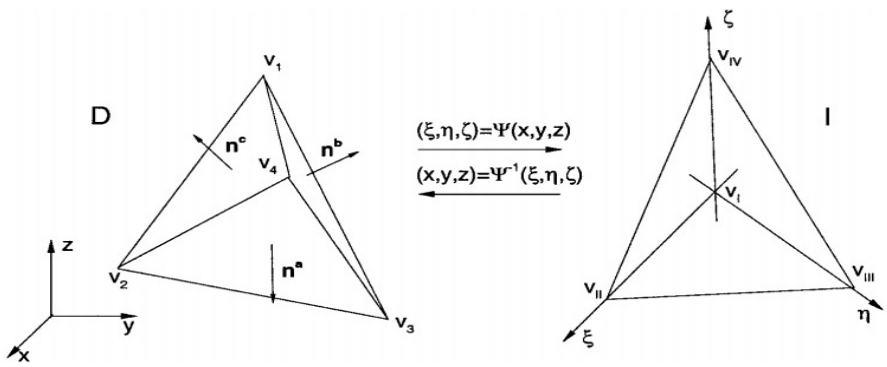

Figure 2.1 – Mapping from D to I

Let $\mathbf{v}_1, \mathbf{v}_2, \mathbf{v}_3, \mathbf{v}_4$ the vertices of the physical element D while their images through the mapping Ψ are $\mathbf{v}_I, \mathbf{v}_{II}, \mathbf{v}_{III}, \mathbf{v}_{IV}$ in the element I. In both elements, faces are defined as a, b, c and d.

In the tetrahedra case, the diffeomorphism Ψ, mapping a point $\mathbf{x} = (x, y, z)$ of the element D and its associated image $\xi = (\xi, \eta, \zeta)$, is expressed as :

$$\mathbf{x} = \Psi^{-1}(\xi) = \lambda_1 \mathbf{v}_1 + \lambda_2 \mathbf{v}_2 + \lambda_3 \mathbf{v}_3 + \lambda_4 \mathbf{v}_4 \tag{2.49}$$

and

$$\xi = \Psi(\mathbf{x}) = \lambda_1 \mathbf{v}_I + \lambda_2 \mathbf{v}_{II} + \lambda_3 \mathbf{v}_{III} + \lambda_4 \mathbf{v}_{IV} \tag{2.50}$$

where $\lambda_1, \lambda_2, \lambda_3, \lambda_4$, known as the barycentric coordinates, are invariant with $\sum_{s=1}^{4} \lambda_s = 1$. Moreover we have :

$$\mathbf{v}_I = \begin{pmatrix} -1 \\ -1 \\ -1 \end{pmatrix}, \mathbf{v}_{II} = \begin{pmatrix} 1 \\ -1 \\ -1 \end{pmatrix}, \mathbf{v}_{III} = \begin{pmatrix} -1 \\ 1 \\ -1 \end{pmatrix}, \mathbf{v}_{IV} = \begin{pmatrix} -1 \\ -1 \\ 1 \end{pmatrix} \tag{2.51}$$

The previous vortices coordinates ultimately lead to the linear formulation of the barycentric coordinates expressed as follows :

$$\lambda_1 = -(\xi + \eta + \zeta + 1)/2, \lambda_2 = (\xi + 1)/2, \lambda_3 = -(\zeta + 1)/2, \lambda_4 = (\eta + 1)/2 \tag{2.52}$$

In order to work in the parametric space, we will use the following property :

$$\frac{\partial \mathbf{x}}{\partial \xi} \frac{\partial \xi}{\partial \mathbf{x}} = \begin{pmatrix} x_\xi & x_\eta & x_\zeta \\ y_\xi & y_\eta & y_\zeta \\ z_\xi & z_\eta & z_\zeta \end{pmatrix} \cdot \begin{pmatrix} \xi_x & \xi_y & \xi_z \\ \eta_x & \eta_y & \eta_z \\ \zeta_x & \zeta_y & \zeta_z \end{pmatrix} = \begin{pmatrix} 1 & 0 & 0 \\ 0 & 1 & 0 \\ 0 & 0 & 1 \end{pmatrix} \tag{2.53}$$

The Jacobian J_Ψ of the diffeomorphism Ψ will be constant since the barycentric coordinates are linear. It will be formulated as :

$$J_\Psi = \left| \frac{\partial \mathbf{x}}{\partial \xi} \right| = \frac{1}{\nabla \xi \cdot (\nabla \eta \times \nabla \zeta)} \tag{2.54}$$

According to such mapping, elementary integration and derivation operations are implemented as follows :

- The gradient of a function $\mathbf{F} = (F_x, F_y, F_z)$ is, based on the mapping Ψ, expressed as:

$$\nabla \mathbf{F} = \frac{1}{J_\Psi} \Big[\frac{\partial}{\partial \xi}(J_\Psi \mathbf{F} \cdot \nabla \xi) + \frac{\partial}{\partial \eta}(J_\Psi \mathbf{F} \cdot \nabla \eta) + \frac{\partial}{\partial \zeta}(J_\Psi \mathbf{F} \cdot \nabla \zeta) \Big] \tag{2.55}$$

- The scalar product on element D to the element I is given by :

$$\int_D f(\mathbf{x}) g(\mathbf{x}) d\mathbf{x} = \int_I f(\mathbf{x}(\xi)) g(\mathbf{x}(\xi)) J_\Psi(\xi) d\xi \tag{2.56}$$

- The scalar product on the element's faces of D to the element's faces of I is

given by :

$$\int_{\partial D} f(\mathbf{x})g(\mathbf{x})d\mathbf{x} = \int_{\partial I} f(\mathbf{x}(\xi))g(\mathbf{x}(\xi))J_{\Psi}(\xi)d\xi \tag{2.57}$$

Moreover, the interpolation of a function f using basis functions L_k and the mapping Ψ give us the following :

$$f(\xi) = \sum_{k=0}^{N} f_k L_k(\xi) \tag{2.58}$$

with ξ_k the interpolation points such that $f_k = f(\xi_k)$ and $L_k(\xi_l) = \delta_{kl}$.

Let ϕ_k the polynomial basis of $\mathbb{P}^m$ and the associated Vandermonde matrix:

$$V([\xi_1, .., \xi_N]) = \begin{pmatrix} \phi_1(\xi_1) & \phi_2(\xi_1) & \dots & \phi_N(\xi_1) \\ \phi_1(\xi_2) & \phi_2(\xi_2) & \dots & \phi_N(\xi_2) \\ \vdots & \vdots & \ddots & \vdots \\ \phi_1(\xi_N) & \phi_2(\xi_N) & \dots & \phi_N(\xi_N) \end{pmatrix} \tag{2.59}$$

thus

$$L_k(\xi) = \frac{|V([\xi_1, ..., \xi_{k-1}, \xi, \xi_{k+1}, ..., \xi_N])|}{V([\xi_1, .., \xi_N])} \tag{2.60}$$

Interpolation points will be choosed based on the quadrature method of Legendre-Gauss-Lobatto in order to render the Vandermonde matrix invertible and minimize the error from the polynomial interpolation.

Thus we will have the following approximations of the magnetic field $\mathbf{H} = H_i$ (where $i = 1, 2,$ and 3) and the temperature T :

$$H_i = \sum_{j=0}^{N} h_j L_j(\mathbf{x}) \tag{2.61}$$

and

$$T = \sum_{j=0}^{N} t_j L_j(\mathbf{x}) \tag{2.62}$$

2.4.4 Numerical fluxes terms on the faces of the mesh $\mathcal{T}_h$

New interfaces terms expressed as numerical fluxes will be constructed to replace the actual interface terms. The derived terms, based on the symmetric interior

penalty method, should be equivalent to $I_{h,M}$ and $I_{h,T}$. The term $I_{h,M}$ must specifically ensure the continuity of the normal and tangential components of the magnetic field $\mathbf{H}$ across each face $f \in \mathcal{T}_h$. The defined face will either belong to two neighbouring elements K (on the left side) and K' (on the right side) as $f = \partial K \cap \partial K'$ or to the boundary Γ as $f = \partial K \cap \Gamma$.

▷ **Thermal problem**

Based on several previous studies on the Discontinuous Galerkin method applied on Poisson problem, the equivalent interface term $\tilde{I}_{h,T}$ for the thermal part of the problem is known as :

$$\tilde{I}_{h,T} = -\int_f [\lambda \nabla \Phi \cdot \mathbf{n}]\{\{u^h\}\} dA - \int_f [\lambda \nabla u^h \cdot \mathbf{n}]\{\{\Phi\}\} dA + I^{p,T} \tag{2.63}$$

with the penalty term $I^{p,T}$ defined as :

$$I^{p,T} = \int_f \mathtt{b}[u^h][\Phi] dA \tag{2.64}$$

The penalty coefficient $\mathtt{b}$ depends on both the size and diffusivities of the neighbouring elements K and $K^{'}$. The quantities $[u^h]$ and $\{\{u^h\}\}$ denote the jump and average of the approximated temperature u^h across each face f. For instance, if $f = \partial K \cap \partial K'$ for two neighbouring elements K and K', the respective jump and average are :

$$[u^h] = u^h_K - u^h_{K'} \tag{2.65}$$

and

$$\{\{u^h\}\} = \frac{u^h_K - u^h_{K'}}{2} \tag{2.66}$$

with u^h_K and $u^h_{K'}$ the approximate temperature fields on elements K and $K^{'}$.

▷ **Magnetic problem**

Grote [70] was able to derive error estimates on the discontinuous galerkin energy norm from the use of the interior penalty discontinuous galerkin method applied to Maxwell equations. He then developped appropriate interface terms with two theorems in order to get the convergence.

Grote theorem 2: a priori error estimate on general finite element meshes

Let the analytical solution $\mathbf{w}$ *of the problem satisfy*

$\mathbf{w} \in L^\infty(J; H^{1+s}(\Omega)^3)$, $\mathbf{w}_t = \partial \mathbf{w}/\partial t \in L^\infty(J; H^{1+s}(\Omega)^3)$,

for $s > \frac{1}{2}$, $\mathbf{w}^h$ *be the semi-discrete Discontinuous Galerkin approximation with a coefficient* $\alpha \geqslant \alpha_{min}$. *Then the error* $\mathbf{e} = \mathbf{w} - \mathbf{w}^h$ *satisfies*

$$\|\mathbf{e}\|_{L^\infty(J;\mathbf{V}(h))} \leqslant C|\mathbf{e}(0)|_h + Ch^{\min(s,l)}\Big(\|\mathbf{w}\|_{L^\infty(J;H^{1+s}(\Omega)^3)} + \|\mathbf{w}_t\|_{L^\infty(J;H^{1+s}(\Omega)^3)}\Big),$$

with a constant $C > 0$ *that is independent of the mesh size.*

In the theorem 2 above, $\mathbf{w}_0 = \mathbf{w}|_{t=0} \in L^\infty(J; H^{1+s}(\Omega)^3)$, thus we have :

$$|\mathbf{e}(0)|_h \leqslant Ch^{\min(s,l)}\|\mathbf{w}_0\|_{1+s,\Omega}$$

There is therefore an optimal convergence of order $\mathcal{O}(h^{\min(s,l)})$ with respect to the discontinuous galerkin energy norm. However, solutions to the Maxwell equations sometimes have singularities that do not satisfy the regularity assumptions of the previous theorem.

The following theorem will show that the discontinuous galerkin method can still converge under weaker yet realistic regularity assumptions provided that the meshes are conforming.

Grote theorem 3: a priori error estimate on low-regularity solutions with singularities

Let the analytical solution $\mathbf{w}$ *of the problem satisfy*

$\mathbf{w}_t$, $\mathrm{curl}\mathbf{w} \in L^\infty(J; H^s(\Omega)^3)$,

for $s > \frac{1}{2}$. *Next, let* $\mathcal{T}_h$ *be a conforming triangulation of* Ω *into tetrahedra or hexahedra with edges parallel to the coordinates axes, and* $\mathbf{w}^h$ *be the semi-*

discrete Discontinuous Galerkin approximation with $\alpha \geqslant \alpha_{min}$. *Then the error* $\mathbf{e} = \mathbf{w} - \mathbf{w}^h$ *satisfies*

$$\|\mathbf{e}\|_{L^\infty(J;\mathbf{V}(h))} \leqslant |\mathbf{e}(0)|_h + Ch^{\min(s,l)}\Big(\|\mathbf{w}\|_{L^\infty(J;H^s(\Omega)^3)}$$
$$+\|\mathrm{curl}\mathbf{w}\|_{L^\infty(J;H^s(\Omega)^3)} + \|\mathbf{w}_t\|_{L^\infty(J;H^s(\Omega)^3)} + \|\mathrm{curl}\mathbf{w}_t\|_{L^\infty(J;H^s(\Omega)^3)}\Big),$$

with a constant $C > 0$ *that is independent of the mesh size.*

Assuming $\mathbf{w}_0 = \mathbf{w}|_{t=0} \in L^\infty(J; H^{1+s}(\Omega)^3)$, theorem 3 give us an optimal convergence of order $\mathcal{O}(h^{\min(s,l)})$ for the error in the energy norm.

Based on this work, we implemented a similar equivalent interface term function of the magnetic field and based on the symmetric interior penalty method to the magnetic part of the **H**-formulation as :

$$-\int_f [\boldsymbol{\varphi} \times \mathbf{n}] \cdot \{\{\kappa \cdot \mathrm{curl}\mathbf{w}^h\}\} dA - \int_f [\mathbf{w}^h \times \mathbf{n}] \cdot \{\{\kappa \cdot \mathrm{curl}\boldsymbol{\varphi}\}\} dA + I^p_{h,M} \quad (2.67)$$

with the penalty term $I^p_{h,M} = \displaystyle\int_f \mathtt{a}[\mathbf{w}^h \times \mathbf{n}] \cdot [\boldsymbol{\varphi} \times \mathbf{n}] dA$.

The quantities $[\mathbf{w}^h \times \mathbf{n}]$ and $\{\{\mathbf{w}^h \times \mathbf{n}\}\}$ denote the jump and average of the tangential components of the field $\mathbf{w}^h$ across each face f. For instance, if $f = \partial K \cap \partial K'$ for two neighbouring elements K and K', the respective jump and average of the tangential components of the magnetic field are :

$$[\mathbf{w}^h \times \mathbf{n}] = \mathbf{w}^h_K \times \mathbf{n} - \mathbf{w}^h_{K'} \times \mathbf{n} \quad (2.68)$$

and

$$\{\{\mathbf{w}^h \times \mathbf{n}\}\} = \frac{\mathbf{w}^h_K \times \mathbf{n} + \mathbf{w}^h_{K'} \times \mathbf{n}}{2} \quad (2.69)$$

In the penalty term $I^p_{h,M}$, the function $\mathtt{a}$ penalizes the jump of the tangential components of the fields $\mathbf{w}^h$ and $\boldsymbol{\varphi}$. According to Grote, it is defined as :

$$\mathtt{a}|_f = \alpha \mathtt{mh} \quad (2.70)$$

with

$$\mathtt{m}|_f = \begin{cases} \max(\kappa_K, \kappa_{K'}), & f = \partial K \cap \partial K' \\ \kappa_K, & f = \partial K \cap \Gamma \end{cases} \tag{2.71}$$

and

$$\mathtt{h}|_f = \begin{cases} \max(h_K, h_{K'}), & f = \partial K \cap \partial K' \\ h_K, & f = \partial K \cap \Gamma \end{cases} \tag{2.72}$$

The coefficient α is a constant whose minimum value must depend on the shape-regularity of the mesh and the approximation order of the field $\mathbf{u}^h$. The larger α becomes, the smaller the time step will be for the solver to reach convergence.

However, the interface term expression defined above is not suitable for conservative form based on the *div* operator. In order to ease this process, the interface term must be rewritten in terms of fluxes projected on the basis vector function $\boldsymbol{\varphi}$.

First, the following mixed product invariance property :

$$\mathbf{a} \cdot (\mathbf{b} \times \mathbf{c}) = \mathbf{b} \cdot (\mathbf{c} \times \mathbf{a}) = \mathbf{c} \cdot (\mathbf{a} \times \mathbf{b}) \tag{2.73}$$

with vectors $\mathbf{a}, \mathbf{b}$, and $\mathbf{c}$, applied in equation (2.67) will lead to the interface term expression below:

$$\int_f [\boldsymbol{\varphi}] \cdot \{\{(\kappa \mathrm{curl} \mathbf{w}^h) \times \mathbf{n}\}\} dA + \int_f [(\kappa \mathrm{curl} \mathbf{w}^h) \times \mathbf{n}] \cdot \{\{\boldsymbol{\varphi}\}\} dA + I^p_{h,M} \tag{2.74}$$

with the penalty term $I^p_{h,M} = -\int_f \mathtt{a}[\boldsymbol{\varphi}] \cdot [\mathbf{n} \times \mathbf{w}^h \times \mathbf{n}] dA$.

While this expression showcases projections on the basis vector function $\boldsymbol{\varphi}$, it does not introduce fluxes quantities. Based on the conservative form expressed in the set of equations in 2.45, we will have the following interface term (with $j = 1, 2$ and 3):

$$\int_f [\varphi_j] \cdot \{\{\mathbf{F}_j \cdot \mathbf{n}\}\} dA + \int_f [\mathbf{F}_j \cdot \mathbf{n}] \cdot \{\{\varphi_j\}\} dA + I^p_{h,M} \tag{2.75}$$

where the penalty term $I^p_{h,M}$ remains unchanged.

2.4.5 Boundary conditions

In order to respect the physics, Neumann and Dirichlet boundary conditions must be imposed in accordance with the numerical fluxes developed above. The associated boundaries in both the magnetic and thermal problems respectively are $\Gamma^{\mathcal{D}}$, $\Gamma^{\mathcal{D},\mathcal{T}}$ for the Dirichlet ones and $\Gamma^{\mathcal{N}}$, $\Gamma^{\mathcal{N},\mathcal{T}}$ for the Neumann ones. They are defined such that $\Gamma^{\mathcal{D}} \cap \Gamma^{\mathcal{N}} = \emptyset$, $\Gamma^{\mathcal{D},\mathcal{T}} \cap \Gamma^{\mathcal{N},\mathcal{T}} = \emptyset$, $\Gamma = \Gamma^{\mathcal{D},\mathcal{T}} \cup \Gamma^{\mathcal{N},\mathcal{T}}$ and $\Gamma = \Gamma^{\mathcal{D}} \cup \Gamma^{\mathcal{N}}$. The interface common to both neighbouring elements K and K' is always assumed to belong to $\Gamma^{\mathcal{D}}$,$\Gamma^{\mathcal{D},\mathcal{T}}$ or $\Gamma^{\mathcal{N}}$,$\Gamma^{\mathcal{N},\mathcal{T}}$ on the side of K.

▷ **Magnetic problem**

In this problem, Dirichlet boundary condition, expressed as $\mathbf{H} = \mathbf{H}_a$ where $\mathbf{H}_a$ is the external magnetic field, will be applied on the boundary $\Gamma^{\mathcal{D}}$. Thus the following jump and average terms present on the interface term $\tilde{I}_{h,M}$:

$$[(\kappa \cdot \mathrm{curl}\mathbf{w}^h) \times \mathbf{n}] = -(\kappa \cdot \mathrm{curl}\mathbf{w}^h_{K'}) \times \mathbf{n} \tag{2.76}$$

$$[\mathbf{n} \times \mathbf{w}^h \times \mathbf{n}] = \mathbf{n} \times \mathbf{H_a} \times \mathbf{n} - \mathbf{n} \times \mathbf{w}^h_{K'} \times \mathbf{n} \tag{2.77}$$

$$\{\{(\kappa \cdot \mathrm{curl}\mathbf{w}^h) \times \mathbf{n}\}\} = \frac{(\kappa \cdot \mathrm{curl}\mathbf{w}^h_{K'}) \times \mathbf{n}}{2} \tag{2.78}$$

The quantities $\mathbf{w}^h_K$ and $\mathbf{w}^h_{K'}$ are the approximation of the magnetic field $\mathbf{H}$ over the neighbouring elements K and K' respectively. Meanwhile, the Neumann boundary condition $\mathbf{H} \times \mathbf{n} = \mathbf{0}$, applied on $\Gamma^{\mathcal{N}}$,will give the following jump and average terms :

$$[(\kappa \cdot \mathrm{curl}\mathbf{w}^h) \times \mathbf{n}] = (\kappa \cdot \mathrm{curl}\mathbf{w}^h_K - \kappa \cdot \mathrm{curl}\mathbf{w}^h_{K'}) \times \mathbf{n} \tag{2.79}$$

$$[\mathbf{n} \times \mathbf{w}^h \times \mathbf{n}] = -\mathbf{n} \times \mathbf{w}^h_{K'} \times \mathbf{n} \tag{2.80}$$

$$\{\{(\kappa \cdot \mathrm{curl}\mathbf{w}^h) \times \mathbf{n}\}\} = \frac{(\kappa \cdot \mathrm{curl}\mathbf{w}^h_K + \kappa \cdot \mathrm{curl}\mathbf{w}^h_{K'}) \times \mathbf{n}}{2} \tag{2.81}$$

▷ **Thermal problem**

In this problem, Dirichlet boundary condition, expressed as $T = T_a$ where T_a is the fixed temperature, imposed on the boundary $\Gamma^{\mathcal{D},\mathcal{T}}$. Thus the following jump and average terms present on the interface term $\tilde{I_{h,T}}$:

$$[\lambda \cdot \text{grad} u^h \cdot \mathbf{n}] = -\lambda \text{grad} u^h_{K'} \cdot \mathbf{n} \tag{2.82}$$

$$[u^h] = T_a - u^h_{K'} \tag{2.83}$$

$$\{\{\lambda \text{grad} u^h \cdot \mathbf{n}\}\} = \frac{\lambda \text{grad} u^h_{K'} \cdot \mathbf{n}}{2} \tag{2.84}$$

The quantities u^h_K and $u^h_{K'}$ are the approximation of the temperature T over the neighbouring elements K and K' respectively. Meanwhile, the Neumann boundary condition $\text{grad} T \cdot \mathbf{n} = \mathbf{0}$, applied on $\Gamma^{\mathcal{N},\mathcal{T}}$, will give the following jump and average terms :

$$[\lambda \text{grad} u^h \cdot \mathbf{n}] = -\lambda \text{grad} u^h_{K'} \cdot \mathbf{n} \tag{2.85}$$

$$[u^h] = u^h_K - u^h_{K'} \tag{2.86}$$

$$\{\{\lambda \text{grad} u^h \cdot \mathbf{n}\}\} = \frac{\lambda \text{grad} u^h_{K'} \cdot \mathbf{n}}{2} \tag{2.87}$$

2.4.6 Numerical treatment of the non-linearities arising from $\mathbf{E} = \rho(\mathbf{J})\mathbf{J}$

The discontinuous galerkin method will allow, with its local approximation of the problem on each element, either an explicit or an implicit treatment of the non-linear resistivity $\rho(\mathbf{J})$ of the problem.

In the explicit case, the resistivity ρ^{l-1} , evaluated at the time step t_p^{l-1} of the problem resolution, is used as an input in the problem at following time step t_p^l.

In the implicit case, the full expression of the resistivity ρ is included in the definition of $\mathbb{F}$ expressed in the conservative form 2.45. A Newton-Raphson algorithm

is applied on the approximation of $\mathbb{F}$ to perform a linearization equivalent to the power law linearization defined for the finite element method.

The convergence, once reached in each approach, will give a good enough approximation of the solution.

2.5 Comparisons and validations

2.5.1 Straight superconducting filament embedded in a Niobium matrix carrying a sinusoidal transport current

The superconducting wire of 4 mm length is made of one single superconducting filament of 50 μm radius embedded in a Niobium matrix of 0.6 mm. The wire is carry a sinusoidal transport current of amplitude $I_m = 500$ A. It is modeled using the non-thermal coupling. The computed AC losses will be compared with the ones obtained with an **H**-formulation finite element model implemented in GetDP only .

No thermal coupling

The superconducting behaviour of the wire is characterized by a critical electric field $E_c = 10^{-7}$ V/mm, a critical current density $J_c = 50$ A/mm^2 and a power law exponent $n = 20$. The transport current frequency will be $f = 100$ Hz.

Computed AC losses, fig.2.2, are equivalent for all the numerical approaches implemented.

The allocated memory was about 2 GB for the new approach and about 6 GB for GetDP.

2.5.2 Superconducting cube subjected to an alternating transverse magnetic field

A superconducting cube of $2mm$ side length, subjected to an external magnetic field $\mathbf{H_a} = H_m sin(2\pi ft)\mathbf{e_y}$, will be modeled using both the non-thermal coupling and thermal coupling formulation with the discontinuous galerkin method [72]. The computed AC losses will be compared with the ones obtained with **H**-formulation finite element models implemented in GetDP and Comsol Multiphysics. Computations in Comsol Multiphysics will be done for both the non-thermal coupling and thermal coupling only.

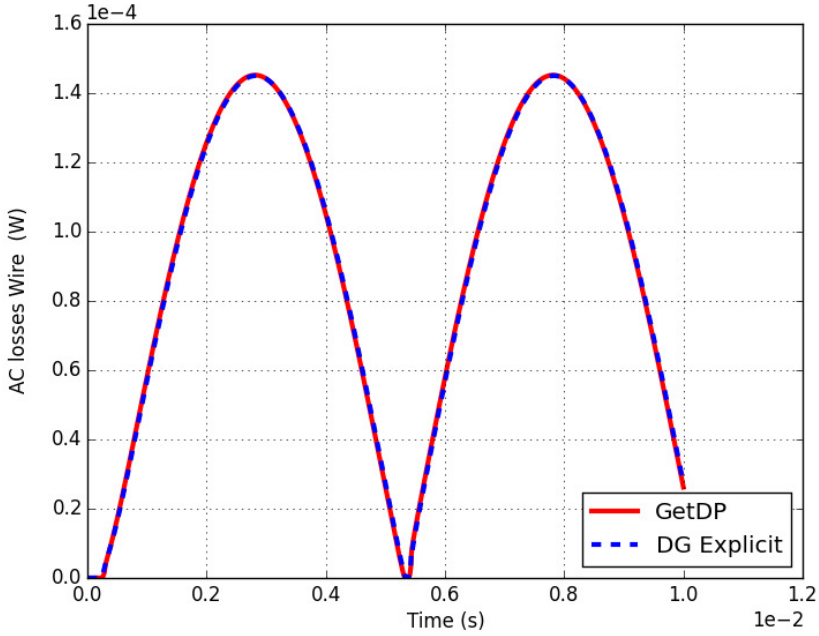

Figure 2.2 – AC losses in the non-thermal case of a superconducting wire carrying a transport current computed with GetDP and the discontinuous galerkin method (DG) with the non-linear resistivity evaluated explicitly.

No thermal coupling

The superconducting behaviour of the cube is characterized by a critical electric field $E_c = 10^{-7}$ V/mm, a critical current density $J_c = 100$ A/mm^2 and a power law exponent $n = 10$. The magnetic applied flux density amplitude is $B_m = 2$ T with a frequency $f = 50$ Hz.

Computed AC losses, fig.2.3, are equivalent for all the numerical approaches implemented.

Using the same meshed cube model, computations in GetDP were performed in 2 hours. The implicit Euler method, used as a time stepping algorithm, was coupled with both iterative and direct methods as matricial sytem solvers. Solvers such as `preonly` and `lu` from the PETSc (Portable, Extensible Toolkit for Scientific Computation) library were used simultaneously with MUMPS (Multifrontal Massively Parallel sparse direct Solver). With an initial timestep of 10^{-5} s subjected to an adaptive time-stepping scheme, the implicit Euler method tolerances were set to 10^{-3} and 10^{-6} for the absolute and relative residuals respectively.

The allocated memory was about 2 GB for the new approach and about 6 GB for GetDP.

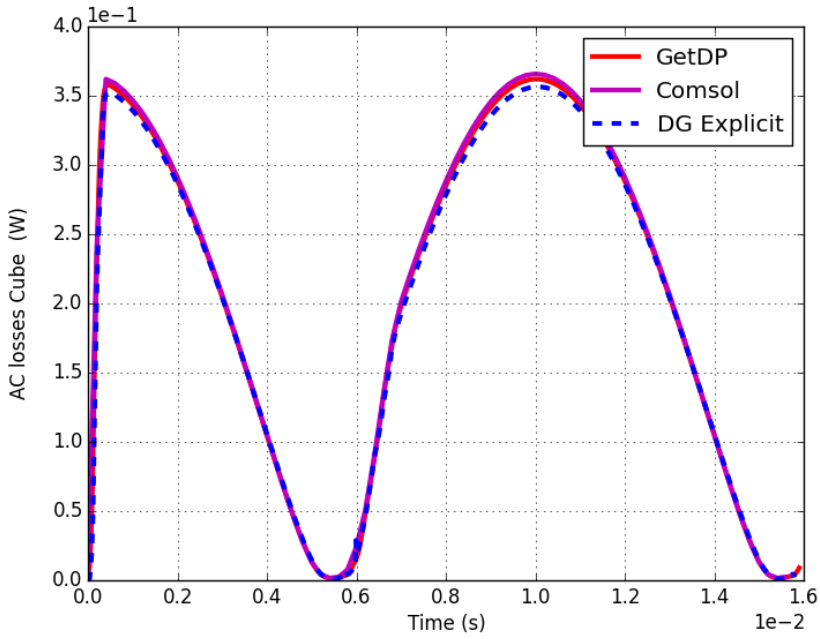

Figure 2.3 – AC losses in the non-thermal case of a superconducting cube subjected to an external magnetic field computed with GetDP, Comsol and the discontinuous galerkin method (DG) with the non-linear resistivity evaluated explicitly.

Thermal coupling

The superconducting cube used in the non-thermal coupling case will be modeled such that there is simultaneously a thermal insulation and an external magnetic field $\mathbf{H_a} = H_m sin(2\pi f t)\mathbf{e_y}$ on the air domain boundaries. Comparisons of the computed AC losses in this thermal case will be done using the numerical approaches investigated in the non-thermal coupling case.

The superconducting behaviour of the cube is characterized by a critical electric field $E_c = 10^{-7}$ V/mm, an initial critical current density $J_{c0} = 100$ A/mm^2, a critical temperature $T_c = 82$ K and a power law exponent $n = 10$. The magnetic applied flux density amplitude is $B_m = 2$ T with a frequency $f = 50$ Hz. The temperature dependence of the critical current density is characterized by :

$$J_c = J_{c0}\frac{T_c - T}{(T_c - T_o)} \tag{2.88}$$

While in the air domain the thermal properties are the specific heat $c_{pa} = 2040$ J/(kg.K), the mass density $\rho_a = 8.08607$ kg/m^3 and the thermal conductivity $\lambda_a = 0.139$ W/(m.K), the superconducting cube is characterized by a specific heat $c_{ps} = 3$ J/(kg.K), the mass density $\rho_s = 6300$ kg/m^3 and the thermal conductivity $\lambda_s = 11$ W/(m.K). The initial temperature T_o is set at 77 K.

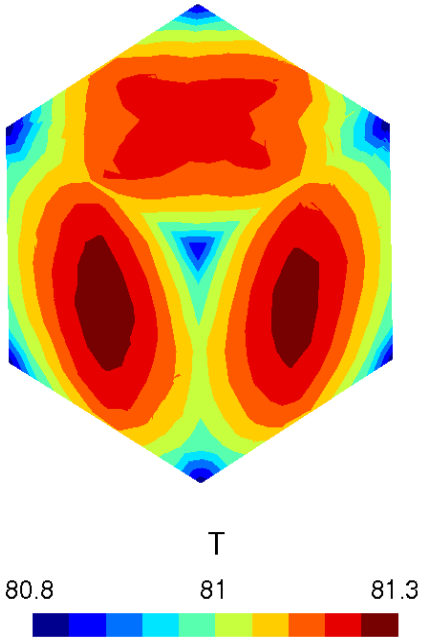

Figure 2.4 – Temperature distribution at $t = 20$ ms in the superconducting cube.

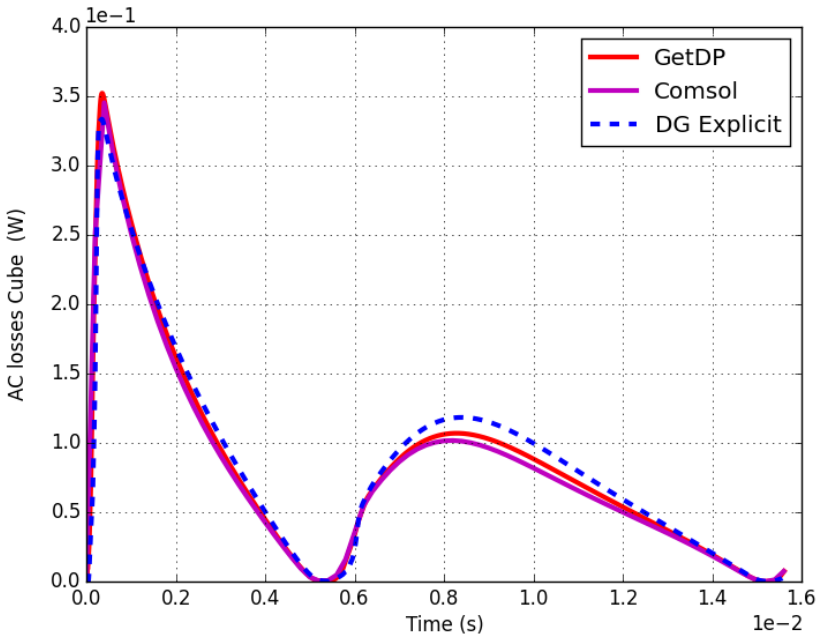

Figure 2.5 – AC losses in the thermal case of a superconducting cube subjected to an external magnetic field computed with GetDP, Comsol and the discontinuous galerkin method (DG) with the non-linear resistivity evaluated explicitly.

Computed AC losses, fig.2.5, remain equivalent for all the numerical approaches implemented. Because of the temperature dependence, a decrease of the critical current density is translated to the AC losses.

Using the same meshed cube model, computations in GetDP were performed in

2 hours. The time stepping algorithm and solvers for the matricial system resolution remain similar to the ones used in the case with no thermal coupling. Tolerances and time step remain unchanged too.

The distribution, shown in fig. 2.4, illustrates the elevation of temperature, below the critical state, occuring in the superconducting cube.

The allocated memory was about 2 GB for the new approach and about 6 GB for GetDP.

2.6 Conclusion

In this chapter, we investigated two numerical approaches to model in 3D high temperature superconductors. The first one was the finite element method, applied on the commonly used **H**-formulation coupled with the heat equation, implemented in GetDP and characterized by a linearization of the vectorial power law characterizing superconductors. Even though stability and convergence is provided by such method coupled with the power law linearization, memory allocation becomes limited with large scale problems.

Thus, we implemented the discontinuous galerkin method, applied on the same problem formulation used in GetDP, to overcome the memory limitations problem encountered in the finite element method. This method is naturally and highly parallelizable both in mesh size and resolution. The matricial system resolution and the mesh domain can then be distributed over numerous processors. In addition, fast computations will also occur for certain cases as we scale optimally over a large number of processors.

Good agreement is found between both numerical approaches as simple simulation cases are implemented. Comsol Multiphysics, commonly used for superconductor modelling, had its results implemented for the cube problem to validate the approach used in GetDP.

Chapter 3

3D modelling of twisted multi-filamentary superconducting wires

3.1 Introduction

In several large scale applications, superconducting machines [30] [65] use in some cases twisted multi-filamentary superconducting wires [66] as windings.

The structure of those wires consists of fine superconducting filaments embedded in a resistive matrix as a mechanical support. The matrix role is to protect mechanically all the superconducting filaments. The purpose of the wire is to allow the superconducting part to carry most of the high currents thus minimizing as much as possible the electric conduction of the resisitive matrix.

The described structure also help, along with the twisting process, reduce AC losses generated by the wire or tape. The geometric transformation resulting from the twisting process keep all the filaments, embedded in the resistive matrix, as much uncoupled as possible in order to get most of the current carried by all filaments.

A numerical and precise evaluation of AC losses generated by such wires is important for an efficient design of superconducting machines. It is also critical for the choice and design of an appropriate cryogenic system. Numerical tools developed in the previous chapter 2 provide useful frameworks to model 3D problems associated with those complex structures and configurations [55]. Complexities also encompass the highly non-linear electrical behaviour of high-temperature superconductors [14]-[13].

In this chapter, the focus will therefore be on the simplification of the 3D modelling of twisted multi-filamentary superconducting wires for fast and efficient AC losses computations.

First, we will investigate, with the help of the numerical approach of type finite element introduced and developed in chapter 2, the 3D modelling of complete twisted multi-filamentary wires with a single twist pitch length. Through those simulation cases, a mapping, allowing the simplification of the twisted wire 3D problem with an equivalent 3D problem in a frame where the wire becomes straight, will be developed and validated. Unlike the twisted multi-filamentary wire geometric complexities and the large number of degrees of freedom deriving from its associated 3D problem, the equivalent 3D problem in the new frame is characterized by a simple straight multi-filamentary wire geometry and a reduced number of degrees of freedom.

Then, approaches aimed at reducing the equivalent 3D problem size will be developed. They will take advantages of periodic conditions, possible because of both the straight wire section geometric uniformity along its length and the electric current uniformity at the wire center. Given a certain minimal wire length, the right approximation of AC losses per unit length of the wire will be possible. Reduced models will involve portions of the wire with at most the twist pitch as length. We will even see that, under a certain magnetic configuration, pseudo-2D model could give us a good approximation of AC losses per unit length.

With those reduced models, we will study, with AC losses measurements as references, the numerical analysis of the impact of elliptical fields on magnetization losses of a sample of 100 MgB_2 wires with 54 twisted filaments each.

Because of their reasonable size, all the models involved in this study were implemented in the finite element open source code GetDP [67].

3.2 Influence of a transverse magnetic field on a twisted mono-filament wire

In this study, we investigated the current distribution within a twisted mono-filament superconducting wire subjected to a sinusoidal transverse magnetic field. The wire is assumed to be a twist pitch long with a superconducting filament embedded in a Niobium matrix.

The 3D model used in the **H**-formulation is comprised of the wire completely

surrounded by a less resistive domain to approximate an air domain.

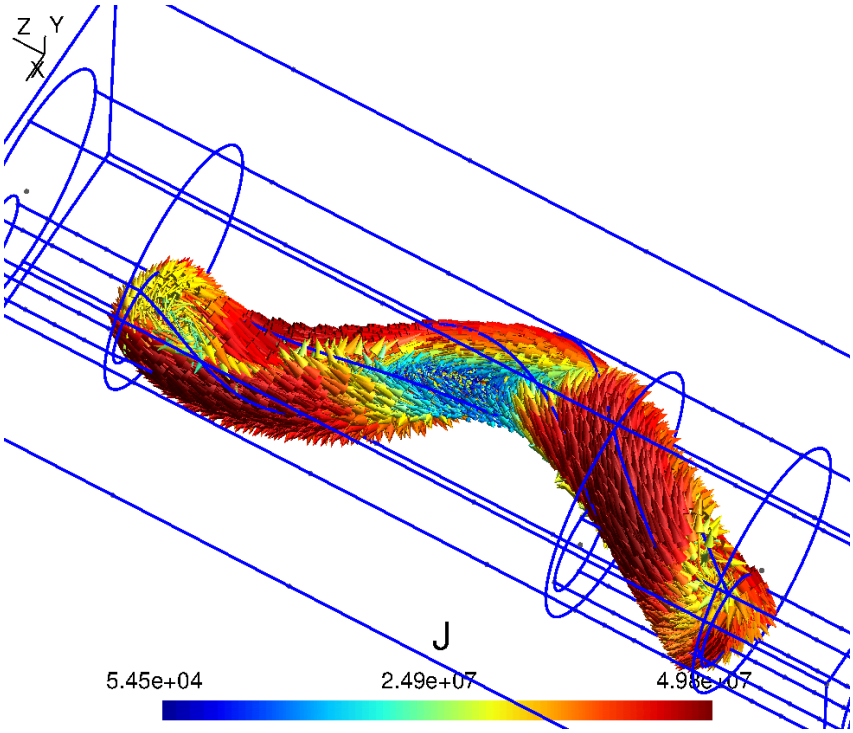

Figure 3.1 – 3D current density distribution inside the filament at $t = T/4s$

The computed current density distribution, resulting from the finite element method model in GetDP, gave an interesting result. Three current loops are locally created along the twisted superconducting filament as shown in fig.3.1.

Unlike the expected single current loop created inside a straight filament subjected to a transverse magnetic field, the unpredictable multiple current loops locally created inside the twisted filament suggests a different magnetic field configuration from the filament perspective.

Differences to a twisted and a straight filament subjected to a similar magnetic led us assume that the twisted superconducting filament observes, in the Frenet frame $(\mathbf{t}_f, \mathbf{n}_f, \mathbf{b}_f)$ moving along the helical trajectory originating from the twisting process, a transverse magnetic field with a directional change. This results from the fact that every point on the twisted superconducting filament sees the same external magnetic field.

The helical trajectory is associated with the geometric transformation of straight filaments into twisted filaments. $\mathbf{t}_f$, $\mathbf{n}_f$ and $\mathbf{b}_f$ are respectively the unit vector tangent, the normal unit vector and the binormal unit vector.

In order to confirm the previous assumption, an expression of the transformation must be derived and validated for numerical modelling purposes.

3.3 Mapping from a twisted mono-filament wire to a straight mono-filament wire

As described above, multiple local current loops appearing inside the twisted mono-filament mean the applied transverse magnetic field, unidirectional in the initial frame $\mathcal{B}_i = (\mathbf{i}, \mathbf{j}, \mathbf{k})$, is characterized with a directional change in the frame associated with the twisted filament.

The given frame is the Frenet frame $\mathcal{B}_f = (\mathbf{t}_f, \mathbf{n}_f, \mathbf{b}_f)$ which moves along the helical trajectory resulting from the twisting in the initial frame $\mathcal{B}_i = (\mathbf{i}, \mathbf{j}, \mathbf{k})$. Assuming the Frenet frame is the one fixed, the initial frame becomes the one moving along the mentioned helical trajectory and the twisted filament becomes straight.

Those observations must be derived in order to implement them for numerical simulations. A mapping from the initial frame $\mathcal{B}_i = (\mathbf{i}, \mathbf{j}, \mathbf{k})$ to the Frenet frame $\mathcal{B}_f = (\mathbf{t}_f, \mathbf{n}_f, \mathbf{b}_f)$ will be developed.

First, the parametric equations, in the initial frame, associated with the helical trajectory resulting from the twisting are :

$$\begin{cases} x = r\cos(\theta) \\ y = r\sin(\theta) \\ z = \dfrac{p}{2\pi}\theta \end{cases} \tag{3.1}$$

with $\theta \in [0, 2\pi]$, r the radius of the helix and p its twist pitch. Thus, the vector function associated to the helical trajectory will be :

$$\mathbf{r}(\theta) = r\cos(\theta)\ \mathbf{i} + r\sin(\theta)\ \mathbf{j} + \frac{p}{2\pi}\theta\ \mathbf{k} \tag{3.2}$$

The unit tangent, normal and binormal vectors of such trajectory are generally expressed as :

$$\mathbf{t}_f = \frac{d\mathbf{r}/d\theta}{|d\mathbf{r}/d\theta|} \tag{3.3}$$

$$\mathbf{n}_f = -\frac{d\mathbf{t}_f/d\theta}{|d\mathbf{t}_f/d\theta|} \tag{3.4}$$

$$\mathbf{b}_f = \mathbf{t}_f \times \mathbf{n}_f \tag{3.5}$$

The use of equation 3.2 in equations 3.3, 3.4 and 3.5 gives :

$$\mathbf{t}_f = \frac{1}{(r^2 + (p/2\pi)^2)^{1/2}}[-r\sin(\theta)\ \mathbf{i} + r\cos(\theta)\ \mathbf{j} + \frac{p}{2\pi}\ \mathbf{k}] \tag{3.6}$$

$$\mathbf{n}_f = \cos(\theta)\ \mathbf{i} + \sin(\theta)\ \mathbf{j} \tag{3.7}$$

$$\mathbf{b}_f = \frac{1}{(r^2 + (p/2\pi)^2)^{1/2}}[-\frac{p}{2\pi}\sin(\theta)\ \mathbf{i} + \frac{p}{2\pi}\cos(\theta)\ \mathbf{j} - r\ \mathbf{k}] \tag{3.8}$$

In addition to defining $a = r/L$, $b = c/L$, $c = p/2\pi$ and $L^2 = r^2 + c^2$, expressions in the Frenet frame of $\mathbf{i}$, $\mathbf{j}$ and $\mathbf{k}$, obtained from substitution applied on equations 3.6, 3.7 and 3.8, are :

$$\mathbf{i} = -a\sin(\theta)\ \mathbf{t}_f + \cos(\theta)\ \mathbf{n}_f - b\sin(\theta)\ \mathbf{b}_f \tag{3.9}$$

$$\mathbf{j} = a\cos(\theta)\ \mathbf{t}_f + \sin(\theta)\ \mathbf{n}_f + b\cos(\theta)\ \mathbf{b}_f \tag{3.10}$$

$$\mathbf{k} = b\ \mathbf{t}_f - a\ \mathbf{b}_f \tag{3.11}$$

Thus, the transition matrix from the initial frame basis vectors $\mathcal{B}_i$ to the Frenet frame basis vectors $\mathcal{B}_f$ is :

$$P_{\mathcal{B}_f}^{\mathcal{B}_i} = \begin{bmatrix} -a\cdot\sin(\theta) & a\cdot\cos(\theta) & b \\ \cos(\theta) & \sin(\theta) & 0 \\ -b\cdot\sin(\theta) & b\cdot\cos(\theta) & -a \end{bmatrix} \tag{3.12}$$

Both basis vectors are orthonormal. Therefore, the transition matrices $P_{\mathcal{B}_f}^{\mathcal{B}_i}$ and $P_{\mathcal{B}_i}^{\mathcal{B}_f}$ are both orthogonal and invertible such that :

$$P_{\mathcal{B}_i}^{\mathcal{B}_f} = (P_{\mathcal{B}_f}^{\mathcal{B}_i})^{-1} = (P_{\mathcal{B}_f}^{\mathcal{B}_i})^T \tag{3.13}$$

The mapping between both basis vectors is thus mathematically valid. In either frame, the frame we depart from is assumed moving along the helical trajectory. Depending on the air domain geometry, the helix radius r will be set as :

- half of the diagonal length of the air domain top and bottom surfaces if it is a box

– the radius of the air domain base surfaces if it is a cylinder

The differential operators describing the domain physics will remain unchanged in whatever frame we will be working on.

However, the external boundary conditions they are subjected to must be changed. For instance, the external magnetic field applied to a twisted superconducting wire must be transformed in the Frenet frame where the wire becomes straight as shown in fig.3.2.

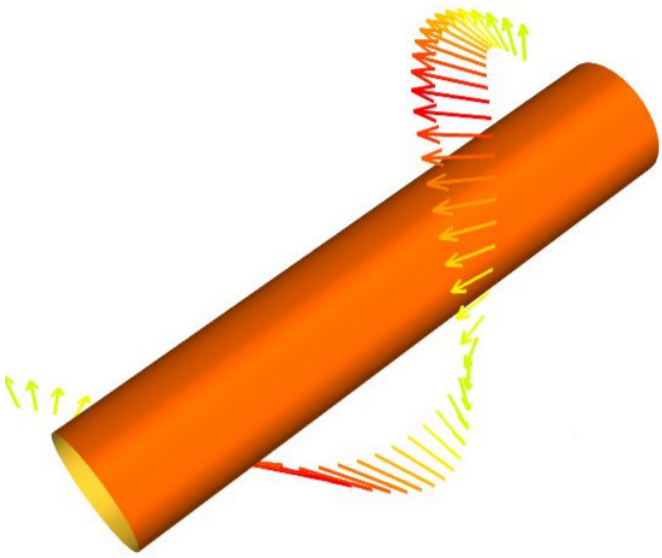

Figure 3.2 – 3D filament subjected to a transverse magnetic field in the Frenet frame

Thus, the mathematical expression of the geometric transformation applied to the magnetic field **H** will be the following :

$$\mathbf{H}_{[\mathbf{T},\mathbf{N},\mathbf{K}]} = \begin{bmatrix} -a \cdot \sin(\theta) & a \cdot \cos(\theta) & b \\ \cos(\theta) & \sin(\theta) & 0 \\ -b \cdot \sin(\theta) & b \cdot \cos(\theta) & -a \end{bmatrix} \cdot \mathbf{H}_{[\mathbf{x},\mathbf{y},\mathbf{z}]} \tag{3.14}$$

with $\theta = z/c$.

In the Frenet frame, we computed the current density distribution of the previously mentioned twisted mono-filament superconducting wire subjected to an external magnetic field. However, the applied magnetic field is now the transformed form of the external magnetic field used in the initial frame $(\mathbf{x}, \mathbf{y}, \mathbf{z})$ shown in the previous case. We therefore have an external magnetic field with a directional change along the helical trajectory associated to the transformation as shown in fig. 3.2.

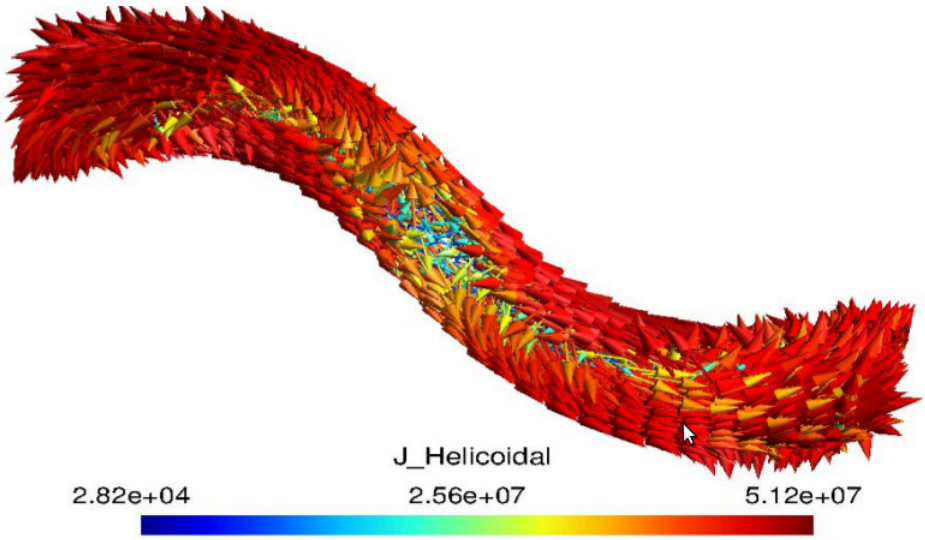

Figure 3.3 – 3D current density distribution inside the filament in the Frenet frame at $t = T/4s$

The computed current density shows in fig. 3.3 a single loop of current inside the filament. The studied case computed in the Frenet frame is thus equivalent to the case of a straight mono-filament superconducting wire subjected to a unidirectional transverse magnetic field. Moreover, the geometry of the resistive matrix remain straight despite such transformation because it is assumed non-magnetic [73].

3.4 Mapping validation on a twisted bi-filaments wire

The geometric transformation described above will be investigated for a twisted bi-filaments superconducting wire subjected to a unidirectional sinusoidal magnetic field (cases in transverse field and cases in axial field). The wire is assumed to have a single twist pitch length. Both superconducting filaments, radially distributed on a single layer, are embedded in a Niobium matrix with an air domain surrounding both filaments and matrix. The model parameters are shown in the table 3.1. Its geometry with and without the mapping are also shown in figures 3.4a and 3.4b.

The objective is to compare modelling cases, through computed AC losses, with and without the geometric transformation in order to check any equivalence between the two problems (initial and transformed ones). The transformed magnetic field becomes bi-directional unlike the unidirectional magnetic field imposed in the initial frame. In both cases, a parametric study, involving the twist pitch p and the

Table 3.1 – Bi-filaments superconducting wire parameters

Quantity	Value
Twist pitch p (mm)	4 or 8 or 16
Filament radius (μm)	50
Matrix radius (mm)	0.6
Air radius (mm)	$4p$
Layer radius (mm)	0.1
Critical current density (A/mm^2)	5
Power law index n	10
Air conductivity (S/m)	10^3
Matrix conductivity (S/m)	$6{\cdot}10^9$
Magnetic field amplitude B_{max} (mT)	50 or 100 or 200
Frequency f (Hz)	50
Magnetic field norm	$B_m \sin(2\pi f)$

magnetic field amplitude B_{max} as variables, will be done.

Comparisons of AC losses results obtained from both problems (initial and transformed ones) will effectively show equivalence no matter the parameters set for the twisted bi-filaments wire. Moreover, we will observe that, unlike the problem with twisted filaments, the equivalent problem with straight filaments will always require, in addition to a simple geometry, at least 50% less degree of freedoms to approximate the solution.

Computations were done using the open source finite element code GetDP. The implicit Euler method, used as a time stepping algorithm, was coupled with both iterative and direct methods as matricial sytem solvers. Solvers such as preonly and lu from the PETSc (Portable, Extensible Toolkit for Scientific Computation) library were used simultaneously with MUMPS (Multifrontal Massively Parallel sparse direct Solver). With an initial timestep of 5.10^{-6} s subjected to an adaptive time-stepping scheme, the implicit Euler method tolerances were set to 10^{-6} and 10^{-6} for the absolute and relative residuals respectively.

Comparisons of those different configurations will be emphasized on the computed AC losses generated by the studied wires. For each defined parameters p and B_{max}, computed AC losses, in both modeling case in the initial frame and its associated transformed case in the Frenet frame, will be compared. Magnetization will be also computed and compared for some cases.

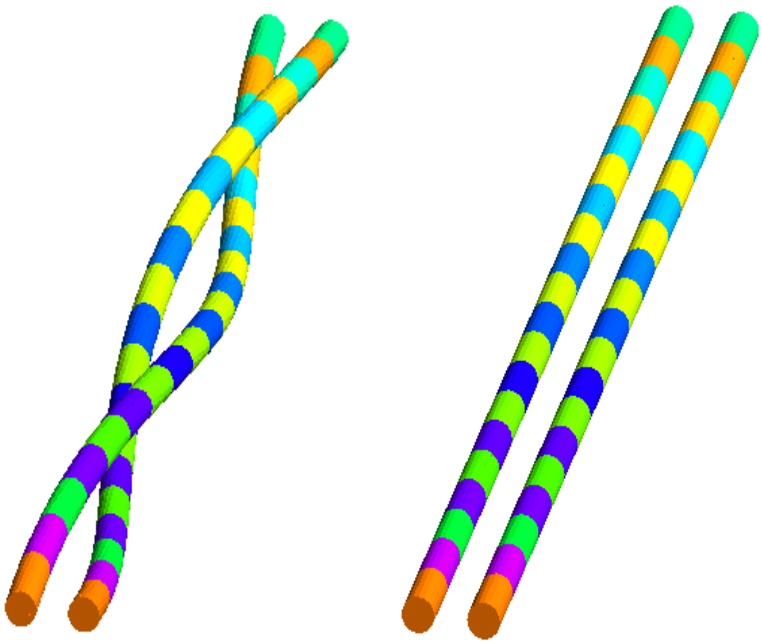

(a) Initial frame (b) Frenet frame

Figure 3.4 – Filaments of both twisted and equivalent straight bi-filaments superconducting wire of length $p = 4$ mm

3.4.1 Twisted bi-filaments superconducting wire subjected to a transverse magnetic field along the y-axis

Case 1 : $B_{max} = 50$ **mT**

In this case, superconducting filaments are fully penetrated in current because of the low critical current density and the high magnetic field. Therefore, coupling losses generated within the matrice make up the most of AC losses generated within the wire (see fig.3.5a, 3.5b and 3.5c).

For each defined twist pitch, we notice that computed AC losses over a quarter of cycle, as shown in figures 3.5a, 3.5b and 3.5c, are equivalent in both the initial frame and the Frenet frame.

The computed magnetization losses and magnetization over the y-axis of the filaments only remain also equivalent in both frames as shown in figures 3.7a and 3.7b. The current density vector distributions, shown in figures 3.6a, 3.6b and 3.6c, are also equivalent.

However, more elements were needed from the filaments of the twisted wire geometry to reach the equivalence. The meshed twisted wire had 108777 elements

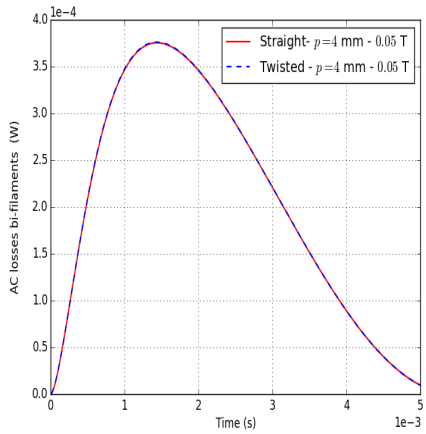

(a) $p = 4$ mm

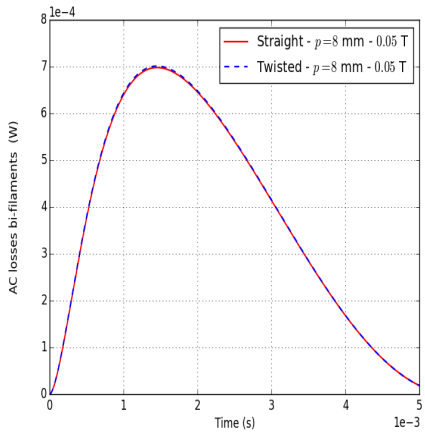

(b) $p = 8$ mm

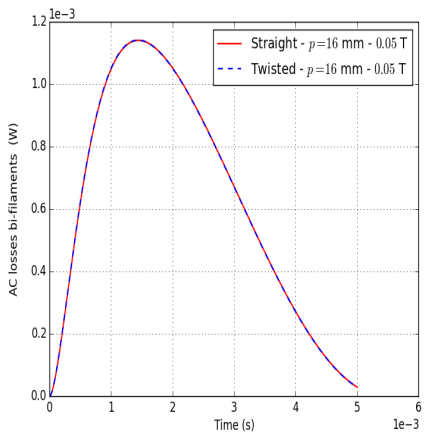

(c) $p = 16$ mm

Figure 3.5 – AC losses comparison of a bi-filaments superconducting wire of different twist pitch lengths subjected to a transverse magnetic field with $B_{max} = 50$ mT in both the initial and Frenet frames.

while the meshed straight wire had 70856 elements.

Case 2 : $B_{max} = 100$ mT

Coupling losses of the wire remain the highest in comparison with magnetization losses. The increase of the magnetic field amplitude means an increase of the losses generated within the wire in comparison with the ones computed when $B_{max} = 50$ mT.

For each defined twist pitch, we notice that computed AC losses, as shown in figures 3.8a, 3.8b and 3.8c, are similar in both the initial frame and the Frenet frame.

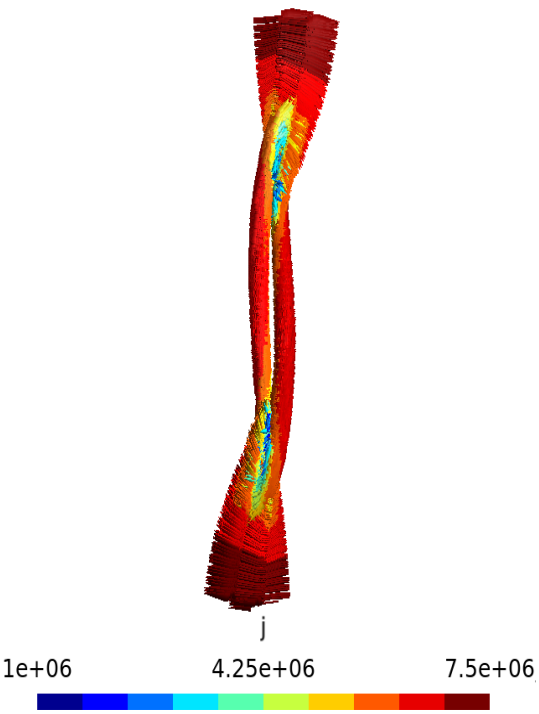

(a) Initial frame

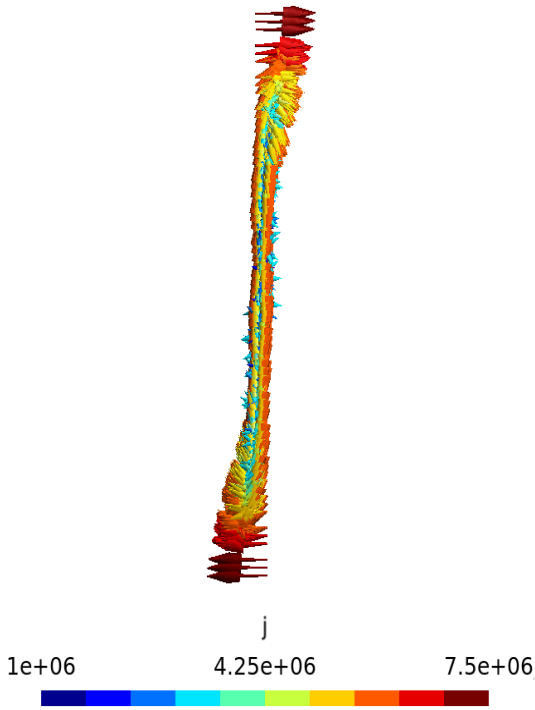

(b) Frenet frame

(c) Initial frame via Frenet frame with the use of $(P_{\mathcal{B}_f}^{\mathcal{B}_i})^{-1}$

Figure 3.6 – Current density vector distribution at $t = 1.5$ ms inside the superconducting domain of a bi-filaments superconducting wire of length $p = 4$ mm subjected to a transverse magnetic field with $B_{max} = 50$ mT in both the initial and Frenet frames.

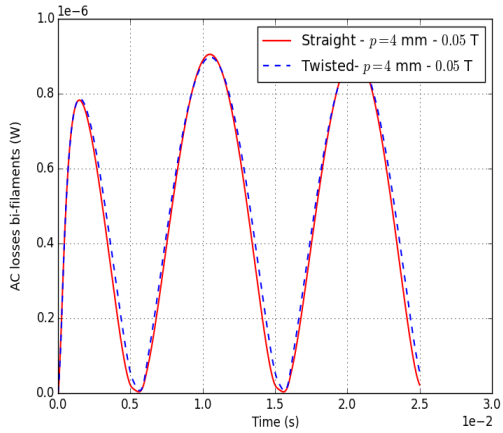

(a) Magnetization losses

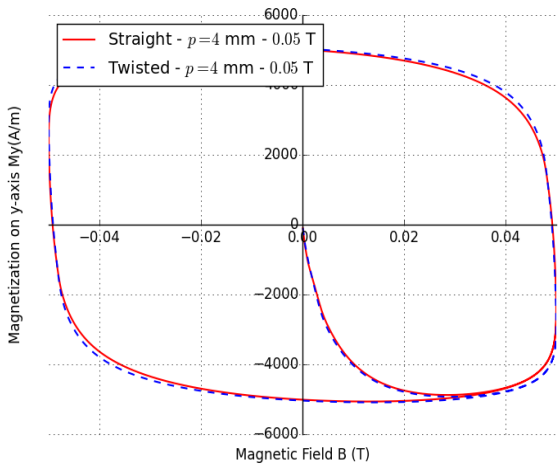

(b) Average magnetization

Figure 3.7 – Magnetization losses and computed average magnetization along the y-axis comparison of a bi-filaments superconducting wire of twist pitch length subjected to a transverse magnetic field with $B_{max} = 50$ mT in both the initial and Frenet frames.

Case 3 : $B_{max} = 200$ **mT**

Coupling losses generated within the wire are the highest in comparison with the ones computed when $B_{max} = 50$ mT and $B_{max} = 100$ mT.

For each defined twist pitch, we notice that computed AC losses, as shown in figures 3.9a, 3.9b and 3.9c, are similar in both the initial frame and the Frenet frame.

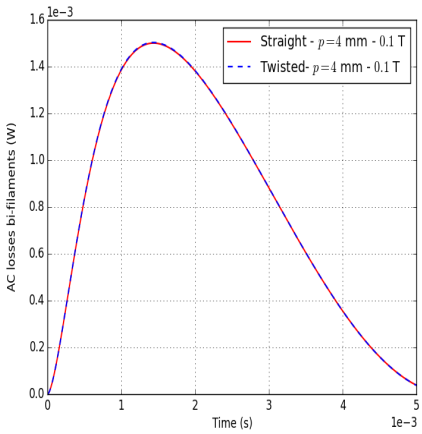

(a) $p = 4$ mm

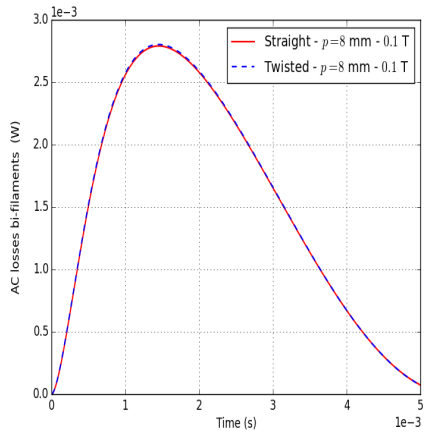

(b) $p = 8$ mm

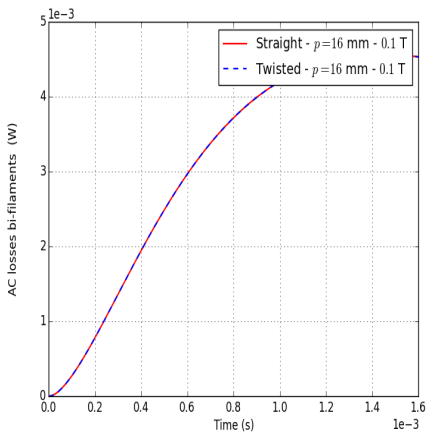

(c) $p = 16$ mm

Figure 3.8 – AC losses comparison of a bi-filaments superconducting wire of of different twist pitch lengths subjected to a transverse magnetic field with $B_{max} =$ 100 mT in both the initial and Frenet frames.

3.4.2 Twisted bi-filaments superconducting wire subjected to an axial magnetic field along the z-axis

Case 1 : $B_{max} = 50$ **mT**

In this case, coupling losses generated within the matrice still make up the most of AC losses generated within the wire (see fig.3.10a, 3.10b and 3.10c).

For each defined twist pitch, we notice that computed AC losses, as shown in figures 3.10a, 3.10b and 3.10c, are similar in both the initial frame and the Frenet frame.

The computed magnetization losses and magnetization over the z-axis of the filaments only remain also equivalent in both frames as shown in figures 3.12a and

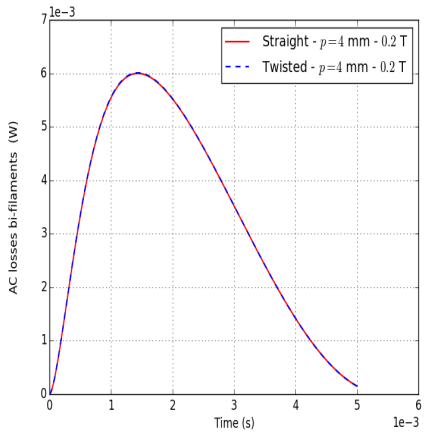

(a) $p = 4$ mm

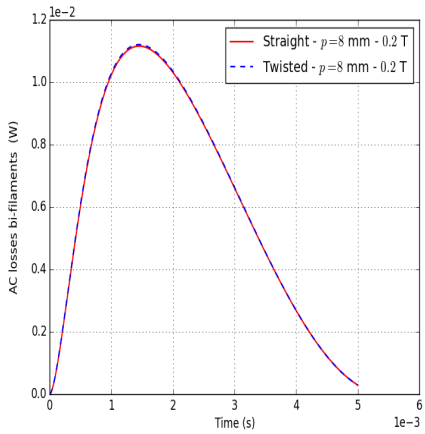

(b) $p = 8$ mm

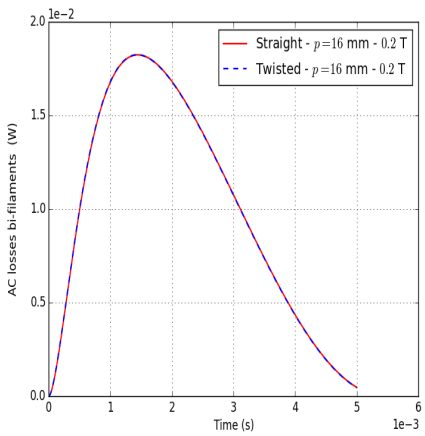

(c) $p = 16$ mm

Figure 3.9 – AC losses comparison of a bi-filaments superconducting wire of of different twist pitch lengths subjected to a transverse magnetic field with $B_{max} =$ 200 mT in both the initial and Frenet frames.

3.12b. The current density vector distributions, shown in figures 3.11a, 3.11b and 3.11c, are also equivalent.

However, more elements were still needed from the filaments of the twisted wire geometry to reach the equivalence. The meshed twisted wire had 108777 elements while the meshed straight wire had 53719 elements.

Case 2 : $B_{max} = 100$ **mT**

Coupling losses of the wire remain the highest in comparison with magnetization losses. The increase of the magnetic field amplitude means an increase of the losses generated within the wire in comparison with the ones computed when $B_{max} = 50$ mT.

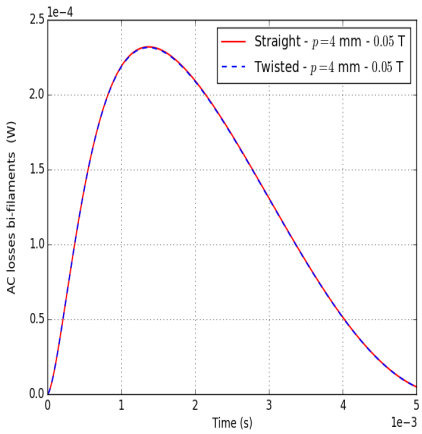

(a) $p = 4$ mm

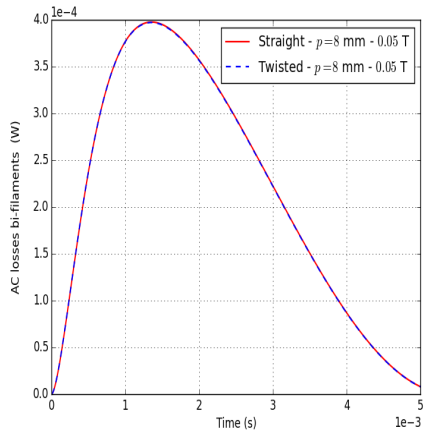

(b) $p = 8$ mm

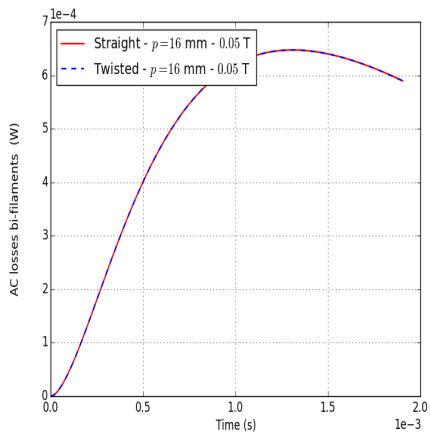

(c) $p = 16$ mm

Figure 3.10 – AC losses comparison of a bi-filaments superconducting wire of of different twist pitch lengths subjected to an axial magnetic field with $B_{max} = 50$ mT in both the initial and Frenet frames.

For each defined twist pitch, we notice that computed AC losses, as shown in figures 3.13a, 3.13b and 3.13c, are similar in both the initial frame and the Frenet frame.

Case 3 : $B_{max} = 200$ mT

Coupling losses of the wire still remain the highest in comparison with magnetization losses. The increase of the magnetic field amplitude means an increase of the losses generated within the wire in comparison with the ones computed when $B_{max} = 200$ mT.

For each defined twist pitch, we notice that computed AC losses, as shown in figures 3.14a, 3.14b and 3.14c, are similar in both the initial frame and the Frenet

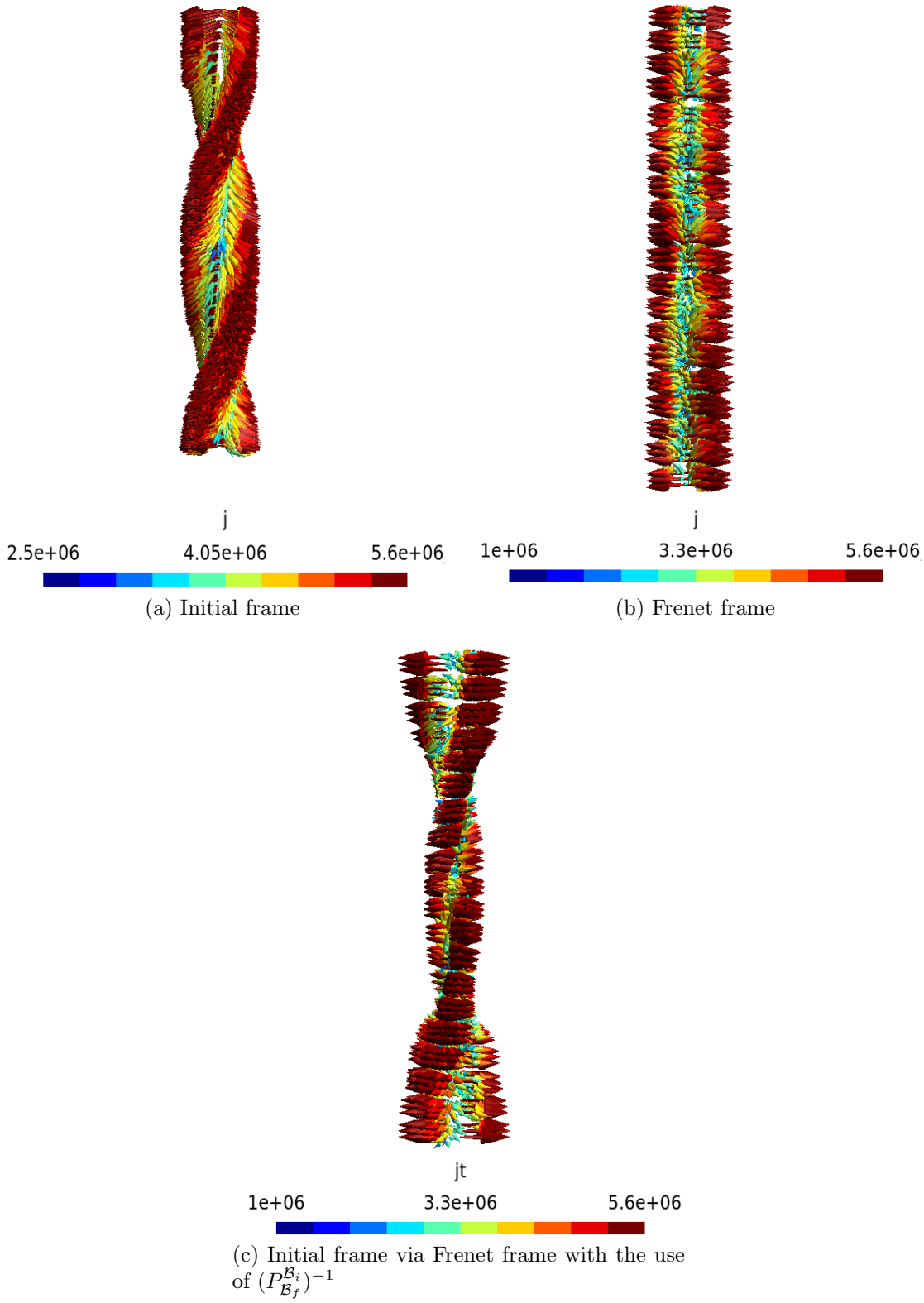

(a) Initial frame

(b) Frenet frame

(c) Initial frame via Frenet frame with the use of $(P_{\mathcal{B}_f}^{\mathcal{B}_i})^{-1}$

Figure 3.11 – Current density vector distribution at $t = 1.5$ ms inside the superconducting domain of a bi-filaments superconducting wire of length $p = 4$ mm subjected to an axial magnetic field with $B_{max} = 50$ mT in both the initial and Frenet frames.

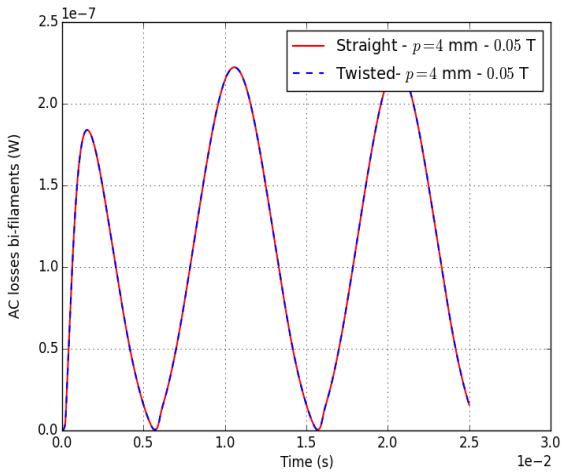

(a) Magnetization losses

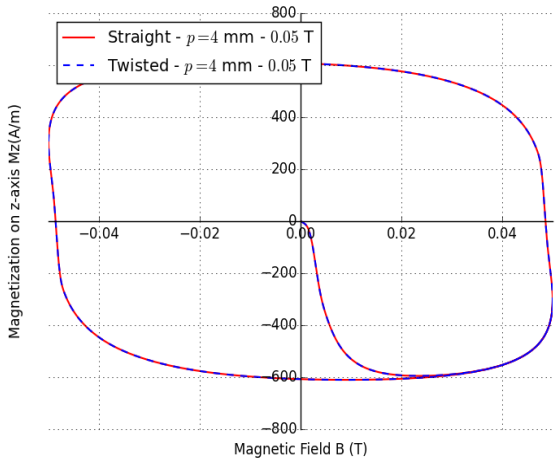

(b) Average magnetization

Figure 3.12 – Magnetization losses and computed average magnetization along the y-axis comparison of a bi-filaments superconducting wire of twist pitch length subjected to an axial magnetic field with B_{max} = 50 mT in both the initial and Frenet frames.

frame.

3.5 Mapping validation on a twisted six-filaments wire

An additional investigation of the geometric transformation has been done on a twisted six-filaments superconducting wire subjected to a unidirectional sinusoidal magnetic field (cases in transverse field and cases in axial field). The wire is assumed to have a single twist pitch length. In addition to two superconducting filaments belonging to a first layer, there is a second layer with four filaments. All those

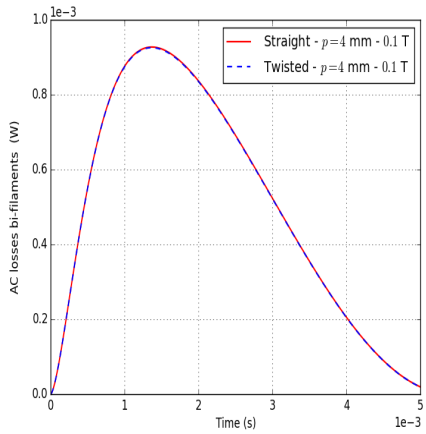

(a) $p = 4$ mm

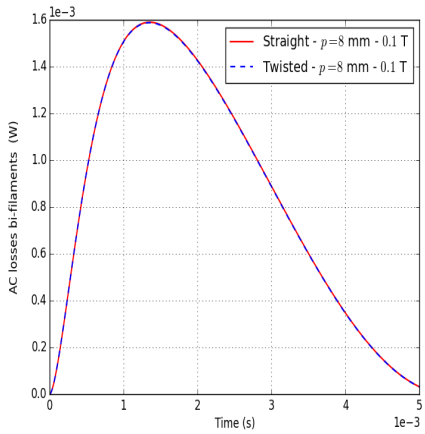

(b) $p = 8$ mm

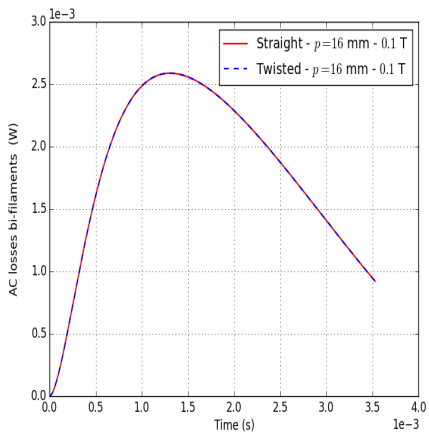

(c) $p = 16$ mm

Figure 3.13 – AC losses comparison of a bi-filaments superconducting wire of of different twist pitch lengths subjected to an axial magnetic field with $B_{max} = 100$ mT in both the initial and Frenet frames.

filaments are still embedded in a Niobium matrix with an air domain surrounding both filaments and matrix. The model parameters are shown in the table 3.2.Its geometry with and without the mapping are also shown in figures 3.15a and 3.15b.

Similarly as the study of the twisted bi-filament wire, the goal is to compare modelling cases, through computed AC losses, with and without the geometric transformation in order to check any equivalence. In both cases, a parametric study, involving the twist pitch p and the magnetic field amplitude B_{max} as variables, will be done.

Comparisons of AC losses results obtained from both problems (initial and transformed ones) will also effectively show equivalence no matter the parameters set for the twisted six-filaments wire. Moreover, we will also observe that, unlike

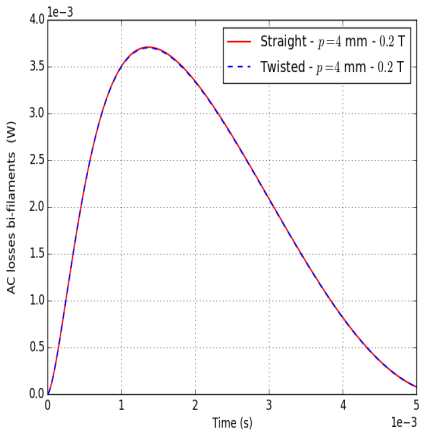

(a) $p = 4$ mm

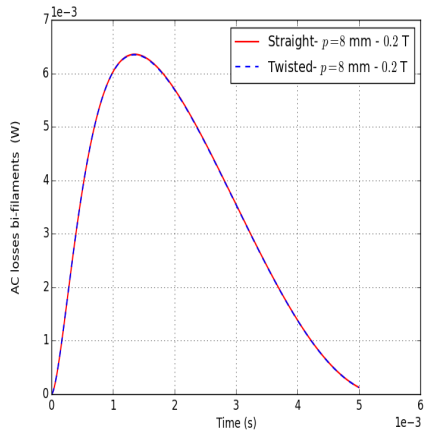

(b) $p = 8$ mm

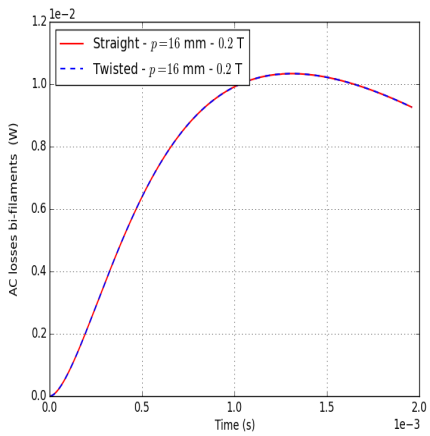

(c) $p = 16$ mm

Figure 3.14 – AC losses comparison of a bi-filaments superconducting wire of of different twist pitch lengths subjected to an axial magnetic field with $B_{max} = 200$ mT in both the initial and Frenet frames.

the problem with twisted filaments, the equivalent problem with straight filaments will always require less degree of freedoms to approximate the solution.

Comparisons of those different configurations will be emphasized on the computed AC losses generated by the studied wires. For each defined parameters p and B_{max}, computed AC losses, in both modeling case in the initial frame and its associated transformed case in the Frenet frame, will be compared.

Table 3.2 – Six-filaments superconducting wire parameters

Quantity	Value
Twist pitch p (mm)	4 or 8 or 16
Filament radius (μm)	50
Matrix radius (mm)	0.6
Air radius (mm)	$4p$
Layer 1 radius (mm)	0.1
Layer 2 radius (mm)	0.3
Critical current density (A/mm^2)	5
Power law index n	10
Air conductivity (S/m)	10^3
Matrix conductivity (S/m)	$6{\cdot}10^9$
Magnetic field amplitude B_{max} (mT)	50 or 100 or 200
Frequency f (Hz)	50
Magnetic field norm	$B_m \sin(2\pi f)$

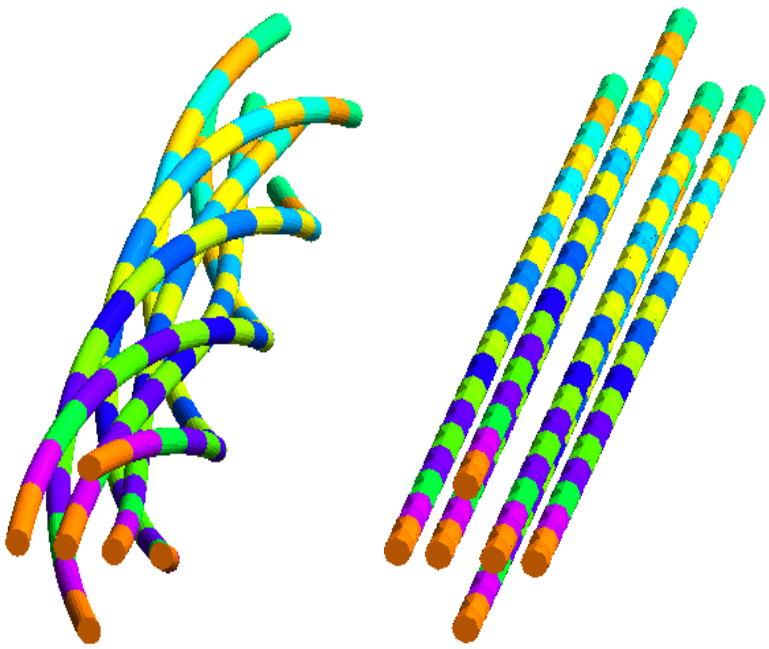

(a) Initial frame (b) Frenet frame

Figure 3.15 – Filaments of both twisted and equivalent straight six-filaments superconducting wire of length $p = 4$ mm

3.5.1 Twisted six-filaments superconducting wire subjected to a transverse magnetic field along the y-axis

Case 1 : $B_{max} = 50mT$

In this case, superconducting filaments are fully penetrated in current because of the low critical current density and the high magnetic field. Therefore, coupling losses generated within the matrice make up the most of AC losses generated within the wire (see fig.3.16a, 3.16b and 3.16c).

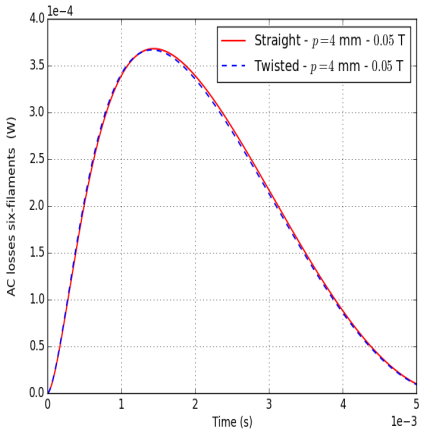

(a) $p = 4$ mm

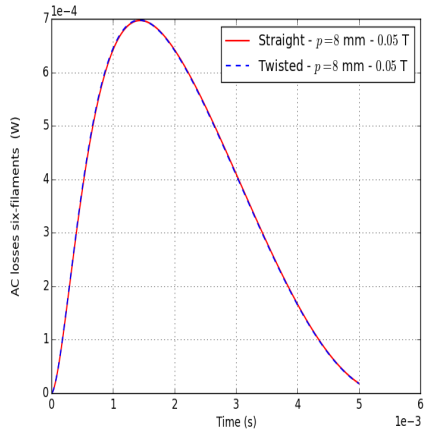

(b) $p = 8$ mm

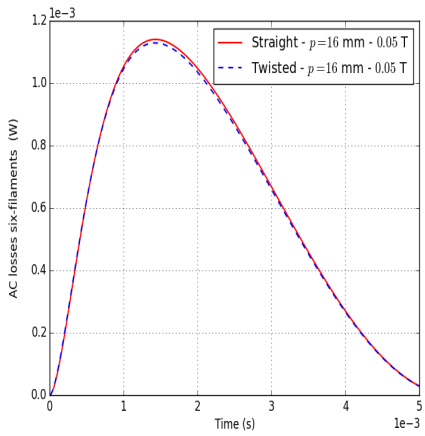

(c) $p = 16$ mm

Figure 3.16 – AC losses comparison of a six-filaments superconducting wire of different twist pitch lengths subjected to a transverse magnetic field with $B_{max} = 50$ mT in both the initial and Frenet frames.

For each defined twist pitch, we notice that computed AC losses, as shown in figures 3.16a, 3.16b and 3.16c, are similar in both the initial frame and the Frenet frame.

The computed magnetization losses and magnetization over the y-axis of the filaments only remain also equivalent in both frames as shown in figures 3.17a and 3.17b. However, more elements were needed from the filaments of the twisted wire geometry to reach the equivalence. The meshed twisted wire had 381106 elements while the meshed straight wire had 82500 elements.

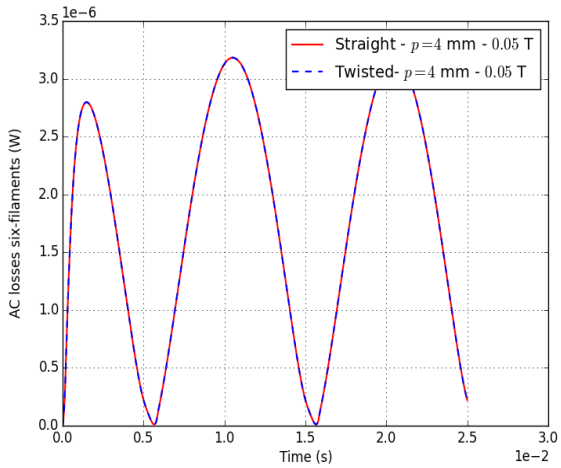

(a) Magnetization losses

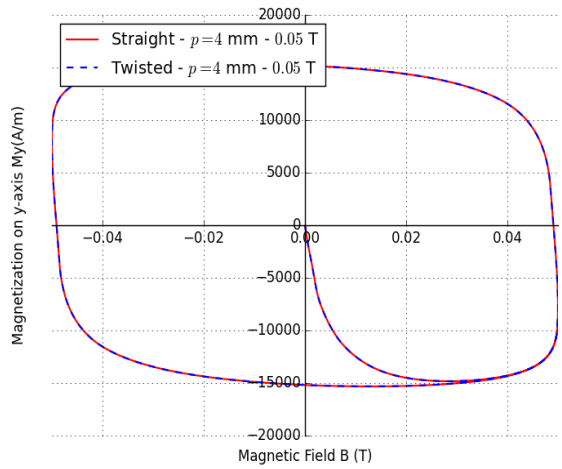

(b) Average magnetization

Figure 3.17 – Magnetization losses and computed average magnetization along the y-axis comparison of a six-filaments superconducting wire of twist pitch length subjected to a transverse magnetic field with $B_{max} = 50$ mT in both the initial and Frenet frames.

Case 2 : $B_{max} = 100mT$

Coupling losses of the wire remain the highest in comparison with magnetization losses. The increase of the magnetic field amplitude means an increase of the losses generated within the wire in comparison with the ones computed when $B_{max} = 50$ mT.

For each defined twist pitch, we notice that computed AC losses, as shown in figures 3.18a, 3.18b and 3.18c, are similar in both the initial frame and the Frenet frame.

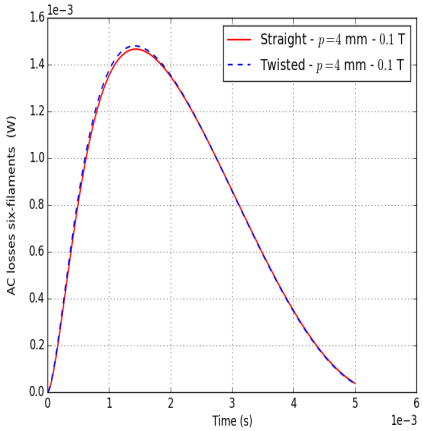

(a) $p = 4$ mm

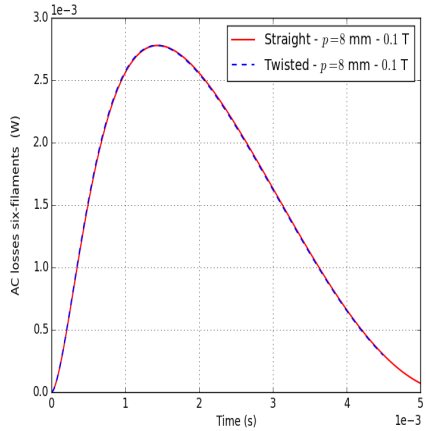

(b) $p = 8$ mm

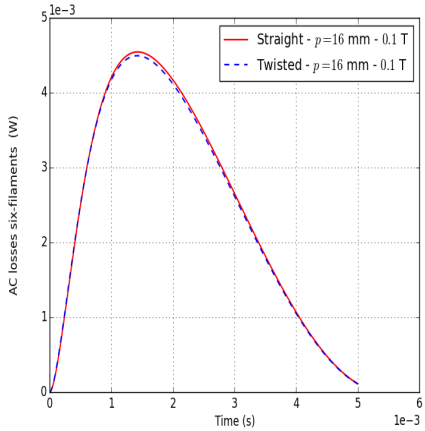

(c) $p = 16$ mm

Figure 3.18 – AC losses comparison of a six-filaments superconducting wire of different twist pitch lengths subjected to a transverse magnetic field with $B_{max} =$ 100 mT in both the initial and Frenet frames.

Case 3 : $B_{max} = 200mT$

Coupling losses of the wire remain the highest in comparison with magnetization losses. The increase of the magnetic field amplitude means an increase of the losses generated within the wire in comparison with the ones computed when $B_{max} = 100$ mT.

For each defined twist pitch, we notice that computed AC losses, as shown in figures 3.19a, 3.19b and 3.19c, are similar in both the initial frame and the Frenet

frame.

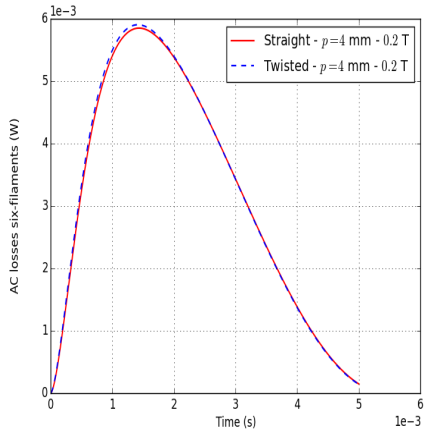

(a) $p = 4$ mm

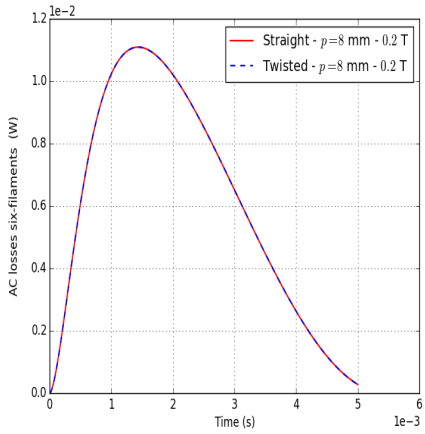

(b) $p = 8$ mm

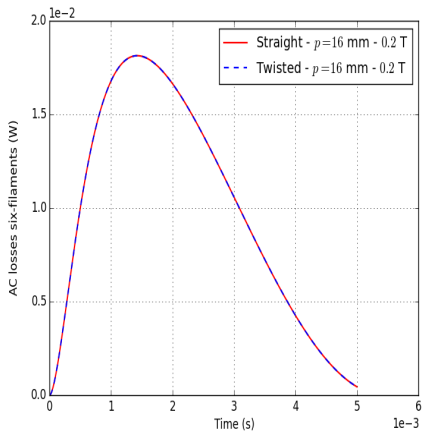

(c) $p = 16$ mm

Figure 3.19 – AC losses comparison of a six-filaments superconducting wire of different twist pitch lengths subjected to a transverse magnetic field with $B_{max} =$ 200 mT in both the initial and Frenet frames.

3.5.2 Twisted six-filaments superconducting wire subjected to an axial magnetic field along the z-axis

Case 1 : $B_{max} = 50mT$

In this case, the superconducting filaments are not fully penetrated in current because of both the low magnetic field amplitude and the defined superconductor parameters.

For each defined twist pitch, we notice that computed AC losses, as shown in figures 3.20a and 3.20b are similar in both the initial frame and the Frenet frame.

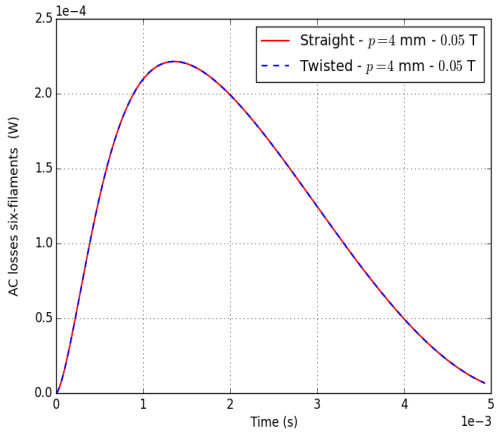

(a) $p = 4$ mm

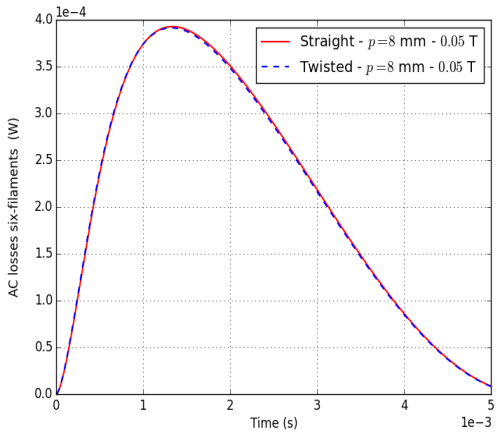

(b) $p = 8$ mm

Figure 3.20 – AC losses comparison of a six-filaments superconducting wire of different twist pitch lengths subjected to an axial magnetic field with $B_{max} = 50$ mT in both the initial and Frenet frames.

The computed magnetization losses and magnetization over the z-axis of the filaments only remain also equivalent in both frames as shown in figures 3.21a and 3.21b. However, more elements were needed from the filaments of the twisted wire geometry to reach the equivalence. The meshed twisted wire had 381106 elements while the meshed straight wire had 82500 elements.

Case 2 : $B_{max} = 100mT$

Coupling losses of the wire remain the highest in comparison with magnetization losses. The increase of the magnetic field amplitude means an increase of the losses generated within the wire in comparison with the ones computed when $B_{max} = 50$ mT.

For each defined twist pitch, we notice that computed AC losses, as shown in

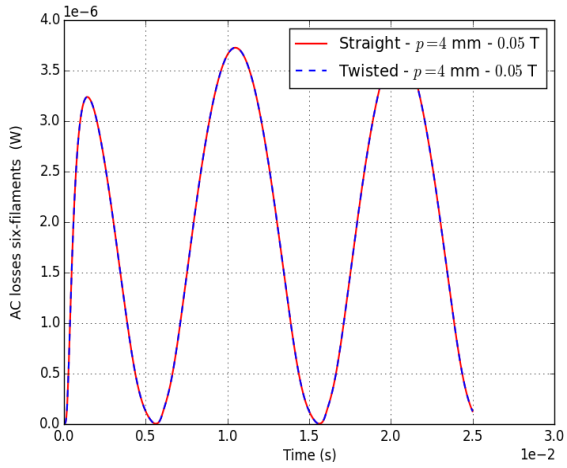

(a) Magnetization losses

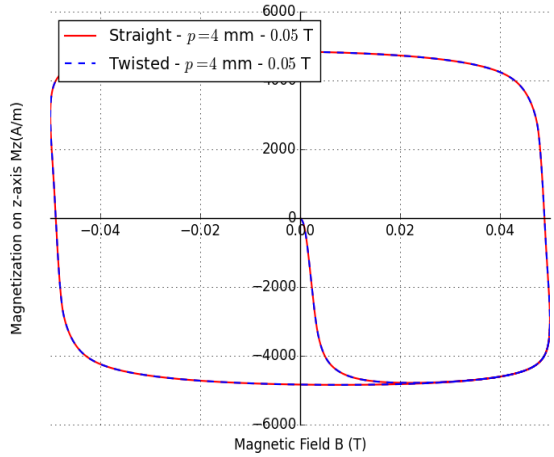

(b) Average magnetization

Figure 3.21 – Magnetization losses and computed average magnetization along the y-axis comparison of a six-filaments superconducting wire of twist pitch length subjected to an axial magnetic field with B_{max} = 50 mT in both the initial and Frenet frames.

figures 3.22a and 3.22b, are similar in both the initial frame and the Frenet frame.

Case 3 : $B_{max} = 200mT$

Coupling losses of the wire remain the highest in comparison with magnetization losses. The increase of the magnetic field amplitude means an increase of the losses generated within the wire in comparison with the ones computed when B_{max} = 100 mT.

For each defined twist pitch, we notice that computed AC losses, as shown in figures 3.23a and 3.23b, are similar in both the initial frame and the Frenet frame.

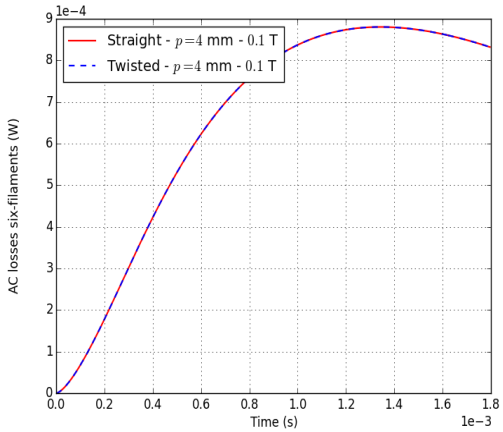

(a) $p = 4$ mm

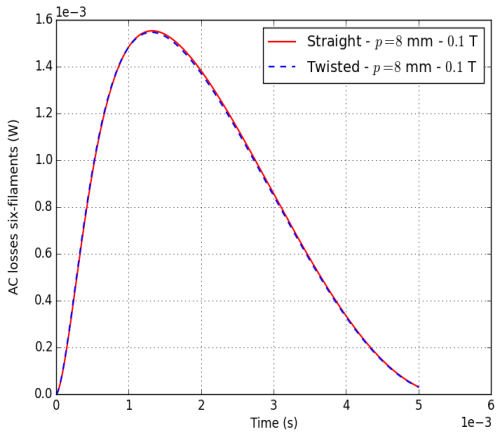

(b) $p = 8$ mm

Figure 3.22 – AC losses comparison of a six-filaments superconducting wire of different twist pitch lengths subjected to an axial magnetic field with $B_{max} = 100$ mT in both the initial and Frenet frames.

3.6 Study of multi-filamentary wires with multiple twist pitch

Simulations cases done on both complete twisted bi-filaments and six-filaments wires validate the mapping proposed above. Thus, a three-dimensional modelling of an equivalent complete straight filaments wire in the Frenet frame is possible. It allows to deal with a simple geometry and its associated problem requires less degrees of freedoms than the problem with twisted filaments.

Although such an equivalence and simplification is possible, problems associated with the modelling of twisted multi-filamentary superconducting wire with multiple twist pitch remain large in terms of degrees of freedoms number. This is due to the commonly great length (several twist pitches) of wires geared for real applications.

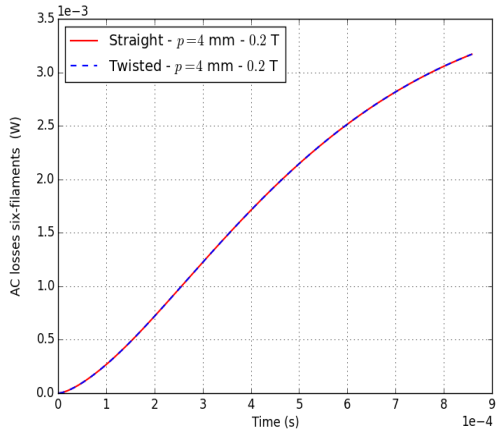

(a) $p = 4$ mm

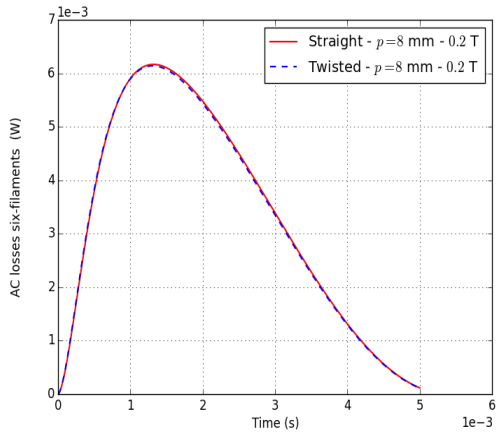

(b) $p = 8$ mm

Figure 3.23 – AC losses comparison of a six-filaments superconducting wire of different twist pitch lengths subjected to an axial magnetic field with $B_{max} = 200$ mT in both the initial and Frenet frames.

We will therefore investigate approaches to reduce the size of problems associated with multi-filamentary superconducting wires with several twist pitch subjected to an external magnetic field. In this study, every simulation case will be done in the Frenet frame on a six-filaments superconducting wire.

Parameters of the study are shown in the table 3.2. Cases of transverse field and axial field will be both explored as external magnetic field.

3.6.1 Influence of the number of twist pitch

The study of straight filaments wires with multiple twist pitch in the Frenet frame can allow, because of the wire section geometric uniformity no matter the wire height position, the potential use of periodic conditions over a single twist pitch as

Table 3.3 – Parameters of a six-filaments superconducting wire with multiple twist pitch

Quantity	Value
Twist pitch p (mm)	4
number of twist pitch n_p	3 or 5 or 7
Filament radius (μm)	50
Matrix radius (mm)	0.6
Air radius (mm)	$4.p.n_p$
Layer 1 radius (mm)	0.1
Layer 2 radius (mm)	0.3
Critical current density (A/mm^2)	5
Power law index n	10
Air conductivity (S/m)	10^3
Matrix conductivity (S/m)	$6{\cdot}10^9$
Magnetic field amplitude B_{max} (mT)	50
Frequency f (Hz)	100

an equivalent reduced model.

This potential is also due to the fact that the current induced and circulating inside the wire remains uniform. Thus, a precise evaluation of AC losses per unit length at one of the wire portion of twist pitch length located approximately at the wire center can give us, assuming the wire is long enough that its ends magnetic influence at its center are negligible, a good enough approximation of the entire wire AC losses.

With periodic conditions set at both top and bottom ends of the truncated wire of twist pitch length, the possibility of reducing the problem is there. However, we have to garantee that the modelled behaviour of the truncated wire is sufficient enough to predict AC losses of the whole wire.

In order to ensure such prediction, numerous simulation cases over multiple twist pitch have been done. Thoses studies consisted in finding the minimum number of twist pitch where AC losses per unit length, evaluated on the whole wire with multiple twist pitch, become equivalent to the ones of a single twist pitch wire with periodic boundary conditions imposed.

As shown in figure 3.24 and 3.25, the greater the number of twist pitch becomes, the closer AC losses per unit length are getting to the ones of a single twist pitch length with imposed periodic boundary conditions. As the wire with multiple twist pitch gets longer, the wire portion of twist pitch length at its center is less influenced by the magnetic effects occuring at both the wire top and bottom ends.

From this study, we conclude that, given a minimum wire length, the magnetic

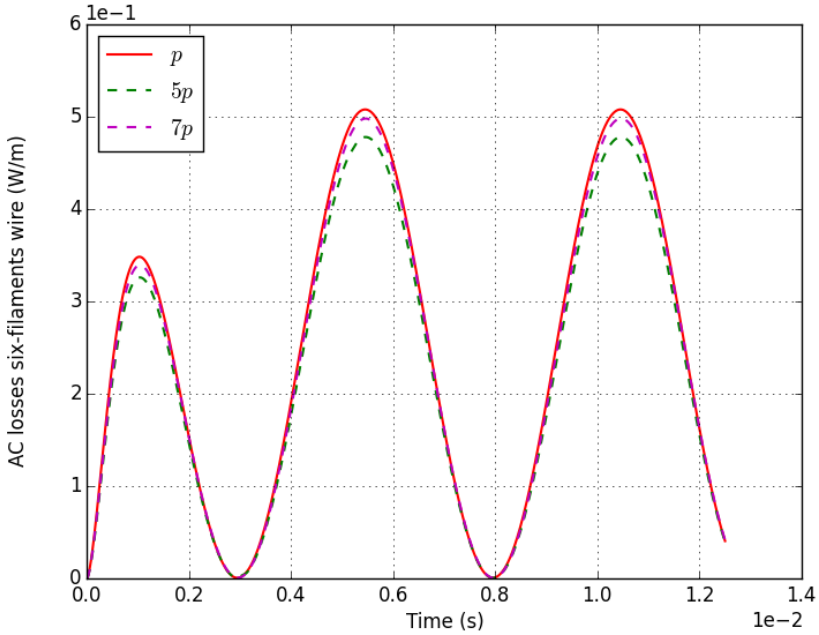

Figure 3.24 – Total ac losses comparison in the Frenet frame of a twisted six-filaments superconducting wire subjected and its truncated version to a transverse magnetic field

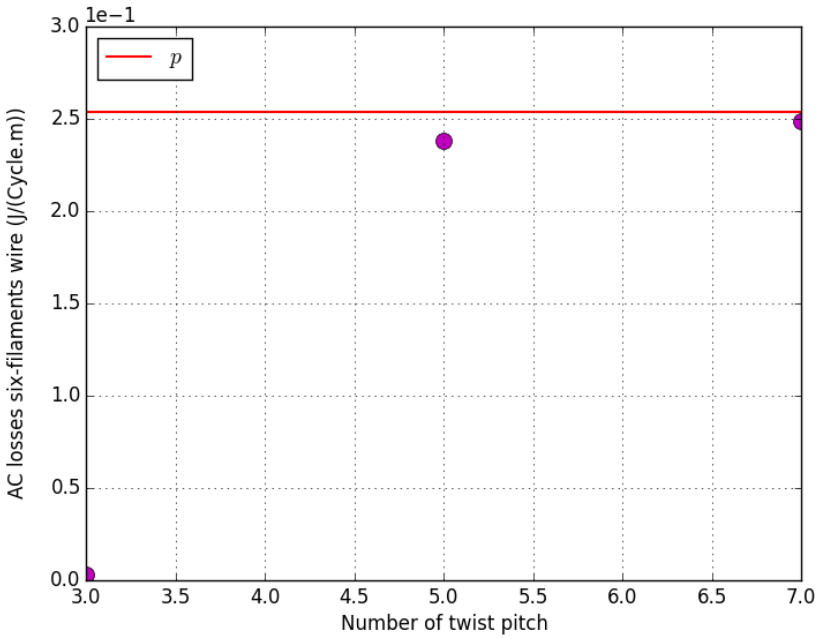

Figure 3.25 – Evolution of the AC losses per unit length with respect to the number of twist pitch of the wire

behaviour of a twisted multi-filamentary superconducting wire with multiple twist pitch can be approximated on a reduced model consisting of a twist pitch length wire with imposed periodic conditions at both its top and bottom ends. This reduced model approximates losses occuring at the center of the wire given that any magnetic influence of its ends are neglected.

3.6.2 Model-order reduction of a twisted multi-filamentary wire with multiple twist pitch

Based on the previous findings, we concluded that the magnetic behaviour of a truncated wire with a single twist pitch length and periodic boundary conditions imposed could give us an approximation of the magnetic behaviour of the whole wire with a minimal length. Thus, a model-order reduction of the whole wire was first introduced.

Because there are four current loops in a wire portion with a twist pitch length , with three of them equallly distributed along its length, we will further develop more reduced models to model the center of this portion. Since we are dealing in the Frenet frame with a straight multi-filamentary wire geometry , periodic boundary conditions can be easily implemented. Also, the electric current at the wire portion center remain the same, given the minimal wire length, further reduction of the twist pitch length should give us an approximation of the AC losses per unit length characterizing the whole wire.

Several simulations cases of different truncated parts, with $p/4$ and $p/16$ as length, of a twisted six-filaments superconducting wire, subjected to either a transverse or an axial magnetic field, were performed.

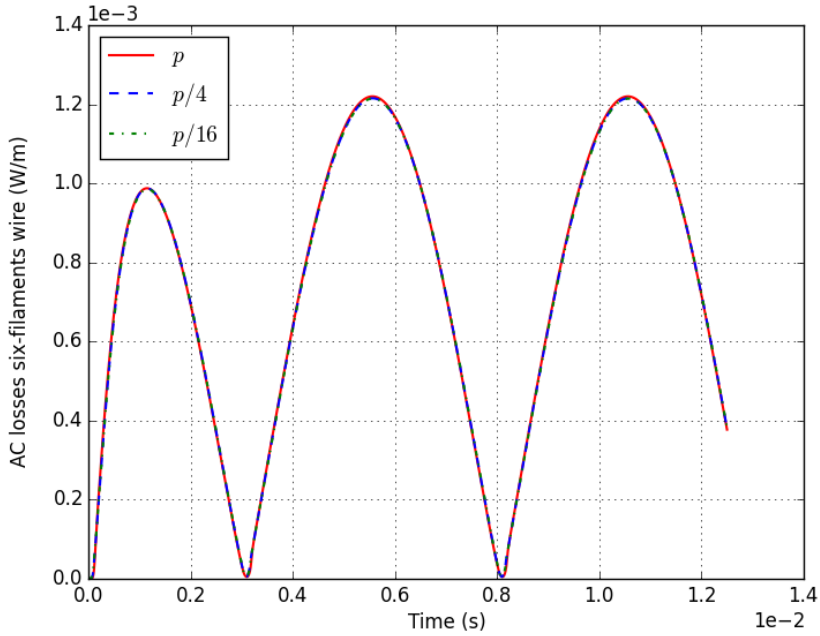

Figure 3.26 – Magnetization losses comparison of truncated twisted six-filaments superconducting wires subjected to a transverse magnetic field along the y-axis

Computed AC losses results, shown in figures 3.26 and 3.27, show the equivalent

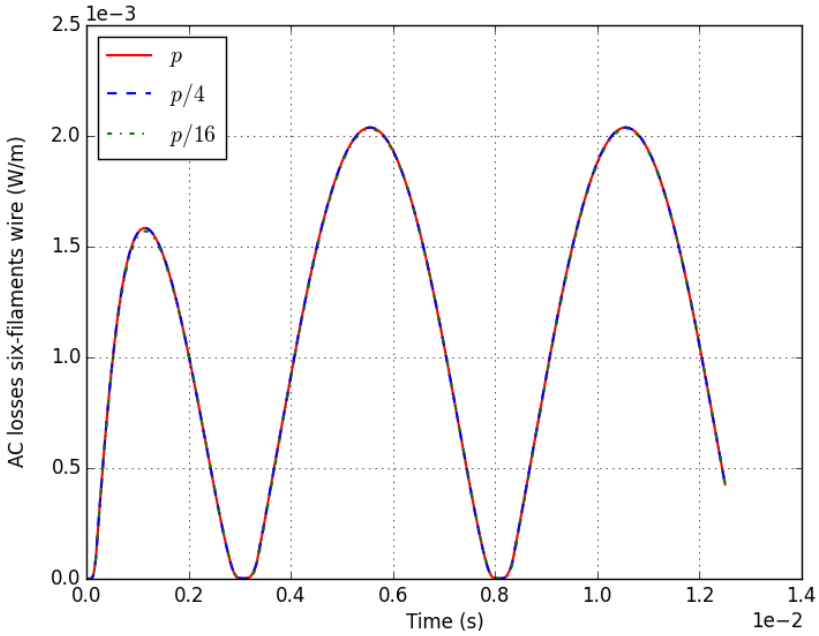

Figure 3.27 – Magnetization losses comparison of truncated six-filaments superconducting wire subjected to an axial magnetic field along the z-axis

magnetic behaviour of different truncated lengths of the single twist pitch wire, with periodic boundary conditions imposed. Thus we can further reduce the problem of modelling long twisted multi-filamentary wire in three dimensions, under a given minimal wire length, in order to effectively evaluate at the wire center its equivalent AC losses per unit length.

- **Special case : from 3D to pseudo-2D**

  Specific 3D problems can also be reduced to pseudo-2D problems. In the Frenet frame, the mapping matrix expressed in eq.3.12 can be simplified, with $\theta = \pi/2$ or $3\pi/2$, as follows :

$$P_{\mathcal{B}_f}^{\mathcal{B}_i} = \begin{bmatrix} \pm a & 0 & b \\ 0 & \pm 1 & 0 \\ \pm b & 0 & -a \end{bmatrix} \tag{3.15}$$

  Thus, the pseudo-2D problem is only valid for cases where the external transverse magnetic field is only along the y-axis. For other magnetic field configurations, the transformed field does not belong to the studied 2D section plane. The final reduced model is a 2D section of the wire whose position along its length is defined such that the imposed magnetic field, moving along the

helical trajectory, belongs to the xy plane.

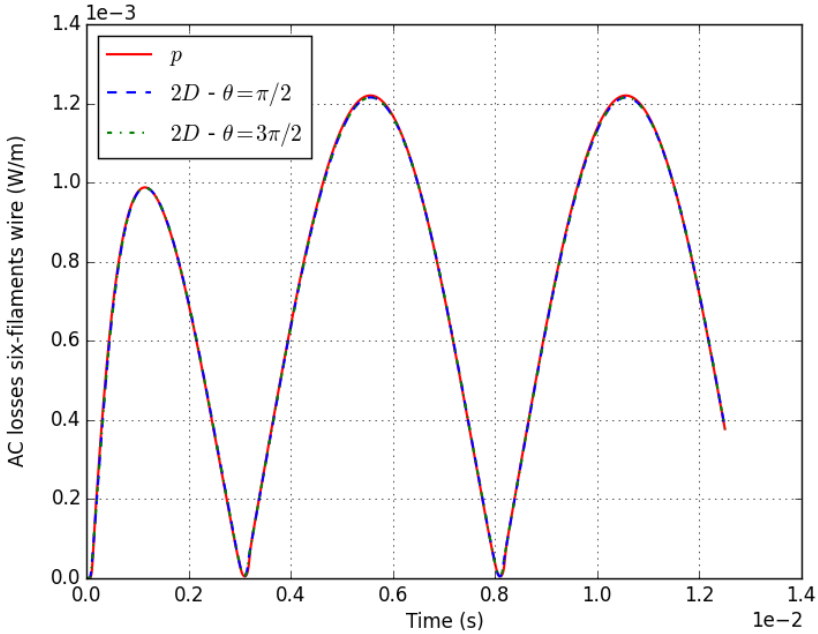

Figure 3.28 – Magnetization losses per unit length of a pseudo-2D representation in the Frenet frame of a truncated six-filaments superconducting wire subjected to a transverse magnetic field along the y-axis

The problem resolution of the section where the helix angular parameter $\theta = \pi/2$ ($z = p/4$) or $\theta = 3\pi/2$ ($z = 3p/4$) give us an equivalent pseudo-2D problem where AC losses per unit length remain the same.

3.6.3 Analysis of the impact of elliptical fields on magnetization losses

In the context of fully superconducting rotating machines, the stator conductor sees a combination of alternating $\mathbf{B}_{alt}$ and rotating $\mathbf{B}_{rot}$ fields. Such a combination is generally known as elliptical fields. It is mathematically expressed as :

$$\mathbf{B} = \mathbf{B}_{alt} + \mathbf{B}_{rot} \tag{3.16}$$

with

$$\mathbf{B}_{alt} = \begin{bmatrix} 0 \\ (1-k)B_0 cos(wt+\varphi) \\ 0 \end{bmatrix} \tag{3.17}$$

and

$$\mathbf{B}_{rot} = \begin{bmatrix} kB_0 sin(wt) \\ kB_0 cos(wt) \\ 0 \end{bmatrix} \tag{3.18}$$

This magnetic configuration is due to the high electrical loading of the stator and the air-core magnetic configuration.

Magnetization losses generated by a round mono-core wire, under elliptical fields, were evaluated and analyzed using a 2D finite element model [74]. Several numerical simulations were performed in order to improve the classical model by taking into account the contribution of the rotating component of the field on the magnetization losses. Beyond AC losses evaluation, this study allowed a physical understanding of the electrical behaviour of superconducting wire under such complex magnetic field configuration.

With the help of the previous study, the goal is to analyze, with the newly-developed model-order reduction, magnetization losses of twisted multifilamentary superconducting wires subjected to elliptical fields.

Based on several AC losses measurements taken with a calorimetric method , by researchers at CAPS (Center for Advanced Power Systems) in Tallahassee, from a sample of 100 multi-filamentary MgB_2 wires of 20 cm length each manufactured by Hypertech, comparisons will be made with numerical results resulting from the model-order reduction. Each wire have a twist pitch p of 25 mm and 54 twisted superconducting filaments of 37 μm of diameter embedded in a CuNi matrix of 0.7 mm. Characterization of filaments defined a critical current density $J_c = 2547$ A/mm^2 and $n = 4.42$.

In this study we are interested in computing measurements taken when the sample was subjected to elliptic fields with k varying from 0 to 1 (with a 0.2 step) and the amplitude B_0 either equal to 10 mT RMS (Root mean square) for a frequency of 110 Hz or 20 mT RMS for a frequency of 50 Hz. The applied field was imposed by setting a well-defined current inside coils inside which the sample is positioned such that the magnetic field is close to be uniform.

As seen in figures 3.29 and 3.30, a fit is possible between measurements and numerical values. Numerical values were obtained by the use of respectively two reduced models of the wire with $p/16$ and $p/2500$ as length. The model-order reduction model proposed above was applied and computations were made in less than a day on meshes of about 135000 and 63000 elements for the reduced models

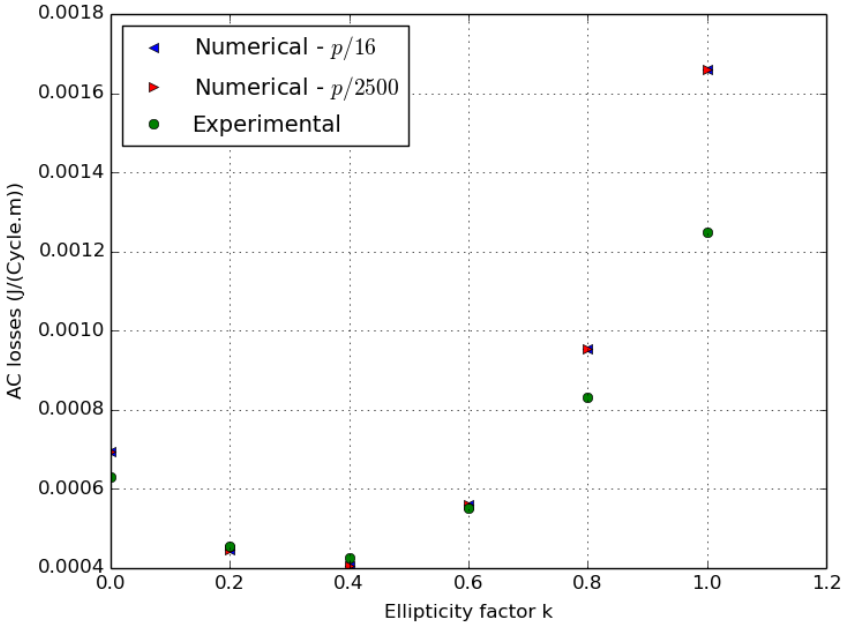

Figure 3.29 – Magnetization losses experimental vs numerical comparison of a twisted 54-filaments MgB_2 wire subjected to an elliptic field at 50 Hz

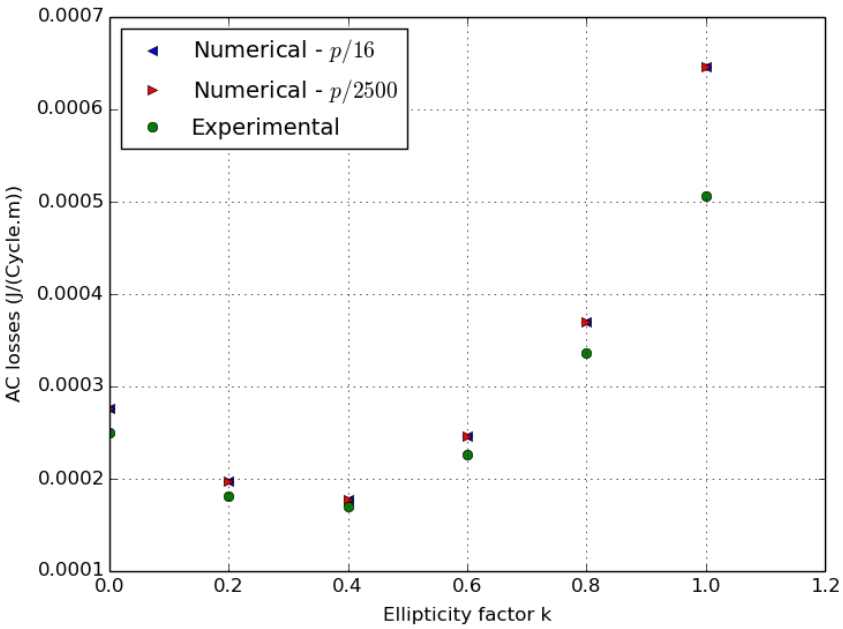

Figure 3.30 – Magnetization losses experimental vs numerical comparison of a twisted 54-filaments MgB_2 wire subjected to an elliptic field at 110 Hz

respectively. However, numerical values were obtained for at 80% of the value of the desired maximal applied field. This suggest a presence of defects in the coils surrounding the sample. In fact, some tests revealed the presence of some additional heat loads present in the coils.

With the lack of additionnal measurements data, more comparisons with the numerical model could not be performed.

Despite such shortcomings, the overall trend of the measured losses was kept intact and retrieved with the numerical model. Thus, the physical behaviour of the studied wire is well captured by the numerical model. As shown below, figures 3.31 and 3.32 illustrate that well with the computed instanteneous magnetization losses of reduced models of length $p/2500$ or $p/16$ of the wire.

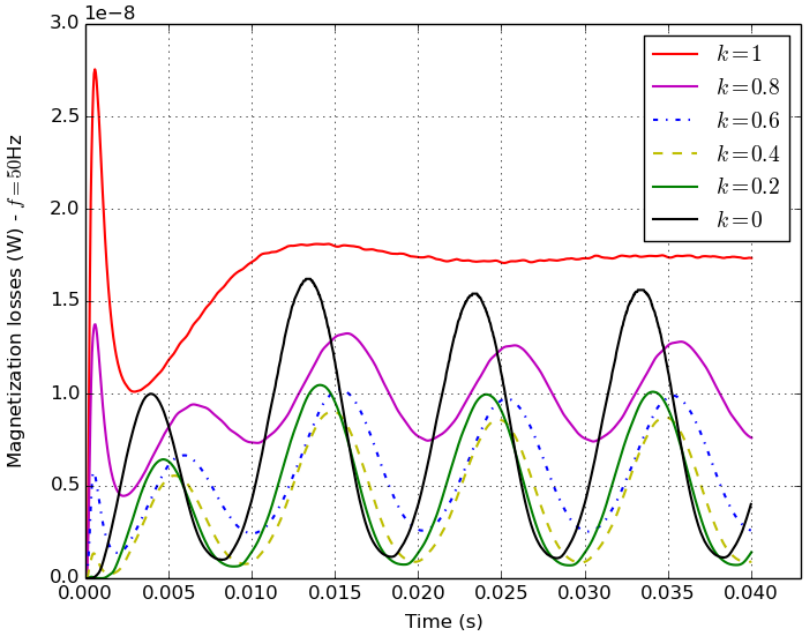

Figure 3.31 – Computed instanteneous magnetization losses of reduced models of the twisted 54-filaments MgB_2 wire subjected to an elliptic field at 50 Hz

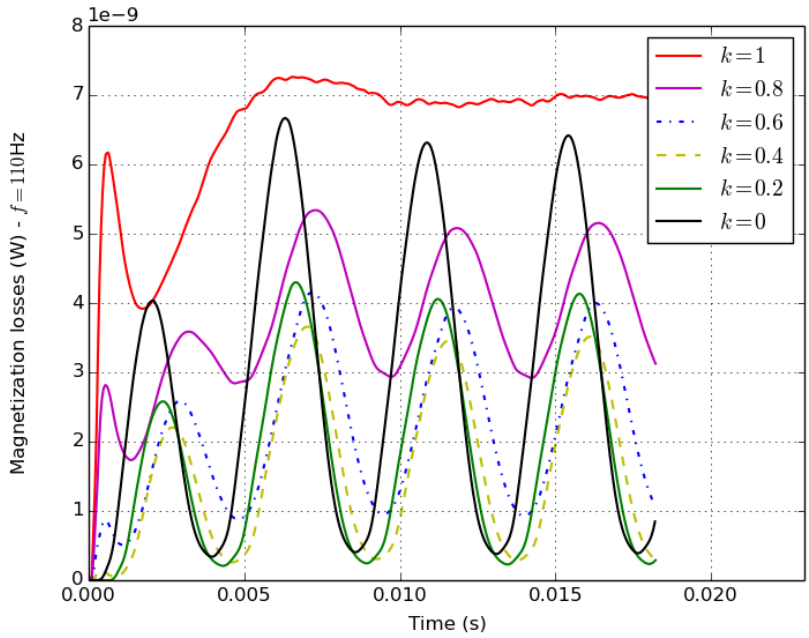

Figure 3.32 – Computed instanteneous magnetization losses of reduced models of the twisted 54-filaments MgB_2 wire subjected to an elliptic field at 110 Hz

As noticed in [74] for a straight mono-core wire, the maximum losses, which are constant, are obtained for $k = 1$. However the AC losses evolution with respect to k remains not the same. It is certainly due the twisted nature of the wire filaments geometry whose impact is translated to the magnetic field behaviour of the wire.

In conclusion, the model-order reduction proposed is able to capture in a simple way the physics involved in a complex twisted multi-filamentary superconducting wire subjected to a complex magnetic configuration. Results are computed quickly and we can have less degrees of freedoms. More comparisons with measurements must be done in order to completely validate such an approach.

3.7 Perspective : homogenization of multi-filamentary superconducting wire

As described above, the mapping allows us to reduce considerably the problem of modelling twisted multi-filamentary superconducting wires. With the mapping validation, we notice that the problem in the Frenet frame, characterized by a simple geometry of a wire with straight filaments subjected to a geometrically transformed magnetic field, gives us an approximate solution with higher precision than the one obtained in the initial frame.

Based on those premises, a brief investigation of an homogenization approach has been applied on twisted multi-filamentary superconducting wire subjected to an external magnetic field along the y-axis. Thus, a pseudo 2D model in the Frenet frame was used.

Wires with only one layer of filaments have been treated and the parameters of the studied wires and their homogenized versions were defined in table 3.4. Homogenization was studied on three twisted multi-filamentary superconducting wires which have respectively 2, 3 and 4 filaments (see figures 3.33a, 3.33b and 3.33c) .

The investigation was done empirically in order to show that an homogenization on those types of wires is possible. For a specific twisted wire with multiple superconducting filaments on its single layer, the study mainly consist in finding the equivalent magnetic behaviour of an equivalent wire with a single superconducting filament at the center.

In this brief study, the superconducting sub-domain volume, the wire length and the twist pitch remain unchanged. The conservation of the superconducting

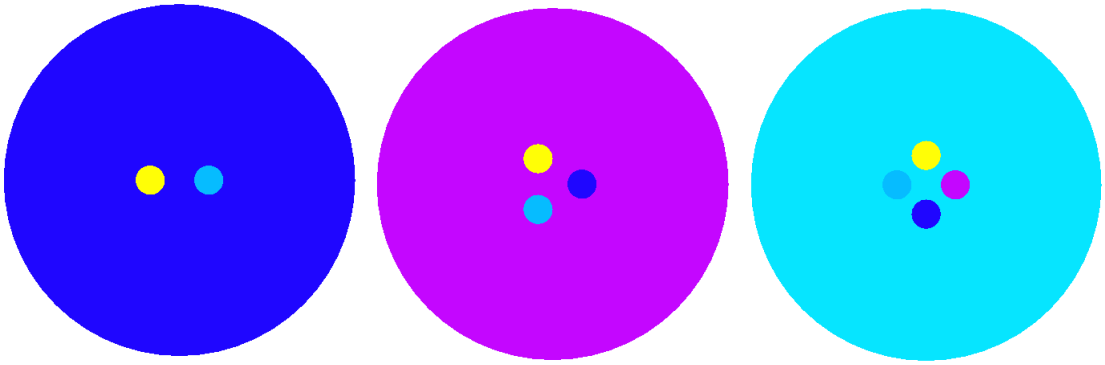

(a) 2 filaments (b) 3 filaments (c) 4 filaments

Figure 3.33 – Pseudo-2D representation in the Frenet frame of twisted multifilamentary superconducting wire subjected to a transverse magnetic field in the Frenet frame.

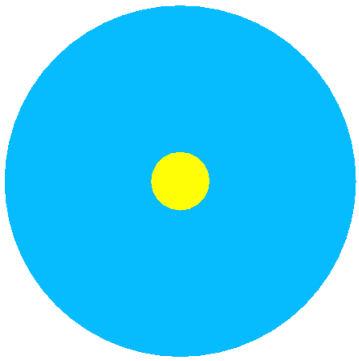

Figure 3.34 – Pseudo-2D representation in the Frenet frame of the homogenized twisted multifilamentary superconducting wire subjected to a transverse magnetic field in the Frenet frame.

sub-domain imply having as an homogenized version a single centered filament of radius $r_h = r/\sqrt{n_f}$.

The power law characterizing the electric behaviour of high temperature superconductors remained also unchanged. However, both the critical current density J_c and the power law index n were adjusted as follows :

$$J_{ch} = G(J_c, n_f, \alpha_v, \beta_{r_f}, \beta r_L) \tag{3.19}$$

and

$$n_h = g(n, n_f, \alpha_v, \beta_{r_f}, \beta r_L) \tag{3.20}$$

with J_{ch}, n_h the adjusted critical current density and the adjusted power law index. G and g are defined functions.

Those functions depends on the number of filaments n_f belonging to the layer,

Table 3.4 – Parameters of twisted multi-filamentary wire with multiple twist pitch for homogenization

Quantity	Value
Twist pitch p (mm)	4
number of filaments - normal n_f	2 or 3 or 4
number of filaments - homogenized n_{fh}	1
number of twist pitch n_p	≥ 7
Filament radius - normal r (μm)	50
Filament radius - homogenized r_h(μm)	$50\sqrt{2}$ or $50\sqrt{3}$ or 100
Matrix radius (mm)	0.6
Layer radius (mm)	0.1
Critical current density (A/mm^2)	5
Power law index n	10
Air conductivity (S/m)	10^3
Matrix conductivity (S/m)	$6{\cdot}10^9$
Magnetic field amplitude B_{max} (mT)	50
Frequency f (Hz)	100

the volume ratio α_v of the filaments with respect to the resistive matrice, the radial distribution β_{r_f} of the filaments on the layer and the radial distribution βr_L of the layers. The functions G and g must be evaluated correctly in order to get the equivalent magnetic behaviour.

In order to show that an homogenization is possible, we will evaluate empirically those functions for specific cases (wires with 2, 3 and 4 filaments respectively), with parameters set in, by choosing appropriate constant values J_{ch} and n_h. We will have :

- $J_{ch} = 1.01J_c$ and $n_h = 1.01n$ for 2 filaments
- $J_{ch} = 2.16J_c$ and $n_h = 2.16n$ for 3 filaments
- $J_{ch} = 1.7J_c$ and $n_h = 1.7n$ for 4 filaments

As shown in figures 3.35a, 3.35b and 3.35c, the computed magnetization losses of the homogenized wire show good agreement with the results from the actual wire.

In conclusion, the homogenization of a twisted multi-filamentary superconducting wire with a single layer of filaments is possible. A more in-depth research on the subject is necessary in order to define explicitely the functions G and g with respect to the different parameters mentioned above. They should also be formulated with consideration of wires with several layers of filaments.

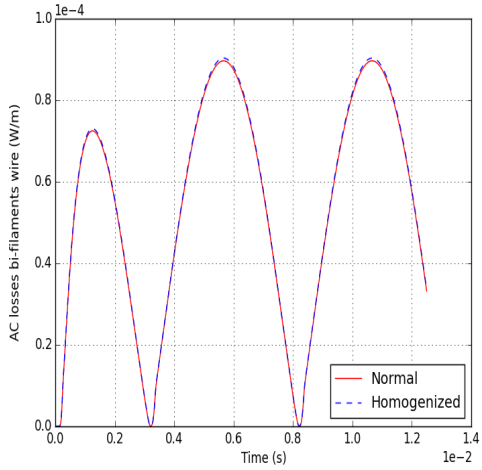

(a) Homogenized - 2 filaments

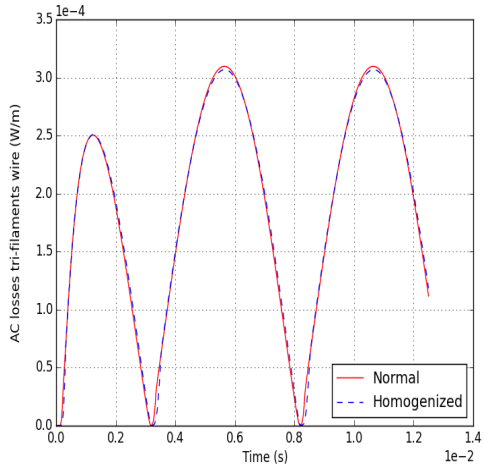

(b) Homogenized - 3 filaments

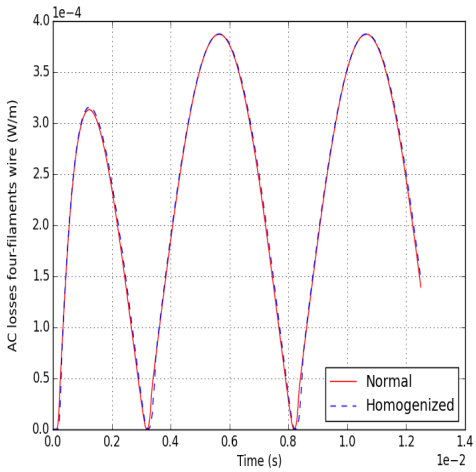

(c) Homogenized - 4 filaments

Figure 3.35 – Magnetization losses per unit length of a pseudo-2D representation in the Frenet frame of the pseudo-2D representation of twisted superconducting wires in the Frenet frame.

3.8 Conclusion

In this chapter, we proposed a geometric transformation which simplifies, through a well-defined mapping, the 3D modelling of twisted multi-filamentary superconducting wires. The mapping originates from observations made on the current distribution inside a twisted mono-filament superconducting wire subjected to a transverse magnetic field. In fact, several current loops, observed along the helical trajectory of the filament, suggested that the magnetic field was changing direction with respect to the filament trajectory.

Thus, the transformation allows the study of the straight wires in the Frenet frame subjected to a magnetic field moving along the helical trajectory that will result from twisting filaments.

The application of this mapping to both twisted bi-filaments and six-filaments superconducting wires have been successfully validated for a transverse and an axial external magnetic field. Computed AC losses of wires in both the initial frame and the Frenet frame show good agreement regardless of the parameters such as the magnetic field amplitude and the twist pitch.

Moreover, an advanced application of the proposed mapping allowed us to reduce the size of the 3D problem associated with the study of twisted multi-filamentary wire with multiple twist pitch. In fact, the computed AC losses per unit length in the wire becomes equivalent to the ones in a single twist pitch wire or its truncated length with imposed periodic boundary conditions imposed on both its ends. In the case of the transverse applied magnetic field, the 3D problem can be further reduced to a pseudo-2D problem where the transformed applied magnetic field is planar in the Frenet frame.

An application of the model-order reduction on a sample of 100 MgB_2 wires with 54 twisted filaments each gave, base on AC losses measurements, a good enough approximation of their magnetic behaviour under the influence of elliptical magnetic fields.

All those simplifications introduced and developed make possible the 3D modelling of twisted multi-filamentary superconducting wires with the finite element method.

The homogenization of multi-filamentary wire with multiple twist pitch were briefly explored. The goal was to show that such approach was worth investigating as an application of the mapping. A brief study was done in order to show this approach capabilities. A good agreement was obtained for computed AC losses in both the homogenized wire and non-homogenized wire. This approach can be studied more in-depth and it can help a further design optimization of superconducting wire.

General conclusion

The need of accurate evaluation of AC losses generated in large superconducting wire led us to investigate robust and efficient numerical methods with 3D modelling capabilities. By analyzing shortcomings of numerical approaches found in the literature, in regards with their 3D modelling capabilities of large superconducting systems such as wire, new approaches have been proposed.

First, the finite element method applied on the commonly used **H**-formulation was introduced with a focus on the linearization of the power law in order to handle its associated non-linearities for convergence purposes. Also, the discontinuous galerkin method applied on the commonly used **H**-formulation was proposed. Because of its parallel computation capabilities, this approach scales naturally with the computing architecture at disposal. Validations of this approach was done by comparing AC losses of simple models done using finite element method implemented in GetDP and Comsol Multiphysics. Unlike the finite element method, this approach is not limited by the available computing memory. Its parallel computation configuration allow the distribution of partitioned sub-domain of the studied mesh over numerous computers. This characteristic will be significant for 3D modelling of large superconducting systems such as wires. As future research endeavours, the resulting framework from this numerical approach can be optimized for fast computations with GPU computations instead of CPU.

Memory limitations associated with the finite element method impede its use for the 3D modelling of twisted multi-filamentary superconducting wires. Thus, an in-depth study of such wires led us to develop a mapping where there is an equivalent 3D model with straight filaments instead. The resistive matrix remain also straight if it is non-magnetic. Otherwise, the matrix geometry must be twisted. This mapping give us a less geometrically complex 3D model with less degrees of freedoms for AC losses computations. Numerous simulations were done for the purpose of a parametric study which validated the mapping use on twisted multi-filamentary wires.

Simplifications were further developed based on the developed mapping with the introduction of a model-order reduction approach. It allows to study shorter truncated 3-D version of a wire twist pitch in order to evaluate accurately the invariant AC losses per unit length. Such reduction is possible for wires with at least 7 twist pitches as we see that the greater the number of twist pitch is, the closer AC losses per unit length of the whole wire get to the ones of its reduced version. The problem can even be reduced to a 2D section with well-defined z positions for the specific case involving transverse magnetic field in the y-axis only.

In order to study the influence of elliptical magnetic fields on magnetization losses generated on 100 MgB_2 wires with 54 twisted filaments each, AC losses of the entire sample were computed from the 1/2500th of a single wire twist pitch. The 3D model-order reduction approach was applied on the mentioned truncated wire. We observed the expected AC losses behaviour as we increase the ellipticity of the applied magnetic field. This showed how the proposed reduced model approximates well the behaviour of wires under complex magnetic configurations.

As another application of this reduced 3D model, an homogenization approach was briefly investigated for wires with a single layer of filaments. The study, although performed empirically, shows good promises. It need to be thoroughly investigated in order to evaluate an expression of the required function allowing the homogenization for all types of twisted multi-filamentary wires. This can also lead to the homogenization of tapes where the superconducting materials is deposited.

All those newly numerical approaches show good promises regarding the 3D modelling of twisted multi-filamentary wires/tapes. The model-order reduction approach allows us to considerably reduce and simplify the resulting 3D problem while giving us a good approximation of the magnetic behaviour of the whole wire. The prospects of developing homogenization techniques will simplify even more the 3D modelling and likely ushered more research on the optimization design of those wires. AC losses measurements of those wires are also necessary in order to establish such modelling approaches.

Bibliography

[1] H.K. Onnes Comm. Phys. Lab. Univ. Leiden, pp. 119,120,122, 1911.

[2] W. Meissner, R. Ochsenfeld Naturewiss, vol. 21, p. 787, 1933.

[3] Coalition for the Commercial Applications of Superconductivity (CCAS). Superconductivity. [Online]: Available :http://www.ccas-web.org/superconductivity/.

[4] M. Tinkham *Introduction to Superconductivity* 2nd ed. Dover Publications, 1996.

[5] C. McNaught *Running smoothly: making motors more efficient* IEEE Review, Vol. 39, no. 2, pp. 89-91, 1993.

[6] C. P. Poole *Superconductivity* 2nd ed. Elsevier Ltd., 2007.

[7] A. A. Abrikosov *On the magnetic properties of superconductors of the second group* Sov. Phys. JETP-USSR, Vol. 5, no. 6, pp. 1174-1183, 1957.

[8] A.C. Rose-Innes, E.H. Rhoderick *Introduction to Superconductivity* revised 2nd ed. Pergamon Press, 1994, pp. 183-194.

[9] A.C. Rose-Innes, E.H. Rhoderick *Introduction to Superconductivity* Oxford: Pergamon Press, 1978.

[10] A. A. Golubov *Handbook of Applied Superconductivity* IOP Publishing, 1998, vol. 1, ch. A2: Type II superconductivity, pp. 37-52.

[11] J. Rhyner *Magnetic properties and AC-losses of superconductors with power law current-voltage characteristics* Physica C, vol. 212, pp. 292-300, 1993.

[12] P. W. Anderson *Theory of flux creep in hard superconductors* Phys. Rev. Lett., vol. 9, no. 7, pp. 309-311, 1963.

[13] E. Zeldov et al *Flux creep characteristics in high temperature superconductors.* Appl. Phy. Let., Vol. 56, number 7, p680-683, 1990

[14] C.P. Bean *Magnetization of high-field superconductors* Rev. Mod. Phys., p. 31, 1964.

[15] M. P. Oomen *AC loss in superconducting tapes and cables* Ph.D. dissertation, University of Twente, Enschede, The Netherlands, 2000.

[16] J. J. Rabbers *AC loss in superconducting tapes and coils* Ph.D. dissertation, University of Twente, Enschede, The Netherlands, 2001.

[17] M. M. Farhoudi *AC loss in Ag/Bi-2223 tapes in AC field* Master's thesis, University of Wollongong, Wollongong, Australia, 2005.

[18] W. J. Carr *AC loss and macroscopic theory of superconductors* 2nd ed. CRC Press, 2001.

[19] J. Jin and X. Chen *Development of HTS Transformers* in Proc. IEEE Int. Conf. Industrial Technology (ICIT 2008), Chengdu, China

[20] W. Paul et al *Fault current limiter based on high temperature superconductors - different concepts, test results, simulations, applications* Physica C 354, p. 27, 2001.

[21] M. Parizh, A.K. Kalafala and R. Wilcox *Superconducting magnetic energy storage for substation applications* IEEE Transactions on Applied Superconductivity, vol. 7, no. 2, p. 849, 1995.

[22] Y. Iwasa *HTS and NMR/MRI magnets: Unique features, opportunities, and challenges* Physica C: Superconductivity and its applications,vol. 445, p. 1088-1094, 2006.

[23] J.F. Maguire et al *Development and demonstration of a HTS power cable to operate in the long island power authority transmission grid* IEEE Transactions on Applied Superconductivity, vol. 17, no. 2, pp. 2034-2037, 2007.

[24] S.H. Sohn et al *The results of installation and preliminary test of 22.9 kV, 50 MVA, 100 m class HTS power cable system at KEPCO* IEEE Transactions on Applied Superconductivity, vol. 17, no. 2, pp. 2043-2046, 2007.

[25] C.H. Joshi, C.B. Prum, R.F. Schiferl, D.I. Driscoll *Demonstration of two synchronous motors using high temperature superconducting field coils* IEEE Transactions on Applied Superconductivity, vol. 5, no. 2, pp. 968-971, June 1995.

[26] R.F. Schiferl, B.X. Zhang, D.I. Driscoll, B.A. Shoykhet, R.C. Dykhuizen *Development status of a 125 horsepower superconducting motor* Advances in Cryogenic Engineering, Pleunum Press, vol. 42, pp.977-984, 1997.

[27] V. Dombrovski , D. Driscoll, B.A. Shoykhet, S.D. Umans , J.K. Zevchek *Design and testing of a 1000-hp high-temperature superconducting motor* IEEE Transactions on Energy Conversion, vol. 20, no. 3, pp. 638-643, September 2005.

[28] B.B. Gamble, S. Kalsi, G. Snitchler, D. Madura, R.Howard *The status of HTS motors* Proceedings of the IEEE Power Engineering Society Transmission and Distribution Conference, vol. 1, pp. 270-274, 2002.

[29] S. Greg, G. Bruce, S.K. Swarn *The performance of a 5 MW high temperature superconductor ship propulsion motor* IEEE Transactions on Applied Superconductivity, vol. 15, no. 2, pp. 2206-2209, June 2005.

[30] P.J Masson and al *HTS motors in aircraft propulsion: design considerations* IEEE Trans. Appl. Supercond., Vol. 15, number 2, p2218-2221, 2005.

[31] M. Frank, J. Frauenhofer, P. Van Hasselt, W. Nick, H.W. Neumueller, G. Nerowski *Long-term operational experience with first siemens 400 kW hts machine in diverse configurations* IEEE Transactions on Applied Superconductivity, vol. 13, no. 2, pp. 2120-2123, June 2003.

[32] H.W. Neumuller, W. Nick, B. Wacker, M. Frank, G. Nerowski, J. Frauenhofer, W. Rzadki, R. Hartig *Advances in and prospects for development of high-temperature superconductor rotating machines at Siemens* Superconductor Science and Technology, vol. 19, no. 3, pp. S114-S117, March 2006.

[33] Y.K. Kwon, M.H. Sohn, S.K. Baik, E.Y. Lee, J.M. Kim, T.S. Moon, H.J. Park, Y.C. Kim, K.S. Ryu *Development of a 100 hp synchronous motor with HTS field coils* IEEE Transactions on Applied Superconductivity, vol. 15, no. 2, pp. 2194-2197, June 2005.

[34] Y.S. Jo, Y.K. Kwon, M.H. Sohn, Y.K. Kim, J.P. Hong *High temperature superconducting synchronous motor* IEEE Transactions on Applied Superconductivity, vol. 12, no. 1, pp. 833-836, March 2002.

[35] H. Matsuzaki, Y. Kimura, I. Ohtani, M. Izumi, T. Ida, Y. Akita, H. Sugimoto, M. Miki, M. Kitano *An axial gap-type HTS bulk synchronous motor excited by pulsed-field magnetization with vortex-type armaturecopper windings* IEEE Transactions on Applied Superconductivity, vol. 15, no. 2, pp. 2222-2225, June 2005.

[36] M. Ainslie *Transport AC loss in high temperature superconducting coils* Ph.D. dissertation, University of Cambridge, Cambridge, United Kingdom, 2012.

[37] P.J Masson and al *Modelling of high temperature superconductors for AC power applications* Ph.D. dissertation, École Polytechnique Fédérale de Lausanne, Lausanne, Switzerland, 2002.

[38] S.S. Kalsi, B.B. Gamble, G. Snitchler, S.O. Ige *The status of HTS ship propulsion motor developments* IEEE Power Engineering Society General Meeting, vol. 18-22, June 2006 .

[39] L.H. Zheng, J.X. Jin, Y.G. Guo, J.G. Zhu *Technical and Theoretical Analysis of HTS Machines and Their Development* Nature Sciences, vol. 1, No. 1, pp. 33-41, December 2006.

[40] J.T. Eriksson, R. Mikkonen, J. Paasi, R. Perala, L.Soderlund *A HTS synchronous motor at different operating temperatures* IEEE Transactions on Applied Superconductivity, vol. 7, no. 2, pp. 523-526, June 1997.

[41] E. Vinot, G. Meunier, P. Tixador *Different formulations to model superconductors* IEEE Transactions on Magnetics, Vol. 36, No. 4, pp. 1226-1229, 2000.

[42] F. Grilli *Numerical Modeling of HTS Applications* IEEE Transactions on Applied Superconductivity , Vol. 26, No. 3, pp. 1-8, April 2016.

[43] L. Prigozhin *The Bean model in superconductivity: Variational formulation and numerical solution* Journal of Computational Physics, Vol. 129, No. 1, pp. 190-200, 1996.

[44] M. Maslouh and F. Bouillault *Modélisation des phénomènes électromagnétiques dans les matériaux supraconducteurs.* The European Physical Journal-Applied Physics, Vol. 1, No. 3, pp. 190-200, 1996.

[45] A. Sanchez, C. Navau *Magnetic properties of finite superconducting cylinders. I. Uniform applied field* Physical Review B, Vol. 64, No. 21, p. 214506, 2001.

[46] E. Pardo, F. Gömöry, J. Šouc, and J. M. Ceballos *Current distribution and ac loss for a superconducting rectangular strip with in-phase alternating current and applied field* Superconductor Science and Technology, Vol. 20, No. 4, p. 351, 2007.

[47] F. Sirois, F. Roy, B. Dutoit *Assessment of the computational performances of the semi-analytical method (SAM) for computing 2-D current distributions in superconductors* IEEE Transactions on Applied Superconductivity, Vol. 19, No. 3, pp. 3600-3604, 2009.

[48] E. H. Brandt *Superconductors of finite thickness in a perpendicular magnetic field: Strips and slabs* Physical review B, Vol. 54, No. 6, p. 4246, 1996.

[49] F. Sirois, F. Grilli *Potential and limits of numerical modelling for supporting the development of HTS devices* Superconductor Science and Technology, Vol. 28, No. 4, p.043002, 2015.

[50] A.M. Campbell *A direct method for obtaining the critical state in two and three dimensions* Superconductor Science and Technology, Vol. 22, No. 3, p.034005, 2009.

[51] M. Zhang, T.A. Coombs *3D modeling of high-Tc superconductors by finite element software* Superconductor Science and Technology, Vol. 25, No. 1, p.015009, 2011.

[52] F. Grilli, R. Brambilla, F. Sirois, A. Stenvall, S. Memiaghe *Development of a three-dimensional finite-element model for high-temperature superconductors based on the H-formulation* Cryogenics, Vol. 53, pp. 142-147, 2013.

[53] F. Grilli, S. Stavrev, Y. Le Floch, M. Costa-Bouzo, E. Vinot, I. Klutsch, G. Meunier, P. Tixador, B. Dutoit *Finite-element method modeling of superconductors: From 2-D to 3-D* IEEE Transactions on Applied Superconductivity, Vol. 15, No. 1, pp. 17-25, 2005.

[54] G. Rubinacci, A. Tamburrino, A., F. Villone *Three dimensional finite elements modeling of superconductors* IEEE Transactions on Magnetics, Vol. 36, No. 4, pp. 1276-1279, 2000.

[55] A. Bossavit *Numerical modelling of superconductors in three dimensions: a model and a finite element method* IEEE Transactions on Magnetics, Vol. 30, No. 5, pp. 3363-3366, 1994.

[56] A. Lotfi, F. Bouillault, S.M. Mimoune *Numerical study of the influence of flux creep and of thermal effect on dynamic behaviour of magnetic levitation systems with a high-Tc superconductor using control volume method* The European Physical Journal-Applied Physics, Vol. 45, No. 2, 2009.

[57] A. Lotfi, F. Bouillault, L. Bernard, J. Lévêque, S.M. Mimoune *3D modeling of forces between magnet and HTS in a levitation system using new approach of the control volume method based on an unstructured grid* Physica C: Superconductivity , Vol. 475, pp. 32-37, 2012.

[58] A. Lotfi, F. Bouillault, A. Kameni, S.M. Mimoune, M. Feliachi *3-D Numerical Evaluation of Trapped Magnetic Field and Temperature of a Rectangular GdBaCuO Bulk Magnetized by MMPSC Method* IEEE Transactions on Magnetics, Vol. 51, No. 3, pp. 1-4, 2015.

[59] A. Kameni, D. Netter, F. Sirois, B. Douine, J. Lévêque *New hybrid FE-FV method for computing current distribution in 2-D superconductors: Application to an HTS cylinder in transverse magnetic field* IEEE Transactions on Magnetics, Vol. 19, No. 3, pp. 2423-2427, 2009.

[60] A. Kameni, S. Mezani, F. Sirois, D. Netter, J. Lévêque, B. Douine *A 2-D robust FE-FV mixed method to handle strong nonlinearities in superconductors* IEEE Transactions on Magnetics, Vol. 46, No. 8, pp. 3445-3448, 2010.

[61] D.N. Arnold, F. Brezzi, B. Cockburn, and L.D. Marini *Unified analysis of discontinuous galerkin methods for elliptic problems* SIAM journal on numerical analysis, Vol. 39, No. 5, pp. 1749-1779, 2002.

[62] A. Kameni, J. Lambrechts, J.F. Remacle, S. Mezani, F. Bouillault, C. Geuzaine *Discontinuous Galerkin method for computing induced fields in superconducting materials* IEEE Transactions on Magnetics, Vol. 48, No. 2, pp. 591-594, 2012.

[63] A. Kameni, M. Boubekeur, L. Alloui, F. Bouillault, J. Lambrechts *A 3-D semi-implicit method for computing the current density in bulk superconductors* IEEE Transactions on Magnetics, Vol. 50, No. 2, pp. 377-380, 2014.

[64] L. Makong, A. Kameni, P. Masson, J. Lambrechts, F. Bouillault. *3-D modeling of heterogeneous and anisotropic superconducting media* IEEE Transactions on Magnetics, Vol. 52, No. 3, 2016.

[65] S.D Chen and al *Design of a HTS Magnet for Application to Resonant X-Ray Scattering* IEEE Trans. Appl. Supercond., Vol. 21, number 3, p1661-1664, 2013.

[66] C.J Christopherson and G.N. Riley, Jr. *Development of twisted high-temperature superconductor composite conductors* Appl. Phys. Lett., Vol. 66, number 17, p2277-2279 , 1995.

[67] P. Dular, C. Geuzaine, F. Henrotte, W. Legros *A general environment for the treatment of discrete problems and its application to the finite element method* IEEE Transactions on Magnetics, Vol. 34, No. 5, pp. 3395-3398, 1998.

[68] ONELAB, 'Superconducting wire', 2017. [Online]: Available : http://onelab.info/wiki/Superconducting_wire

[69] M. Boubekeur *Evaluation de l'efficacitÃ© de blindage de structures avec plaques minces : modÃ©lisation par une mÃ©thode de Galerkin discontinue* Ph.D. dissertation, University Paris-Sud, Cambridge, Orsay, 2014.

[70] M.J. Grote, A. Schneebeli, D. Schötzau *Interior penalty discontinuous Galerkin method for Maxwell's equations: Energy norm error estimates* Journal of Computational and Applied Mathematics, Vol. 204, No. 2, pp. 375-386, 2007.

[71] L. Makong, A. Kameni, F. Bouillault, C. Geuzaine, P. Masson *Nodal discontinuous Galerkin method for high-temperature superconductors modeling based on the H-formulation* Int J Numer Model. pp. 2298-2306, 2017.

[72] L. Makong, A. Kameni, L. Queval, P. Masson, F. Bouillault *H-formulation using the Discontinuous Galerkin method for the 3D Modeling of Superconductors* IEEE Transactions on Magnetics, 2017 (Accepted).

[73] L. Makong, A. Kameni, P. Masson, F. Bouillault *3D Equivalent Model to Compute the Electro-Magnetic Behaviour of Twisted Multi-filamentary Superconductors Wires* IEEE Transactions on Magnetics, 2017 (In review).

[74] C. Lorin and P. Masson *Numerical Analysis of the Impact of Elliptical Fields on Magnetization Losses* IEEE Trans. Appl. Supercond., Vol. 23, number 3, pp. 8201405-8201405, 2013.

ÉCOLE DOCTORALE
Physique et ingénierie : électrons, photons, sciences du vivant (EOBE)

Titre : Modélisation tridimensionnelle de supraconducteurs multifilamentaires torsadés

Mots clefs : supraconducteurs à hautes températures, câbles multifilamentaires torsadés, modélisation tridimensionnelle

Résumé : Les supraconducteurs à hautes temperatures sont considérablement utilisés dans des applications telles que des machines électriques. La conception de telles machines requiert une évaluation précise des pertes AC générées par leurs bobinages de câbles supraconducteurs multifilamentaires torsadés. Ainsi, des outils numériques robustes et précis sont indispensables afin de modéliser rapidement en 3D le comportement de tels câbles. Dans ce manuscrit, deux approches numériques dont une approche de type galerkin discontinue furent développées afin de simplifier considérablement la modélisation 3D de ce type de câbles. Elles furent appliquées à la formulation en **H** couplée aux effets thermiques. La modélisation de cas simples a permis de valider ces approches en les comparant à celle des elements finis implementée sur Comsol. Puis, une transformation géométrique fut proposée afin de modéliser de façon équivalente en 3D, quelque soit la configuration en champ magnétique, des câbles à filaments supraconducteurs droits à la place de filaments torsadés. De cette transformation, un modèle d'ordre réduit fut développé et validé afin de simplifier considérablement la modélisation 3D de ce type de câbles. À partir de ce modèle réduit, l'influence du champ elliptique sur les pertes par aimantation d'un échantillon de 100 câbles de 54 filaments de MgB_2 torsades fut modélisé en moins d'une journée. Par ailleurs, des premières études empiriques montrant la faisabilité d'une homogénéisation furent brièvement présentées et validées pour des câbles ayant une seule couche de filament.

Title : 3D modelling of twisted multi-filamentary superconductors

Keywords : High-temperature superconductors, twisted multi-filamentary wires, 3D modelling

Abstract : High temperature superconductors are increasingly being used for several applications such as electrical machines. Thus the design of such devices ultimately requires an accurate evaluation of AC losses generated by superconducting coils sometimes made of twisted multifilamentary wires. The development of robust numerical tools geared towards the 3D modeling of such wires is therefore needed. In this manuscript, the main objective is to develop numerical approaches allowing considerable simplifications of the modelling of twisted multi-filamentary superconducting wires in 3D.
First, two numerical approaches such as the discontinuous galerkin method applied on the thermally coupled **H**-formulation were developed. They were compared and validated on simple cases using the finite element method implemented in Comsol. Then, a well-defined mapping was proposed to simply model in 3D, for any magnetic field configuration, straight multifilamentary wires instead of twisted ones. An application of this mapping allowed the development of a model-order reduction approach which simplify considerably the modelling of twisted wires in 3D. Thus, the elliptical magnetic fields impact on magnetization losses was accurately modeled in less than a day with the reduced approach applied on 100 MgB_2 wires with 54 twisted filaments. As a research perspective on the reduced model advanced applications, an homogenization, empirically defined, was briefly presented for wires with single layer only.

Université Paris-Saclay
Espace Technologique / Immeuble Discovery
Route de l'Orme aux Merisiers RD 128 / 91190 Saint-Aubin, France